

**Development of infrared spectroscopy techniques  
for environmental monitoring**

**Jonas Sandsten**

Lund Reports on Atomic Physics  
LRAP-257

Doctoral Thesis  
Department of Physics  
Lund Institute of Technology  
August 2000

ISBN 91-7874-055-X

*To Maria and Erik*

## Contents

<b>Abstract</b>	<b>6</b>
<b>List of papers</b>	<b>7</b>
<b>1. Introduction</b>	<b>9</b>
<b>2. Infrared radiation sources</b>	<b>12</b>
2.1 <i>Natural background radiation</i>	12
2.2 <i>Artificial infrared radiation</i>	14
2.3 <i>Near-infrared diode lasers</i>	15
2.4 <i>Difference-frequency generation with near-infrared diode lasers</i>	16
2.5 <i>Passive versus active remote-sensing methods</i>	17
<b>3. Infrared spectroscopy</b>	<b>18</b>
3.1 <i>The gas-correlation principle</i>	25
3.2 <i>The two-dimensional extension to the gas-correlation principle</i>	27
3.3 <i>Gas concentration calibration</i>	28
3.4 <i>Aerosol particle scattering</i>	33
<b>4. Infrared image detectors</b>	<b>39</b>
4.1 <i>Thermal detectors</i>	39
4.2 <i>Photon detectors</i>	40
<b>5. Optical design considerations</b>	<b>42</b>
5.1 <i>Gas-correlation telescopes</i>	43
5.2 <i>Gas-filter cell design</i>	47
5.3 <i>Aerosol particle sensor optics criteria</i>	48
5.3 <i>Difference-frequency generation criteria</i>	51
<b>6. Image processing</b>	<b>53</b>
6.1 <i>Gas visualization</i>	53
6.2 <i>Noise in gas-correlated images</i>	56
6.3 <i>Gas flow evaluation by cross correlation in time</i>	57
<b>7. Applications</b>	<b>58</b>
7.1 <i>Gas visualization</i>	58
7.2 <i>Aerosol particle sensor</i>	63
7.3 <i>Diode laser spectrometer</i>	63
<b>8. Summary of papers</b>	<b>64</b>
<b>Acknowledgements</b>	<b>65</b>
<b>References</b>	<b>66</b>

## **Abstract**

Infrared spectroscopy techniques have long been utilized in identifying and quantifying species of interest to us. Many of the elementary molecules in the atmosphere interact with infrared radiation through their ability to absorb and emit energy in vibrational and rotational transitions. A large variety of methods for monitoring of molecules and aerosol particles by collecting samples or by using remote sensing methods are available. The objective of the work presented in this thesis was to develop infrared spectroscopic techniques to further enhance the amount of useful information obtained from gathering spectral data.

A new method for visualization and quantification of gas flows based on gas-correlation techniques was developed. Real-time imaging of gas leaks and incomplete or erratic flare combustion of ethene was demonstrated. The method relies on the thermal background as a radiation source and the gas can be visualized in absorption or in emission depending on the temperature difference.

Diode laser spectroscopy was utilized to monitor three molecular species at the same time and over the same path. Two near-infrared diode lasers beams were combined in a periodically poled lithium niobate crystal and by difference-frequency generation a third beam was created, enabling simultaneous monitoring of oxygen, water vapor and methane.

Models of aerosol particle cross sections were used to simulate the diffraction pattern of light scattered by fibers, spherical particles and real particles, such as pollen, through a new aerosol particle sensing prototype. The instrument, using a coupled cavity diode laser, has been designed with a ray-tracing program and the final prototype was employed for single aerosol particle sizing and identification.

## List of papers

This thesis is based on the following papers which will henceforth be referred to by their Roman numerals, I-V.

- I J. Sandsten, H. Edner, and S. Svanberg, "Gas imaging by gas-correlation spectrometry," *Optics Letters* **23**, 1945 (1996).
- II J. Sandsten, P. Weibring, H. Edner, and S. Svanberg, "Real-time gas-correlation imaging employing thermal background radiation," *Optics Express* **6**, 92 (2000); <http://www.opticsexpress.org/opticsexpress/tocv6n4.htm>
- III J. Sandsten, H. Edner, and S. Svanberg, "Gas visualization of industrial hydrocarbon emissions," Manuscript for *Applied Physics B*, (2000).
- IV U. Gustafsson, J. Sandsten, and S. Svanberg, "Simultaneous detection of methane, oxygen and water vapor utilizing near-infrared diode lasers in conjunction with difference frequency generation," *Applied Physics B*, in press.
- V J. Sandsten, U. Gustafsson, and G. Somesfalean, "Single aerosol particle sizing and identification using a coupled-cavity diode laser," *Optics Communications* **168**, 17 (1999).

## 1. Introduction

Humans make decisions based on information gathered by the senses. Information with high quality makes it easier to take the correct measures in complex decision situations. The development of instruments enhancing the sense of sight makes it possible for us to monitor species invisible to us. Greenhouse gases and aerosol particles are examples of species that we are able to sense with optical instruments through absorption and scattering of light. Several instruments have been employed during the last century to monitor gases and aerosol particles emanating from a variety of both natural sources, like volcanoes and sea spray, and manmade sources like those related to combustion of fossil fuel. Some of the most useful instruments are based on the remote sensing techniques, [1]. The principles that the instruments rely on are called *passive* if natural radiation sources are used, such as thermal background radiation or the sun, and they are called *active* if they rely on an artificial source of radiation, like a lamp or a laser. The most widely spread passive optical technique is visible light photography, as illustrated in the upper left corner of Fig. 1. The sun is used as a light source and objects can be imaged by the spectrally reflected light. The upper middle box in Fig. 1, illustrates a situation where the thermal background is radiating behind a gas cloud. This radiation is also called infrared light and it can be used to monitor many molecules in the fundamental infrared region (2.7–20 $\mu\text{m}$ ) due to their strong absorption by vibrational- and rotational transitions. The energy absorbed by the molecules can also be emitted and observed against a cold background, as depicted in the upper right box in Fig. 1. In the lower left box an artificial source of radiation is utilized, e.g. an incandescent lamp, a laser or a glow bar. The spectral brightness of such a source can easily be more than a million times higher than the brightness from a passive source. Instruments based on active techniques are therefore suitable as trace gas detectors and the path-integrated absorption can be measured to ppt levels (ppt = 1 part in 10<sup>12</sup>). Differential optical absorption spectroscopy, DOAS [2], Fourier transform infrared, FTIR [3-5], and diode laser spectroscopy [6] are all active transmission techniques, and by increasing the path-length between the source and the instrument, minute amounts of trace gases in the atmosphere can be measured. However, the number of particles, water droplets and absorbing molecules other than the measured molecules in the path between the instrument and the source will decrease the visibility. At sea, the mariners use the visibility to describe horizontal atmospheric conditions. A normal weather condition is in this context, defined as having a transmission of 74% or a visibility of 10 nautical miles (18.52 km). A mist has a visibility of 1 km or a transmission of 60% and a perfect transmission of 100% never prevails in the atmosphere. This limits the practical distance of active measurements with ppt detection limits to a few kilometers in urban areas. In the lower middle box in Fig. 1, a pulsed laser beam is directed out in the atmosphere and the backscattered light from aerosol particles is collected by a telescope. If the laser beam frequency is alternately tuned on and off a molecular absorption line, the influence of other slowly frequency varying absorbing

molecules and particles will not affect a differential on/off signal. Range resolved measurements can be performed by gating the detector and thus collecting light from scattering particles along the beam path. Light detection and ranging, LIDAR, and the described extension, DIAL, differential absorption lidar, are techniques utilizing aerosol back-scattering [7-9].

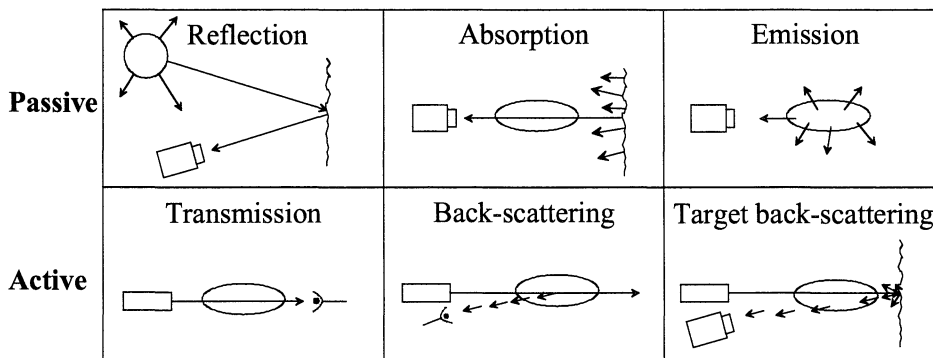


Fig. 1. Passive and active remote sensing techniques.

If a diffusely scattering target is used as a background, as shown in the lower right box, a stronger backscattered signal is obtained but the range resolution is lost and the path-integrated measurement is performed over the whole laser beam. Topographic differential absorption LIDAR has recently been extended to an imaging mode and this technique is called differential backscatter-absorption gas imaging, BAGI [10-15]. This technique is requiring a large laser system as an illuminating source. Other gas imaging systems utilize a heated background and view the gas in absorption with an infrared camera equipped with a bandpass filter [16,17]. A Fabry-Perot etalon, an acousto-optic filter or an interferometric correlator can be used instead of the bandpass filter to enhance the contrast in gas visualization [18-21]. DOAS, FTIR and LIDAR are all line-of-sight instruments, meaning that if we would like to create a cross-sectional image the instrumental field-of-view must be swept over the scene. Measurements performed from satellites are based on passive methods and a vertical column of air through the whole atmosphere is the most common line-of-sight mode. The Terra satellite with the Measurements of Pollution in The Troposphere (MOPITT) instrument onboard, released the first scientific data and images in April 2000. The instrument makes it possible to create global maps of methane and carbon monoxide utilizing a gas-correlation technique [22-27].

The new gas-correlation imaging technique, which is presented in this thesis, is a compact and straightforward passive imaging method where the natural thermal background radiation is employed, either in an absorption mode or in an emission mode [Papers I-III]. Presently, the applications where the gas-correlation imaging

can be most beneficial are when the molecular concentrations are localized as in the case of leak searching and flare combustion monitoring. The gas-correlation imaging system is based on an infrared sensitive camera, a gas-correlation telescope with a gas-filter cell and a filter wheel with different spectral filters tuned to specific gas absorption bands. The camera system is depicted in Fig. 2.

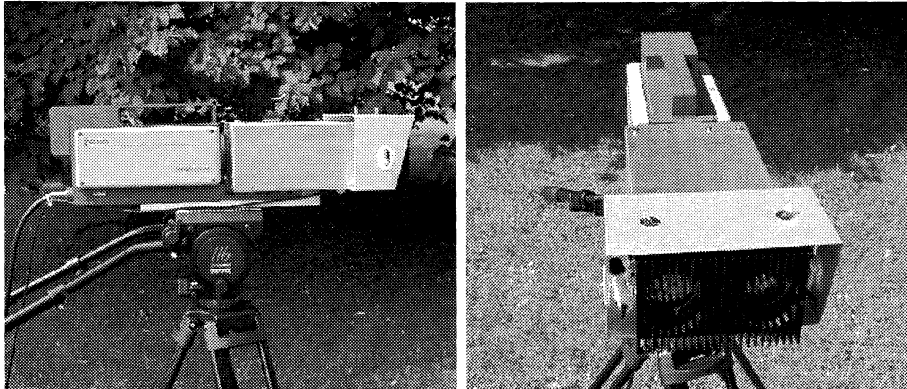


Fig. 2. The gas-correlation camera system.

The diode laser based instruments developed during this work are active transmission and scattering instruments. One is a tunable spectrometer capable of detecting three species (methane, water vapor and oxygen) simultaneously [Paper IV] and the other one is an aerosol particle sensor based on extinction and diffraction of near-infrared diode laser light inside a coupled cavity [Paper V].

The following chapters will cover complementary issues of relevance to the technique development and applications presented in Papers I-V. In Chapter 2 the laws describing natural background radiation are recapitulated and the near-infrared diode laser sources are discussed in connection with passive and active gas monitoring. Infrared spectroscopy, absorption, emission and scattering issues is discussed in Chapter 3. The gas-correlation imaging principle will be explained and simulations of diffraction patterns from models of aerosol particles will be presented. A survey of infrared imaging detectors to come and those used in this work will be presented in Chapter 4. The optical design considerations, when constructing the gas-correlation telescope and the aerosol particle sensing instrument using a ray-tracing program, are discussed in Chapter 5. Gas image processing aspects will be described in Chapter 6 together with noise issues and gas detection limits. In Chapter 7, examples are given of some applications where we have found the gas-correlation imaging particularly useful. Specific gases especially suitable for detection and imaging with the gas-correlation methods are tabulated and some future applications will be discussed.

## 2. Infrared radiation sources

### 2.1 Natural background radiation

Electromagnetic radiation is a wide-reaching concept with many names. The wavelength is the only primary difference between radiation towards the left and right in Fig. 3. The interaction of electromagnetic radiation with matter is, however, strongly wavelength dependent, and causes different secondary effects which we observe with our sensors. Another aspect of short- or long-wavelength radiation is that the resolution of an image created with electromagnetic radiation is inversely proportional to the wavelength. Thus, the resolution of an infrared image is less than the resolution of a visible image.

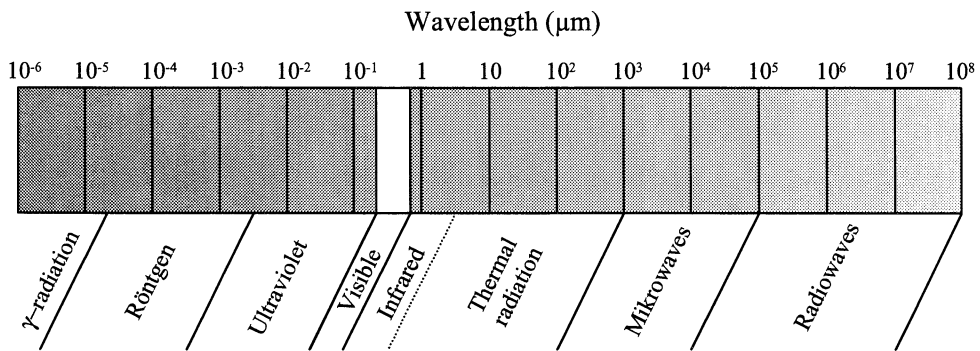


Fig. 3. The electromagnetic spectrum.

Radiation impinging on a surface can either be reflected, absorbed or transmitted, processes which are characterized by the coefficients  $r_\lambda$ ,  $a_\lambda$  and  $t_\lambda$ , respectively. Independent of the wavelength ( $\lambda$ ) and according to energy conservation considerations:

$$r_\lambda + a_\lambda + t_\lambda = 1, \quad (2.1)$$

i.e., all the radiation interactions probabilities sum up to one. If the reflectance and the transmittance coefficients are both zero, all the energy will be absorbed and the temperature of the object will increase. Objects in thermal equilibrium with the surrounding will have to emit exactly the same amount of energy as they absorb; in other words, the spectral emissivity is equal to the spectral absorptance at any specified temperature and wavelength. The emissivity,  $\epsilon$ , is defined as the ratio of the spectral radiant power from an object to that from a blackbody at the same temperature and wavelength. A blackbody with a natural background temperature of 300 K radiates energy according to the Planck's radiation law with a spectrum peaking at 10 μm. The Planck radiation law is

$$\frac{dI_{\lambda}}{d\lambda} = \frac{2\pi hc^2}{\lambda^5 \left( e^{\frac{hc}{\lambda kT}} - 1 \right)}, \quad (2.2)$$

where  $dI_{\lambda}/d\lambda$  is the spectral radiant exitance in  $\text{W}/\text{m}^2$  at the wavelength  $\lambda$ ,  $h$  is Planck's constant with a value of  $6.626 \cdot 10^{-34}$  Js,  $c$  is the speed of light,  $k$  is Boltzmann's constant with a value of  $1.38 \cdot 10^{-23}$  J/K and  $T$  is the temperature of the blackbody. Curves of blackbody radiation in the temperature range 223-313 K are shown in Fig. 4. These curves reflect the background temperatures prevailing when passive gas monitoring is performed.

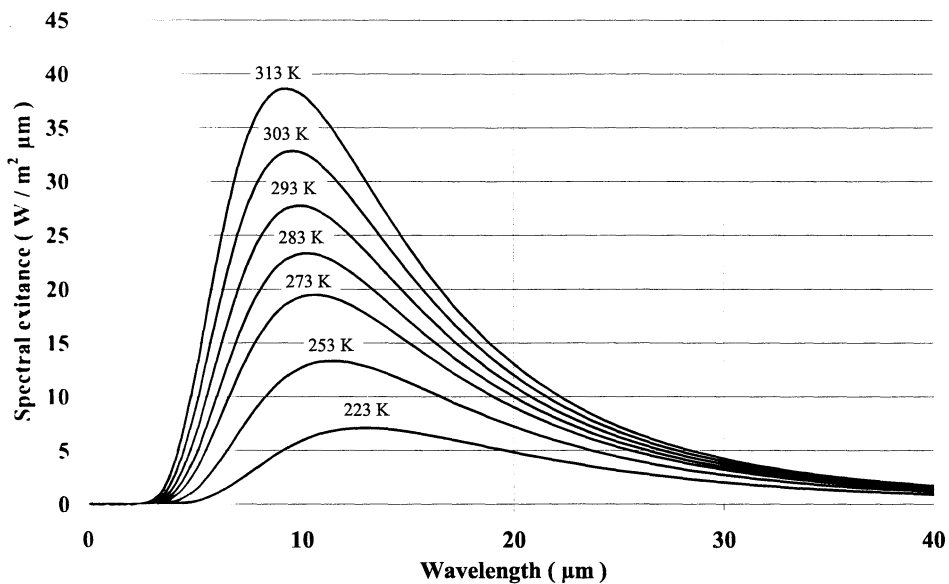


Fig. 4. Blackbody radiation from 223 K to 313 K. Notice that the peak spectral radiance is shifted towards shorter wavelengths with increasing temperature.

An object having an emissivity of 1 is a blackbody radiator by definition. If the emissivity is a constant less than 1, the object is called a gray body and if the emissivity varies over an extended wavelength region, as is the case for real objects, then the object is denoted a selective radiator. The total power/area produced by a radiator at a temperature  $T$  is given by the Stefan-Boltzmann law

$$E = \varepsilon \sigma T^4, \quad (2.3)$$

where  $E$  has the dimension  $\text{W/m}^2$ ,  $\varepsilon$  is the emissivity and  $\sigma$  has a value of  $5.67 \cdot 10^{-8} \text{ W/m}^2 \text{ K}^4$ . Stefan-Boltzmann's law is derived by integrating the Planck radiation law over the wavelengths from zero to infinity. The total rate of emission of photons/area produced by a radiator at temperature  $T$  is

$$N = \varepsilon \sigma_{ph} T^3, \quad (2.4)$$

where  $N$  has the dimension photons/s  $\text{m}^2$ , and  $\sigma_{ph}$  has a value of  $1.5202 \cdot 10^{15} \text{ photons/s m}^2 \text{ K}^3$ . Eq. 2.4 is obtained by dividing the Planck radiation law with the energy of a photon and then integrating over the wavelengths.

The color of heated objects is not depending on the object material but on the temperature of the surface. Wien's displacement law describes that the peak power is shifted towards shorter wavelengths if the object is heated;

$$\lambda_m T = C, \quad (2.5)$$

where  $\lambda_m$  is the wavelength in  $\mu\text{m}$  where the Planck radiation curve has its maximum value and the constant,  $C$ , is  $2898 \mu\text{m K}$ .

At background temperatures (300 K), the materials do not glow in the visible region. The contrast in visible light photography is governed by the differences in reflectance and transmittance of the objects. An important aspect of infrared imaging is that the contrast is governed by the temperature distribution of the objects but also by the wavelength dependent emissivity of the objects. To use natural background radiation for imaging is always favorable both in visible light photography and in infrared radiation imaging (thermography). By combining a visible image with an infrared image, very useful information is frequently obtained.

## 2.2 Artificial infrared radiation

An ordinary incandescent lamp is also an infrared radiation source. The tungsten filament inside the lamp glows at 3000 K and the power spectrum is peaked according to the Wien formula at around 970 nm. According to Planck's radiation law, we expect to find powerful infrared radiation in a tail for longer wavelengths. This is not what is observed, however, because the optical crown glass of the lamp only transmits radiation with wavelengths between 400 nm and 2  $\mu\text{m}$ . The observed infrared power spectrum peak, at approximately 8  $\mu\text{m}$ , is instead originating from the heated glass surface. The Nernst glower is in principle an incandescent lamp without the glass, but this approach suffers from fast oxidation of the filament. Recently, work has been done to use the methods of lamp

production to produce infrared lamps with sapphire and zinc selenide windows fused together with the lamp glass [28]. An infrared heater can be used as a large source of radiation. The heating component is made of a resistance alloy rod and it is optimized to give radiation in the same region as humans emit and absorb radiation, which is at a temperature of 300 K peaked at a wavelength of 10  $\mu\text{m}$ .

A completely different class of radiation sources is formed by lasers. The laser sources are frequently quite sophisticated and complex. The most used laser source, the semiconductor diode laser [29,30], has in its spectroscopic variety a need for a highly stabilized power supply and temperature control to 1/100 of a degree. Lasers are monochromatic and this is an advantage in many cases but often also a problem due to the formation of interference fringes in an optical setup, especially in the infrared region. In the present work a near-infrared diode laser radiating at 780 nm has been used as the light source in an aerosol particle sensor and imager, and two near-infrared diode lasers radiating at 760 nm and 980 nm have been used to produce difference-frequency radiation at 3.4  $\mu\text{m}$  in an experiment of simultaneous measurements of methane, oxygen and water vapor.

### *2.3 Near-infrared diode lasers*

The development of diode lasers is mainly driven by the telecommunications and IT industries. The diode lasers are used to read and store data on mass storage media. A fast emerging market is the broad bandwidth data communication with optical fibers. We have explored the mass-produced compact disc diode lasers in spectroscopy applications, much because of their compact size and low price as compared to traditional lasers for spectroscopy.

The near-infrared diode laser operating at 780 nm has a typical dimension of  $1 \times 3 \times 400 \mu\text{m}^3$ . It is comprised of four integrated building blocks, a p-n junction, a waveguide and two laser resonator end facets. The diode laser capsule also includes a built-in photo diode, which is used for monitoring of the laser output power. The electromagnetic field output has a polarization ratio of 100 : 1, at the normal operating current. The population inversion needed for laser action is produced by reversing the polarity of the p-n junction, as shown in Fig. 5. The injected charge carriers recombine in the active region and photons with the same energy as the bandgap ( $E_g$ ) are produced. The bandgap is the electric potential difference between the conduction band and the valence band and it can be tailored to a quantum well which confines the charge carriers. The statistical fluctuations of the bandgap potential are lowered as compared to a p-n junction without a quantum well. The net effect of creating quantum wells inside the bandgap is the resulting single mode lasing at a lower threshold current which is interesting for spectroscopy.

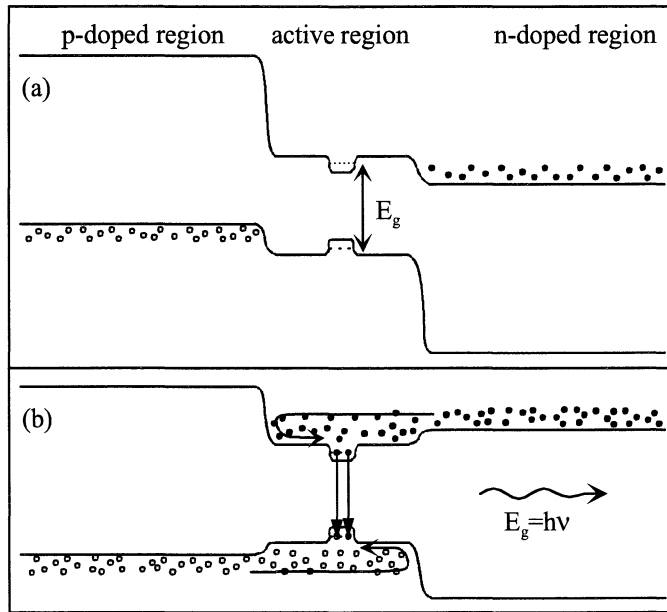


Fig. 5. Energy band diagrams of a p-n junction, (a) at thermal equilibrium and (b) under high injection condition.

Near-infrared diode lasers are based on an aluminum gallium arsenide (AlGaAs) crystal with a refractive index of 3.6, which makes the reflectance of the laser resonator facets to air  $((3.6-1)/(3.6+1))^2 = 0.32$ . GaAs has a direct bandgap, meaning that no lattice vibrations are needed to create a photon from the annihilation of charge carriers. When a photon is created in a direction inside the waveguide normal to the  $1 \times 3 \mu\text{m}^2$  facets, that photon will be reflected back and this starts the laser action, if the frequency is in resonance with the  $400 \mu\text{m}$  long resonator. The created electromagnetic field emerging at the output facet is highly divergent ( $30^\circ \times 10^\circ$ ) due to the small dimension as compared to the wavelength, and it must be collimated by a lens to produce an elliptical laser beam. The infrared source is now ready to be used, it is monochromatic, it has a coherence length of a few mm, it diverges by 2 mrad after collimating and the power can be as high as 0.3 W from a single-stripe diode laser.

#### 2.4 Difference-frequency generation with near-infrared diode lasers

Two of these near-infrared diode lasers can be used to create an infrared beam in the mid-infrared region. In this work, quasi-phase matching in an PPLN (Periodically Poled Lithium Niobate) crystal was utilized [31-38]. The crystal is responding to the incoming near-infrared radiation by the polarizability of the material and the wave vectors must fulfill the energy conservation condition,  $1 / \lambda_3 = 1 / \lambda_2 + 1 / \lambda_1$ . For efficient frequency conversion it is also necessary that

the phase relationship between the waves is maintained over the whole interaction length, i.e.  $k_3 = k_2 + k_1$ . In Paper IV we used one laser at  $\lambda_3 = 760$  nm and one at  $\lambda_2 = 980$  nm to produce a beam at  $\lambda_1 = 3.4$   $\mu\text{m}$ , for simultaneous measurements of oxygen, water vapor and methane.

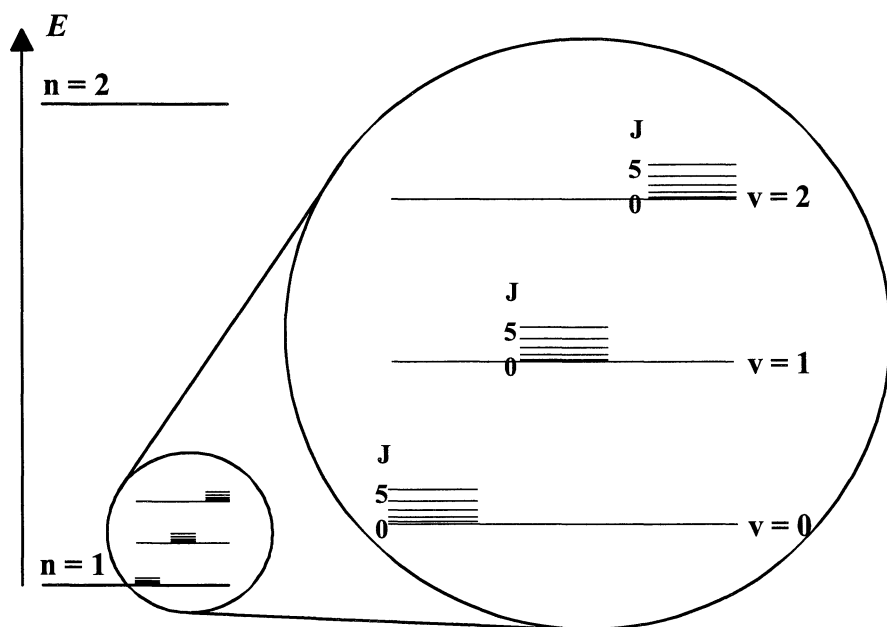
### 2.5 *Passive versus active remote-sensing methods*

Successful passive gas imaging in the infrared region is depending on parameters that we cannot change, such as a high atmospheric transmittance, the integrated absorbance or emittance of several spectral lines, and as the driving force a temperature difference between the gas and the background. On the other hand, we can optimize the system response and the infrared radiation gathering power of the receiving telescope. A successful infrared thermographer will also work hard in finding the best perspective and object, in analogy with a visible light photographer. Two modes of operation are possible. If the gas is imaged against a cold background, we image the gas emission and if the gas is imaged against a warm background, we monitor gas absorption. The source of radiation is the natural background, and all our efforts can be put into the detection side, which makes the setup practical and compact compared to active techniques, where the source side often is complex and costly. The passive technique we have developed has a path-integrated absorption detection limit of a few ppm x m (1 part per 10<sup>6</sup> times meter).

Active laser techniques for gas detection uses an intense infrared source, which is frequently fine-tuned to a spectral line but it need not be one of the fundamental molecular vibrational-rotational transitions. The spectral radiance of a laser source is so large that the temperature difference between the gas and the source can be regarded as infinite. A 10 mW diode laser has approximately a million times higher radiance than the peak Planck radiation at 300 K. Monochromatic laser radiation is the key to gas concentration detection limits of a few ppb x m, but it is also responsible for interference fringes and, in the imaging case, speckle problems. The interference fringes can be handled by using optical isolators or by slightly tilting the optical components. For imaging purposes, the laser beam illuminates a gas and the background. Reflection from the background comes in phase with scattered light from some parts of the surface and out of phase from other parts of the surface. This results in a speckled image. The high output intensity from an illuminating laser makes eye safety a problem in for example an industrial site. The non-uniform far-field cross section of the laser beam is varying over distance and a special lens must be used to minimize this problem. The target back-scattering background should preferably be a diffusely scattering object. All these aspects together make practical *active* gas imaging questionable [14].

### 3. Infrared spectroscopy

The discovery of infrared radiation is credited to Herschel in 1800. The experiment he performed was beautiful in its simplicity. A glass prism was arranged to separate the colors in white light from the sun. He wanted to measure the temperature of the colors and discovered that the temperature was increasing from violet to red. After this observation, he decided to measure the temperature just beyond red and found that the temperature was even higher. The radiation he discovered was later called infrared. This was observed although it is known that the solar spectrum peaks at 500 nm, however, since the dispersion of a glass prism is very low at infrared wavelengths, all such wavelengths are concentrated into the same direction. The human eye cannot detect infrared radiation but the vicious pit snake, hunting mice against the cold desert sand during night, can. The human eye is sensitive to energy quanta in what we call the visible part of the spectrum (400-700 nm), corresponding to a molecular electronic transition, whereas molecules also absorb and emit infrared radiation quanta by transitions between vibrational-rotational energy levels.



**Electronic energy levels      Vibrational- and rotational levels**

Fig. 6. The energy difference between electronic transitions and vibrational-rotational transitions. The electronic energy levels are denoted by  $n$ . The vibrational energy levels are denoted by  $v$  and the rotational energy levels are denoted by  $J$ .

The energy difference between an electronic transition and a vibrational-rotational transition is frequently one to two orders of magnitude, as exemplified in Fig. 6.

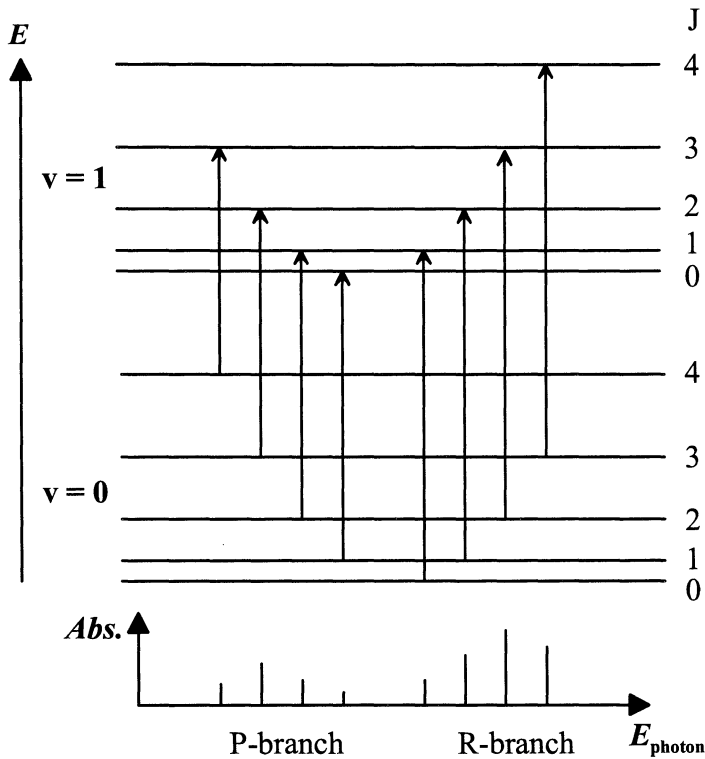


Fig. 7. Quantum vibrational/rotational transitions.

An example of vibrational- and rotational transitions is shown in Fig. 7, and infrared absorption of photons create a spectrum as shown in the lower part of the figure. At natural background temperatures (300 K) the magnitudes of the spectral lines are distributed as shown in the figure. If the temperature increases, a redistribution of states to higher  $J$  quantum numbers occurs, and the resulting spectral line magnitude would be shifted to the left for the P-branch ( $\Delta J = -1$ ) and to the right for the R-branch ( $\Delta J = +1$ ). In order to simulate the absorption spectra of atmospheric gases, the molecular spectroscopy database HITRAN, which contains the absorption line strength parameters of about one million individual vibrational-rotational absorption lines of 37 gases, has been used during this work [39]. Each spectral line in the database contains 14 entries, and they are: the molecule formula, isotope type, transition frequency, line intensity, transition probability, air-broadened halfwidth, self-broadened halfwidth, lower state energy, temperature coefficient for air-broadened linewidth, upper and lower state global quanta index, upper and lower state quanta, error codes and reference numbers. An

example of a simulated HCl spectrum is shown in Fig. 8(a). For comparison a FTIR spectrometer recorded spectrum from the database Qasoft is shown in Fig. 8(b), [40]. The most abundant isotope  $^{35}\text{Cl}$  (76%) is responsible for the peaks of highest absorbance values and the less abundant isotope  $^{37}\text{Cl}$  (24%) is responsible for the peaks with lower absorbance values slightly shifted to the left. The molecule with the heavier isotope thus has less vibrational-rotational energy stored.

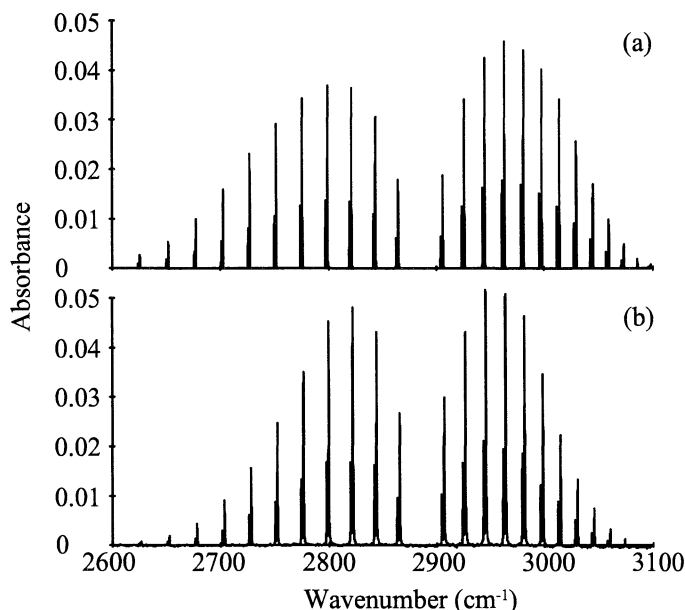


Fig. 8. Simulated absorbance spectrum of 100 ppm x m hydrochloric acid, HCl, using HITRAN and Lorentz lineshape convolution (a). FTIR recorded HCl spectrum with a resolution of  $0.5\text{ cm}^{-1}$  of 100 ppm x m in 1 atm  $\text{N}_2$  at  $25^\circ\text{C}$  (b) [40].

The transmission of light through a medium can be expressed by the Beer-Lambert law

$$I_t = I_i \cdot e^{-OD}, \quad (3.1)$$

where  $I_i$  is the incoming light intensity,  $I_t$  is the transmitted intensity after passing the medium and  $OD$  is the optical depth. The transmission and the optical depth are connected by  $T = I_t / I_i = e^{-OD}$ .

If the incoming light  $I(\nu)$  is monochromatic, i.e.,  $\nu$  has a constant frequency ( $\text{cm}^{-1}$ ), and the light pass through a medium consisting of one molecular gas, we are able to write the light intensity change,  $dI$ , through a gas path of length,  $dx$ , as

$$dI = -\alpha(\nu)I dx, \quad (3.2)$$

where  $\alpha(\nu)$  is the linear absorption coefficient ( $\text{cm}^{-1}$ ). The transmitted intensity  $I_t$  can be calculated by integrating over all the small intensity changes,  $dI$ , through the whole homogenous sample,

$$\int_{I_t}^{I_i} \frac{dI}{I} = -\int_0^L \alpha(\nu) dx, \quad (3.3)$$

where  $L$  is the total path length. The situation is depicted in Fig. 9.

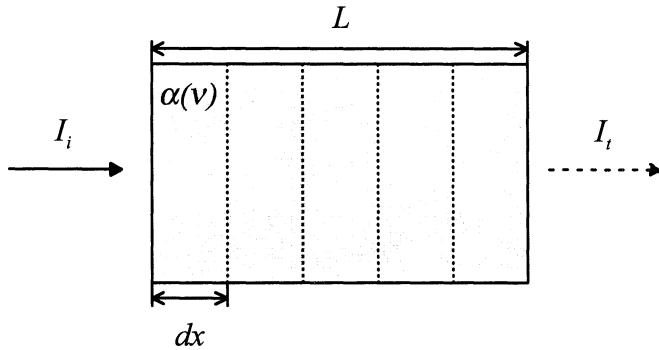


Fig. 9. The transmission of monochromatic light through a sample of absorbing molecules can be derived by dividing the sample into small slices,  $dx$ .

The solution to Eq. 3.3 is the Beer-Lambert law for monochromatic light passing through one molecular gas,

$$I_t = I_i \cdot e^{-\alpha(\nu)L}. \quad (3.4)$$

It is seen from Eq. 3.4 that the path-integrated intensity decrease exponentially with the thickness of the gas. If there are many different gases present in the sample then the total composite transmission is calculated by adding the individual optical depths,

$$OD = (\alpha_1(\nu) + \alpha_2(\nu) + \dots) \cdot L. \quad (3.5)$$

A parameter of importance in this work is the absorbance, which is related to the optical depth as being equal to  $OD / \ln 10$ , or it can be related to the transmission as  $\log(1/T)$ . The essence of the Beer-Lambert law is that the absorbance is proportional to the path-integrated concentration.

The absorption coefficient,  $\alpha(\nu)$ , is related to the absorption cross-section of the molecules,  $\sigma(\nu)$ , as

$$\alpha(\nu) = \sigma(\nu)N, \quad (3.6)$$

where  $N$  is the absolute gas concentration in molecules/cm<sup>3</sup> and the dimension of  $\sigma(\nu)$  is cm<sup>2</sup>/molecule. The strength of a single absorption line is given by integrating the absorption cross-section over the frequency range of the line. The absorption cross-section can also be related to the molecular line strength,  $S$ , by

$$\sigma(\nu) = S g(\nu-\nu_0), \quad (3.7)$$

where  $g(\nu-\nu_0)$  is the normalized lineshape function, and  $\nu_0$  is the central frequency of the line. There are three main lineshape functions, namely the Lorentzian which is used for pressure broadening calculations, a Gaussian function is used for Doppler broadening and a Voigt profile is used for a composite of both Doppler and pressure broadening. The Lorentzian lineshape was utilized in the HITRAN simulations of path-integrated absorbance, performed in Paper II for calibration of ammonia gas images. The Lorentzian lineshape, which is caused by the collisions between the molecules, is broad compared to the linewidth of a near-infrared diode laser, which is often swept in order to register the whole line profile. In the gas-correlation technique, see Section 3.1, there is no need for spectral scanning as the whole spectrum is interrogated simultaneously. The difference-frequency generated radiation, see Paper IV, was also used in measurements at mainly atmospheric pressure, therefore only the Lorentzian line profile,  $g_p$ , will be recapitulated here:

$$g_p = \frac{\Delta\nu_p}{\pi} \frac{1}{(\nu - \nu_0)^2 + \Delta\nu_p^2}, \quad (3.8)$$

where  $\Delta\nu_p$  is the pressure broadened halfwidth at half maximum in wavenumbers and  $\nu_0$  is the central frequency of the line. The halfwidth depends on the partial pressure of the gas itself (self broadening) and the partial pressures of other gases. Temperature also affects the halfwidth, and at normal background temperatures, for passive gas-correlation imaging, the effect of a temperature difference of 10 degrees ( $T_0=296$  K and  $T=306$  K) decreases the halfwidth of for example methane with 2.5% according to

$$\Delta\nu_p(T) = \Delta\nu_p(T_0) \left( \frac{T_0}{T} \right)^n, \quad (3.9)$$

where  $n = 0.75$  for methane. Other line parameters that are affected by the temperature are the line strength due to the Boltzmann population distribution in the vibrational-rotational energy levels and the Doppler broadening which is due to the thermal motion of the molecules. Doppler broadening is, however, negligible compared to the atmospheric pressure broadening.

Since the infrared spectra during this work were observed under thermal equilibrium conditions in the lower troposphere, we need only to consider the distribution of molecules over the different quantum states under thermal equilibrium. Recently, however, accurate sensing of the vertical composition of the atmosphere (especially the thermosphere) from satellites with high resolution spectrometers, when non-thermal equilibrium conditions prevail, call for more detailed line parameters in the molecular spectral databases [41].

The distribution of diatomic molecules over the different quantum vibrational states is proportional to the law of Maxwell-Boltzmann;  $e^{-E/kT}$ , where  $E$  is the energy of the classical vibrating oscillator and  $k$  is Boltzmann's constant. With a temperature of 300 K almost all the molecules are vibrating in the quantum ground state of the vibrating oscillator, and the number of molecules in the higher vibrational levels falls off quite fast. Even at temperatures as high as 1000 K, practically all the transitions that are observed in infrared absorption spectra of diatomic molecules (e.g. HCl and CO) originate from the ground state vibration [42].

The situation is different for the rotating oscillator, here  $hB \ll kT$ , as shown in Fig. 6.  $B$  is a rotational constant which depends on the moment of inertia of the molecule ( $B = h/8\pi^2\mu r^2$ , where  $\mu$  is the reduced mass). The distribution of molecules over the different quantum rotational states is proportional to the degeneracy of the total angular momentum state,  $2J+1$  multiplied with  $e^{-BJ(J+1)hc/kT}$ . This is the solution to the Hamiltonian of a rigid rotator model and it is valid for most diatomic molecules:

$$N_J \propto (2J+1)e^{-BJ(J+1)hc/kT} \quad (3.10)$$

Here  $N_J$  is the number of molecules in the rotational level  $J$ . By searching for a maximum to the expression we find that

$$J_{\max} = \sqrt{\frac{kT}{2Bhc}} - \frac{1}{2} \quad (3.11)$$

The interesting result is that  $J_{max}$  increases with increasing temperature,  $T$ . This expression can also be used to explain the band line intensity variation as seen in Fig. 8.

If a molecule is capable of absorbing energy, it is also equally well capable of emitting the same quantum of energy. Molecules in a large reservoir at pressures around the atmospheric one are exchanging vibrational and rotational energy so that the molecules are in thermal equilibrium with each other and the walls of the reservoir. If we inject molecules with more energy stored in their vibrations and rotations into the large reservoir, they will by relaxation [43] (time scale: a few  $\mu\text{s}$ ) and depending on the mixing (time scale several seconds) get into thermal equilibrium with the molecules in the reservoir.

Many elementary gases have useful absorption features in the fundamental infrared region (2.7-20  $\mu\text{m}$ ). The strong vibrational-rotational bands for methane are positioned at 3.3  $\mu\text{m}$  and at 7.7  $\mu\text{m}$ , as shown in the FTIR recorded spectra of Fig. 10.

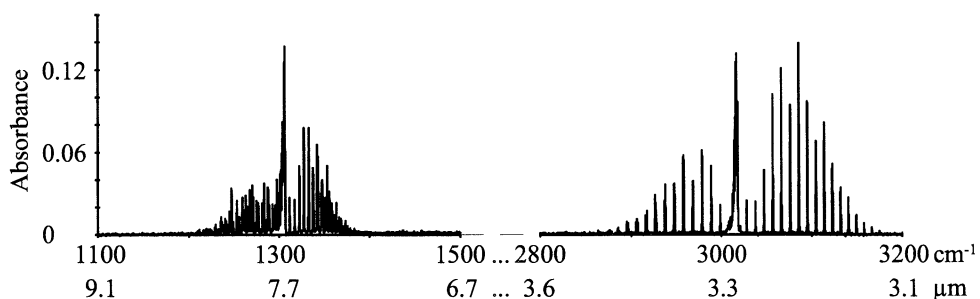


Fig. 10. FTIR recorded methane spectra at 100 ppm x m in 1 atm.  $\text{N}_2$  [40]. Both spectra are shown over a spectral range of  $400 \text{ cm}^{-1}$ , for total integrated absorbance comparison in the spectral regions of long-wavelength sensitive cameras ( 7-14  $\mu\text{m}$  ) and short-wavelength sensitive infrared cameras ( 3-5  $\mu\text{m}$  ).

The radiative balance between the earth and the space background is maintained by the sun and the transmittance of the atmosphere, see Fig. 11. The balance is affected by an increasing amount of, e.g., carbon dioxide and hydrocarbon gases, affecting otherwise reasonable transparent regions. The gas-correlation infrared camera optics are antireflection coated for high transmittance in the same spectral windows as the infrared transparent regions of the earth atmosphere, so by definition infrared cameras are suitable greenhouse gas detectors.

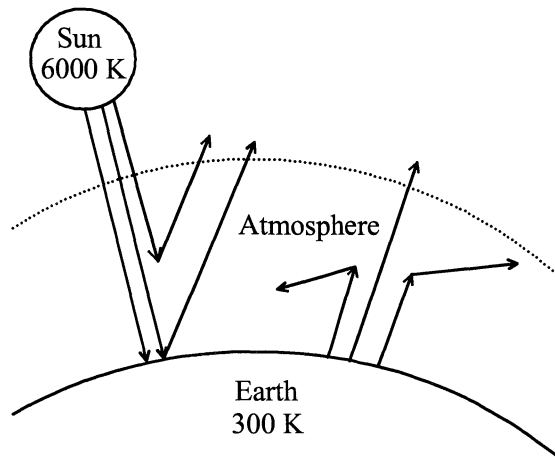


Fig. 11. The sun radiates onto the earth, and one third is reflected back from clouds, the atmosphere and the surface. The remaining two thirds are absorbed in the atmosphere and at the surface. Thermal equilibrium is needed for a stable temperature on earth, which is the case if the same amount is transmitted out from the earth and the atmosphere.

The contrast of a gas-absorption image can be enhanced by including a broad bandpass filter inside the camera in front of the detector. However, due to spectral interference with other gases and water vapor it would be impossible to distinguish one gas from the others. Even if there is only one gas present in the scene, the gas absorption would seem to vary because of a varying natural background of temperatures and emissivities. A narrow bandpass filter positioned at the same spectral location as one spectral line of the gas of interest could be an alternative, but in this case the number of natural background photons absorbed by the detector and converted to electrons would be less than the number of electrons created by noise. The two-dimensional extension to the gas-correlation principle has been used in this work to provide a solution to the practical selective gas imaging problem.

### 3.1 The gas-correlation principle

Already in 1943 Luft described a spectrometer which was based on the gas-correlation principle [44]. Later, the principle was also refined [45-50] and adapted to a space-borne instrument [22] and LIDAR measurements [51].

The gas correlation idea is as simple and straightforward as spectroscopy ever can be; let us use the gas itself as its own spectral filter. Tabulated absorption line information is therefore in principle not needed, neither are the dispersive optical components that are used in most spectrometers. The principle relies on the

inherent and basic physical qualities of molecules. A line-of-sight measurement will be described here, see Fig. 12, and in the next section the principle will be extended to the imaging technique.

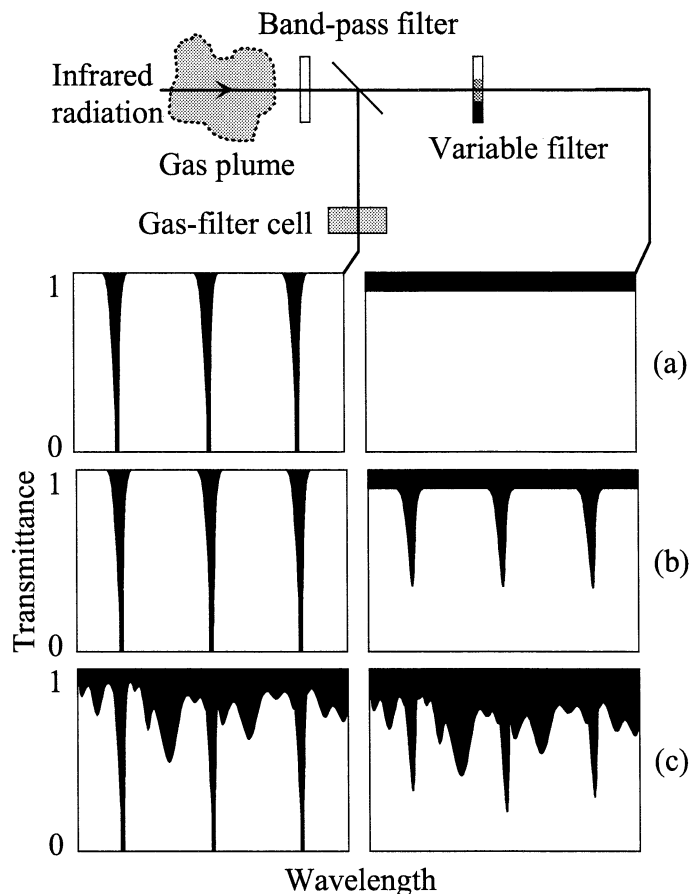


Fig. 12. The gas-correlation principle. No external gas plume present (a). Only gas of interest in plume (b). Gas of interest and interfering gas in plume (c).

The incoming infrared radiation is sent directly to a detector or through a cell containing the gas of interest at such high a concentration that little or no light can pass at the absorption wavelengths. An infrared bandpass filter is inserted to reduce the spectral range to the one where the gas absorbs in order to increase the contrast between the two arms. With no external gas present in the atmosphere between the infrared source and the instrument, a variable transmission filter in the direct arm is adjusted so that equal intensities are obtained in the chosen spectral region cut out by the bandpass filter (a). If an atmospheric pollution plume is present the signal in the gas-filter cell arm is not affected (except for a minor broadening of the

absorption lines) because no more than full absorption can be obtained. The incoming infrared radiation in the other, direct arm is reduced because of absorption lines in the plume. The arising imbalance signal is a measure of the gas concentration in the plume (b). Notice that the presence of interfering gases does not affect the concentration measurements, as long as there is no spectral crosstalk (c) [45].

A special problem arises when the technique is used from satellites. The column of air from the satellite down to the earth has a pressure dependence, which yields a height varying molecular lineshape. The MOPITT instrument on the Terra satellite uses a length-modulated gas-filter cell. An alternating signal is detected when different optical gas paths are switched in and out. The measurements are restricted to the troposphere where the methane gas is in uniform mixing ratio, therefore the vertical distribution is of secondary importance and the total column of gas is deduced [23].

### 3.2 The two-dimensional extension to the gas-correlation principle

The extension of the gas-correlation principle to imaging relies on an infrared sensitive camera equipped with a filter for the selection of specific molecular infrared bands, a gas cell in front of one of the openings of a split-mirror telescope, and a CCD sensor.

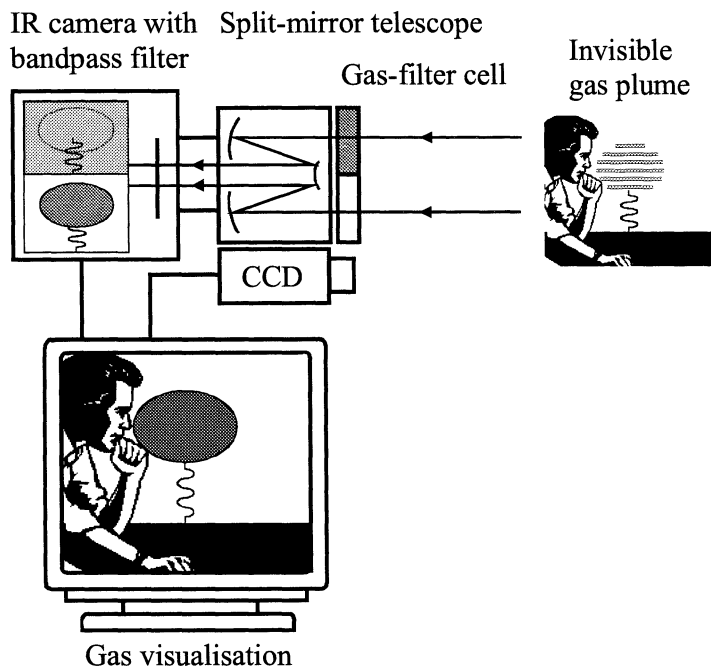


Fig. 13. The two-dimensional extension to the gas-correlation principle.

and processing of the simultaneously captured images according to the gas-correlation scheme on a PC, as indicated in Fig. 13. The image processing will be described in detail in Chapter 6. The result is presented as a color-coded image of a specific gas merged with a visible image, also in the presence of several other gases, and a movie of the gas flow can be produced with up to 30 frames per second. Our first measurements on gas flows, in 1996, were performed using a camera sensitive in the 3-5  $\mu\text{m}$  region with a slightly heated screen as a thermal background [Paper I]. More recently, a camera sensitive in the 8-12  $\mu\text{m}$  region has been employed, enabling passive gas imaging through absorption of the natural thermal background radiation [Paper II]. Field studies have been performed on open gas flows of ammonia, methane, and ethene, set up to simulate leakage from a gas tanker. The method has also proved itself useful when searching for leaks at a polyethene plant and in visualizing ethene escaping from flares at the same location [Paper III].

### *3.3 Gas concentration calibration*

There are two possibilities to derive the gas concentration from the gas images. The standard addition method can be used to calibrate the system with gas-filter cells in the common light path. The cells are filled with known concentrations and placed in front of the same background as the external gas. This calibration methodology has not been used in this work due to some practical considerations. The need for several expensive gas-filter cells placed in front of the same background without having the possibility to turn off the external gas would mean that the external gas could easily destroy the calibration by spatial variations of the external gas concentration. The Beer-Lambert law is valid for monochromatic light but we are interrogating a complete absorption band structure and this calls for several gas-filter cells as the calibration curve is non-linear. The method that we have used is based on the molecular spectroscopy database HITRAN. Depending on the spectral line positions, line strengths and the pressure broadening, among other parameters, the database can be used to simulate real gas absorbance spectrum. This has been done for ammonia gas at concentrations ranging from 0-20000 ppm x m. The background radiation (Planck curve) was convoluted with the system response and the simulated spectra were convoluted with the Planck curve corresponding to the external gas temperature which is assumed to have the same temperature as the surrounding air at thermal equilibrium. The gas-filter cell self emission is convoluted with the corresponding Planck curve and the integrated result is subtracted from the integrated convolution of the external gas. Even if the temperature differs between the external gas and the surrounding air, as in flares, the gas-filter cell has saturated spectral lines which means that the redistribution of vibrational-rotational states to higher J quantum numbers will not affect the result. The resulting convolutions are integrated and divided to obtain the relative transmittance of the gas at a specific temperature difference between the gas and the background.

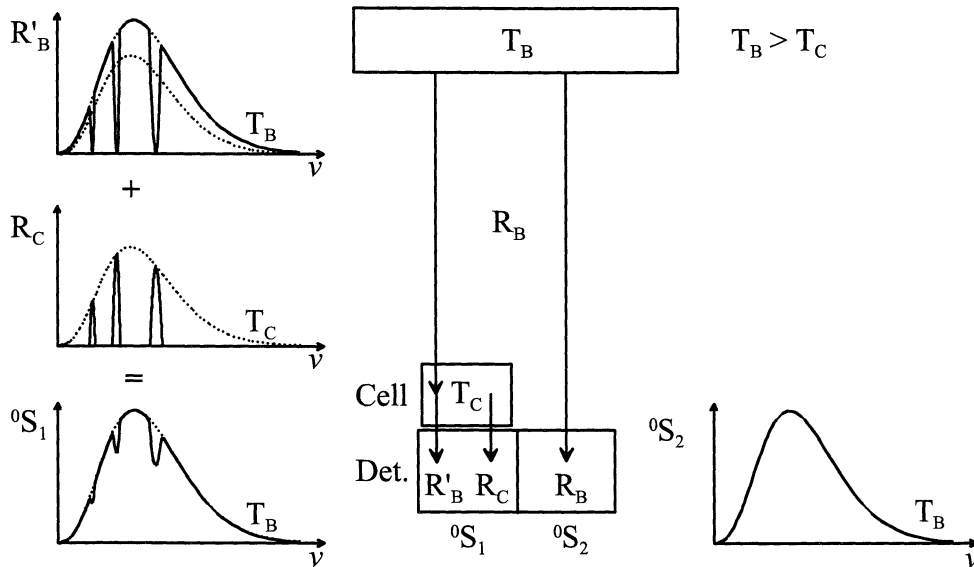


Fig. 14. Schematic view of the spectral radiance,  $R$ , from the background to the formation of two images,  ${}^0S_1$  and  ${}^0S_2$ .  $R_C$  is the self emission from the gas-filter cell gas at a temperature of  $T_C$ .

We consider first the case when no external gas is present in front of a background with a temperature of  $T_B$ , which is larger than the gas-filter cell gas temperature,  $T_C$ , the situation is depicted in Fig. 14.  $R_B$  is the spectral radiance of the background, i.e., in this case a blackbody radiator at a temperature of  $T_B$ . However, the background must not be a blackbody radiator as we divide the images and thus cancel out the background.  $R'_B$  is the spectral radiance after passing the gas-filter cell. Fully saturated spectral lines are due to a high concentration in the gas-filter cell.  $R_C$  is the self emission from the same spectral lines and the radiance values reach up to the same as those from a blackbody radiator at the temperature  $T_C$ . The sum of  $R'_B$  and  $R_C$  is shown as  ${}^0S_1$  in Fig. 14. Thus, the spectral radiance is lowered as compared to the radiance in the direct channel,  ${}^0S_2$ . Now, if an external gas plume is present in front of the background the situation is changed as shown in Fig. 15.

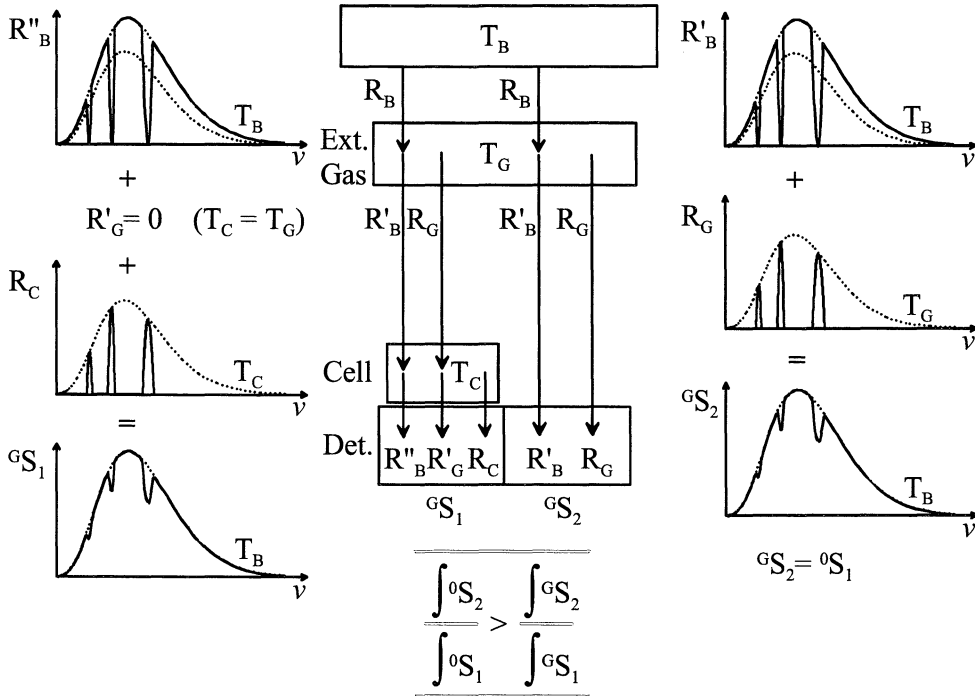


Fig. 15. Schematic view of the spectral radiance,  $R$ , from the background through an external gas plume to the formation of two images,  ${}^GS_1$  and  ${}^GS_2$ .

Here we make the assumption that the gas-filter cell temperature is equal to the external gas temperature,  $T_C = T_G$ . This assumption is valid in most practical cases, which follows from the discussions in Chapter 3. The right-hand side of Fig. 15 is identical to the left-hand side of Fig. 14, if the external gas is optically thick.  $R''_B$  is the spectral radiance after passing through the external gas and the gas-filter cell. A minor broadening of the lines due to the presence of external gas will not affect the resulting signal as the lines are saturated. The gas in the cell will radiate to an amount of  $R_C$ , as in the case with no external gas. The final sum of  $R''_B$ ,  $R'_G$  and  $R_C$  is shown as  ${}^GS_1$  in Fig. 15. A few conclusions can now be drawn from Fig. 14 and Fig. 15. If the background temperature is the same as the gas temperature,  $T_B = T_G$ , then  ${}^GS_1$  integrated over the wavelength region is equal to  ${}^GS_2$  integrated, and no gas can be visualized.  ${}^GS_1$  is independent of the optical density of the external gas, as long as the spectral lines of the gas-filter cell gas are saturated. When the optical density of the external gas is increasing there is an imbalance introduced, the integrated value of  ${}^GS_2$  is decreasing. Finally, what is recorded is the change in the ratio of the integrated radiance in the two images, as shown in the lower box in Fig. 15.

The calibration scheme has been verified experimentally with a gas-filter cell with a known concentration placed in front of a blackbody radiator with temperatures both higher than the gas temperature (absorption mode) and lower than the gas temperature (emission mode), three examples of calibration images are shown in Fig. 16(a-c). Six of these images at different temperatures were used in the calibration procedure of Paper II, Fig. 5.

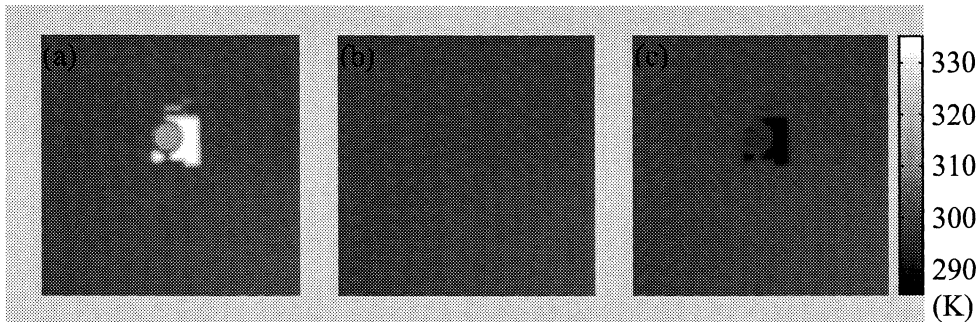


Fig. 16.  $\text{NH}_3$  calibration images. A blackbody radiator with a temperature of 334 K is seen as a white square behind the circular gas-filter cell (a). The blackbody temperature is 296 K in (b), and 285 K in (c). The gas cell was filled with  $\text{NH}_3$  to 1 atm. and the gas temperature was 296 K.

The ammonia gas is absorbing the blackbody radiation in Fig. 16(a). The grayscale value in the gas-filter cell is not a measure of gas temperature, since the gas is a selective radiator. In the next image (b), the temperature of the blackbody is 296 K, which is the same as the surrounding walls. Notice that the ammonia gas is invisible without a temperature difference. In the last image (c), the temperature of the blackbody is 285 K and the ammonia gas is seen in emission. The infrared camera can be calibrated to show a temperature scale but the recorded images are stored with radiance values and these are used in the offset calculation and gas concentration calibration.

The main conclusion from the diatomic theoretical framework in Chapter 3, relevant for gas-correlation imaging, is that while the intensity of the lines vary with temperature the line positions do not vary with temperature and thus a difference between the gas-filter cell temperature and the external gas temperature would not affect the visualization noticeably. It would, however, depend on the saturation of lines in the gas-filter cell, in a way suitable for further investigations. Polyatomic molecules are exhibiting exceedingly more complicated spectra but a virtue of the gas-correlation method is that no spectroscopic database can compete with the gas itself when it comes to where the line positions are, given nearly the same conditions for the external gas as for the gas-filter cell.

A Bomem FTIR spectrometer has been used to measure saturated absorption lines of the gas-filter cell. It was observed that the spectral absorption line wings are important contributors to the totally integrated absorption at high gas concentrations. This makes it impossible to use real FTIR absorbance spectra [40] recorded for one concentration and multiply the spectra with a factor to calculate other concentrations, the line shape information is in that case lost in the noisy background of the spectra. Recordings with a FTIR spectrometer for different gases and concentrations must be performed, or simulated spectra of gases can be utilized to calibrate the camera system.

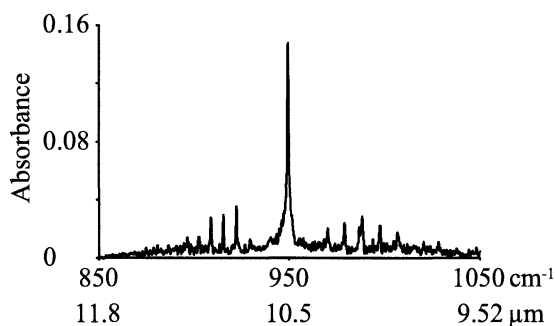


Fig. 17. C<sub>2</sub>H<sub>4</sub> spectrum recorded by the FTIR technique. The path-integrated concentration of ethene was 100 ppm x m in 1 atm. N<sub>2</sub> [40].

Gases that were visualized during this work were methane (Fig. 10), ethene (Fig. 17), nitrous oxide (Fig. 18) and ammonia (Fig. 19). Concentration calibration of path-integrated absorbance for ammonia, as presented in Paper II, was done with the HITRAN database and the array basic programming language GRAMS [52].

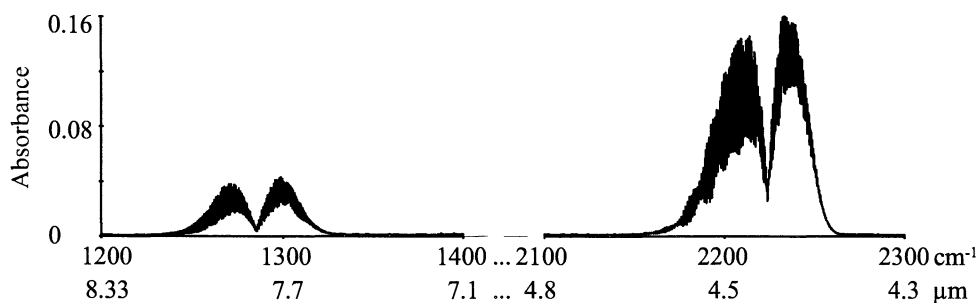


Fig. 18. N<sub>2</sub>O spectrum recorded by the FTIR technique. The path-integrated concentration of nitrous oxide was 100 ppm x m in 1 atm. N<sub>2</sub> [40]. Both spectra are shown over a spectral range of 200 cm<sup>-1</sup>, for total integrated absorbance comparison in the spectral regions of long-wavelength sensitive cameras (8–12 μm) and short-wavelength sensitive infrared cameras (3–6 μm).

An optimal spectrum for passive gas correlation should have large integrated gas absorbance and well separated peaks positioned around  $10\ \mu\text{m}$  (300 K). The nitrous oxide, shown in Fig. 18 has large integrated gas absorbance, especially in the short-wavelength region, but the broad spectrum of overlapping lines can easily be in crosstalk with spectral lines from another gas spectrum. The band position is not optimal, according to the Planck radiation curve in Fig. 4. The spectral radiance from the background is a factor 5 higher for a spectrum positioned around  $10\ \mu\text{m}$  (300 K).

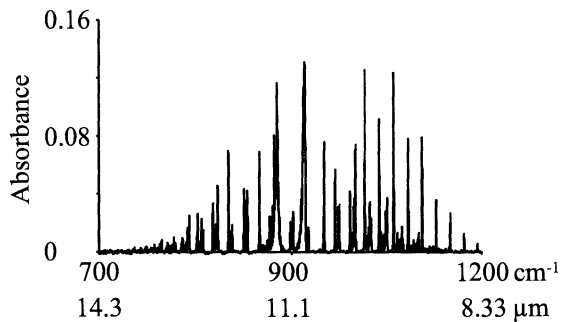


Fig. 19. NH<sub>3</sub> spectrum recorded by the FTIR technique. The path-integrated concentration of ammonia was 100 ppm x m in 1 atm. N<sub>2</sub> [40].

Three examples of band structures that are well suited for gas-correlation imaging are methane, ethene and ammonia. Further suitable gases are tabulated in Chapter 7, Table 7.

### 3.4 Aerosol particle scattering

So far, Chapter 3 has dealt with infrared molecular absorption and emission spectroscopy. In connection with the study of aerosol particles, scattering of light can also be utilized. Scattering of electromagnetic radiation by molecules, aggregates of molecules or particles is related to the accelerated electric charges associated with the scattering object. Huygens' principle states, that a primary wavefront incident on a surface creates secondary spherical wavelets, such that at a later time the primary wavefront is the envelope of these wavelets. Depending on the structure of the scattering medium, radiation is either reradiated in any direction in space or in absorption transferred to the scattering medium as for example vibrational-rotational energy (heat).

The purpose of this section is to pinpoint the main conclusions from diffraction theory that are relevant for the development of an aerosol particle sensing instrument [53,54]. The Mie scattering simulations that were used to create the

extinction model in Paper V will be exemplified. Fraunhofer diffraction will be compared to analyzing fiber shapes with a ray-tracing program (Optics Software for Layout and Optimization, OSLO) based on the geometric-optics approximation and the extension; two-dimensional scalar diffraction theory [55-59]. Pollen grain shape analysis using OSLO will be described.

The scattering of radiation by homogenous spherical particles which are large compared to the wavelength of the incoming radiation can be described by Mie theory. An optical size parameter is defined as  $\alpha = \pi d/\lambda$ , where  $d$  is the diameter of the particle and  $\lambda$  is the wavelength of the light. Mie scattering from 0 to 180 degrees is shown in Fig. 20. The simulations are made according to [57] and [60]. The model can be used to show that the forward-scattered light ( $0^\circ$ ) has the highest magnitude. It is also seen that near-forward scattered light ( $0-20^\circ$ ) is strong compared to scattering in the sidelobes and back-scattering [61].

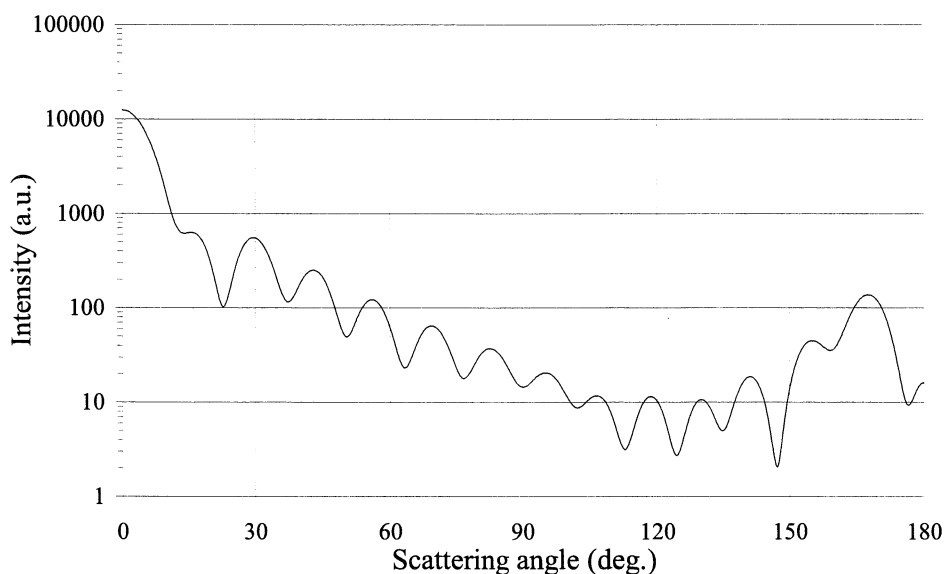


Fig. 20. Spherical particle scattering in forward to backward directions (0 to 180 degrees). The wavelength was 780 nm,  $\alpha = 15$ ,  $n_{\text{sphere}} = 1.5$  and the medium surrounding the sphere had a refractive index of  $n_{\text{medium}} = 1$ . Notice that forward scattered light is 1-3 orders of magnitude larger than light scattered in the other directions.

Mie theory describes only scattering from spherical particles but real particles come in different shapes. The idea behind the aerosol particle sensor developed is as follows: If we measure the influence of one particle by its extinction of light, it is also possible, at the same instance, to capture the near-forward scattered light

from the same single particle. By using such a measurement scheme, the shape and an optical equivalent size of the particle can be derived. Shape information can for example be used to separate *Betula* sp. pollen from *Fraxinus* sp. pollen (i.e. birch from ash) or it can be used to separate fibers from spherical particles, even if the optical equivalent sizes are the same.

The far-field diffraction pattern from a fiber subject to a coherent planar wavefront is a special case of vector diffraction theory, namely Fraunhofer diffraction. The electromagnetic field at a point in the diffraction pattern from a fiber is complementary to that of a single slit according to Babinet's principle [62]. This principle is very useful when tracing rays through a large aperture with a small obstacle. The Fraunhofer far-field diffraction from a single slit is

$$I(\theta) = I_0 \left( \frac{\sin \beta}{\beta} \right)^2, \quad (3.2)$$

where  $I_0$  is the incoming intensity,  $\beta = (kb/2)\sin\theta$ ,  $k = 2\pi/\lambda$ ,  $b$  is the width of the single slit,  $\lambda$  is the wavelength and  $\theta$  is the angle perpendicular to the slit. The intensity has minima, when  $\sin \beta = 0$ , whereupon

$$\beta = \pm\pi, \pm2\pi, \pm3\pi, \dots \quad (3.3)$$

The angular dependence of the diffraction minimum order,  $m$ , can also be written as

$$b \sin\theta_m = m\lambda. \quad (3.4)$$

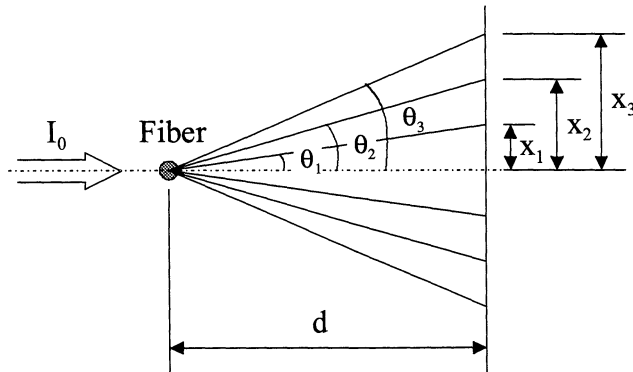


Fig. 21. Intensity minima positions,  $x_1$ ,  $x_2$  and  $x_3$  at a distance  $d$  from the scattering fiber.

The results from calculating the Fraunhofer diffraction from a fiber at distance  $d=100$  mm are shown in Table 1.

Table 1. Fraunhofer diffraction minima, angles and positions.  $\lambda=780$  nm.

Fiber diameter, $b$ ( $\mu\text{m}$ )	$\theta_{m=\pm 1}$ ( $^\circ$ )	$\theta_{m=\pm 2}$ ( $^\circ$ )	$\theta_{m=\pm 3}$ ( $^\circ$ )	$x_{m=\pm 1}$ (mm)	$x_{m=\pm 2}$ (mm)	$x_{m=\pm 3}$ (mm)
10	$\pm 4,47$	$\pm 8,97$	$\pm 13,53$	$\pm 7,82$	$\pm 15,79$	$\pm 24,07$
20	$\pm 2,24$	$\pm 4,47$	$\pm 6,72$	$\pm 3,9$	$\pm 7,82$	$\pm 11,78$

The values of the three last columns in Table 1 should now be compared to the values derived from simulations with OSLO, see Table 2.

Table 2. Simulated diffraction minima 100 mm from the fibers.

Fiber diameter, $b$ ( $\mu\text{m}$ )	$x_{m=\pm 1}$ (mm)	$x_{m=\pm 2}$ (mm)	$x_{m=\pm 3}$ (mm)
10	$\pm 8.07$	$\pm 15,89$	$\pm 24.14$
20	$\pm 4.20$	$\pm 8.07$	$\pm 11.97$

The ray-tracing program uses an extended scalar diffraction theory which agrees well with Fraunhofer theory when the particle size is much larger than the wavelength of the incident radiation [55].

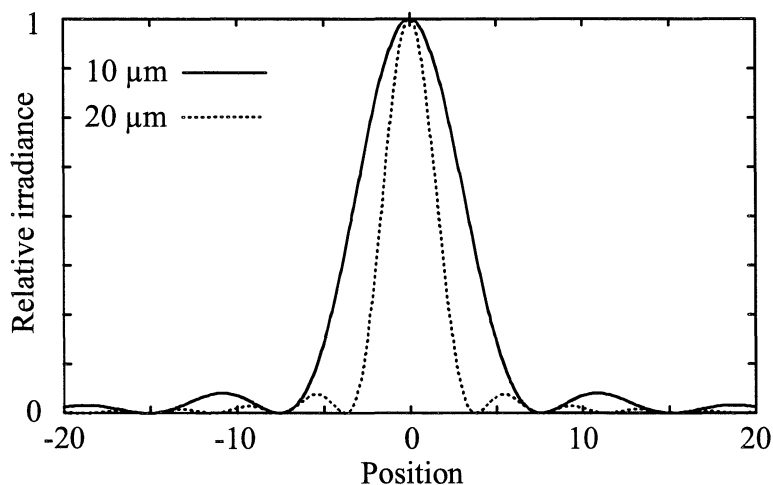


Fig. 22. Diffraction from two fibers, 10 and 20  $\mu\text{m}$  in diameter, simulated with OSLO.

The point spread function is calculated in OSLO with rays emerging from one point in space and the rays are directed to an entrance opening of the optical system. A geometrical wavefront of sufficiently high resolution is needed for the point spread function to converge. The resolution is determined by the number of rays that are traced through the system. The model of an aerosol particle used here is, according to Babinet's principle, a geometrical cross-section of an aperture without depth.

Models of real aerosol particles and fibers were created, in the optics software, and used to simulate the performance of the final prototype instrument. The simulated diffraction patterns were compared to the real diffraction images and they were found to agree well, see Fig. 23.

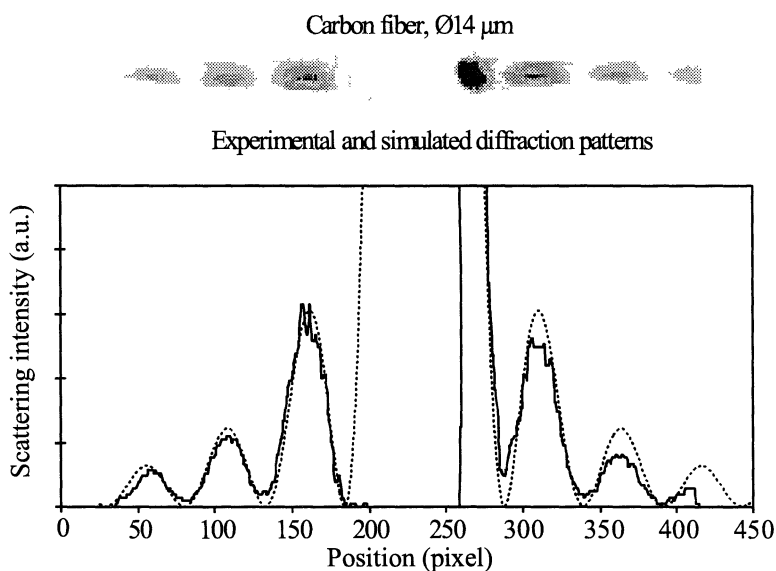


Fig. 23. Experimental diffraction pattern from a fiber with a diameter of  $14 \mu\text{m}$  (top). Integrated intensity of the experimental diffraction pattern, solid line (bottom). Simulated diffraction intensities, dashed line.

Ray tracing the final prototype for simulation of aerosol particle shape makes it possible to predict the diffraction images of specific pollen grains. Elongated fibers are essentially one-dimensional objects and if we would like to simulate the diffraction pattern from a pollen grain, the calculations will have to be two-dimensional. A simulation of *Betula* sp. (birch) and *Fraxinus* sp. (ash) pollen grains results in the perspective diffraction images shown in Fig. 24 and Fig. 25, respectively.

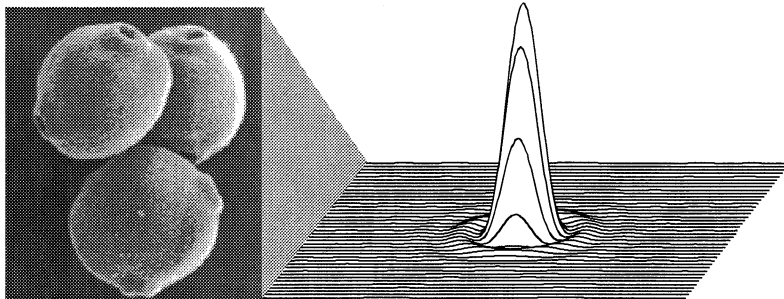


Fig. 24. Electron microscope image of *Betula* sp. pollen and a simulated diffraction pattern in perspective. The diameter ranges from 22-25  $\mu\text{m}$ , the simulation was done for 20  $\mu\text{m}$ .

The shape of pollen grains of *Fraxinus* sp. can be rectangular 19-38  $\mu\text{m}$  x 13-28  $\mu\text{m}$  but also spherical 15-33  $\mu\text{m}$ . *Fraxinus* sp. can also be afflicted with 13-26  $\mu\text{m}$  long tentacles of 0.5-2.5  $\mu\text{m}$  width. The simulation shown in Fig. 25 has been performed for 20  $\mu\text{m}$  x 20  $\mu\text{m}$  square *Fraxinus* sp. pollen grain.

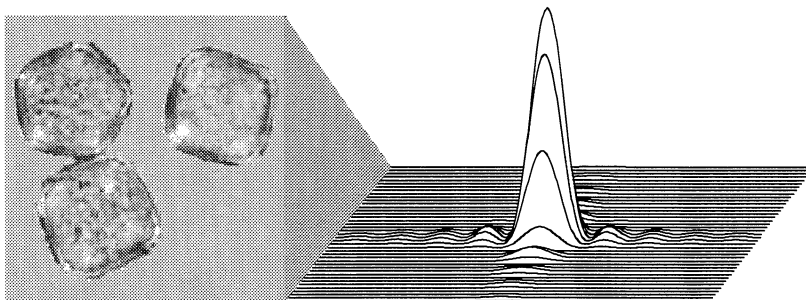


Fig. 25. Electron microscope image of *Fraxinus* sp. pollen and a simulated diffraction pattern in perspective. The simulation was performed for a 20  $\mu\text{m}$  x 20  $\mu\text{m}$  pollen grain.

The geometrical transverse cross-sections, that can be used in the ray-tracing program as aerosol particle models, are built from apertures that can be elliptical, rectangular, triangular and polygons. Two of these special apertures can be combined in the same surface. Several surfaces with special apertures can be combined to simulate several particles in the measurement volume.

## 4. Infrared image detectors

Infrared radiation, also denoted thermal radiation, consists of photons with wavelengths greater than those of photons in the visible part of the electromagnetic spectrum. The infrared photons are thus less energetic, and more difficult to detect. Two principally different physical detector families for infrared photons exist. The first family has members relying on absorption of photons followed by the detection of a secondary effect, for example a resistance change in the absorbing material, and they are called thermal detectors (bolometers). The other family consists of photon detectors, and in these, the annihilation of photons in a semiconductor material creates a detectable current. In addition to the detection of photons, an image is formed either by scanning the field-of-view with a mechanically stable high speed rotating mirror and project the radiation onto a solitary detector or by imaging onto a focal plane array (FPA) of detectors. The detectors using the FPA technology are also called staring arrays and they are the most promising infrared camera detectors undergoing intensive research and development during the last years. In the survey of infrared detectors below we will focus on the imaging detectors used in this work.

### 4.1 Thermal detectors

An ordinary mercury thermometer is a thermal detector using the secondary effect of volume enlargement due to the absorbed infrared photons giving the collective forces of the atoms more vibrational energy and thus more space need. The temperature is read from a scale where zero Kelvin stands for the lowest possible energy stored in the mercury volume. Now, if we would like to create an image of a heated object, we will have to arrange, for example 10 x 10 thermometers in a matrix. All the sensing bodies of the thermometers are placed in the image plane of an infrared transmitting lens. We then note the temperatures and positions of the thermometers. Using a collection of pencils with a scale of nine gray levels, we would be able to represent the temperature image of the object with the dynamic range of the thermometers and the temperature resolution of 10 steps. This is what is done in a staring infrared camera, but with sensing bodies, that changes their resistance due to the absorbed infrared photons. An uniformity error between the sensing bodies in the array must be corrected for, with an electronically automated calibration. Such a camera is staring in the respect that it integrates all the infrared radiation that is absorbed by the focal plane array during a typical integration time of 1/50 second. No moving parts are necessary and the detector can be slow as compared to the detector in scanning camera systems. The FPA microbolometer detector can be used at room temperatures, because it senses temperature changes, but it is often cooled by a Peltier element to reduce the noise. The camera used for sensitive absolute temperature measurements in the thesis work was based on a state-of-the-art FPA detector with the infrared absorbing resistors (microbolometers) in a 320 x 240 array. The dynamic temperature range was

–20 °C to 500 °C, the accuracy  $\pm 2\%$  of the range or  $\pm 2$  °C, and the temperature resolution was 0.1 °C.

A further thermal detector used during this work is based on the pyroelectric effect. The physical property that changes with temperature in a pyroelectric crystal is its permanent electric polarization. A capacitor is formed employing the crystal and placed in the image plane of a lens and the charge distribution on that capacitor, representing the thermal image, is read by scanning an electron beam from the back (vidicon photoconductivity technique). A camera based on this detector is also staring, and it can be used at room temperatures because it senses temperature changes. If the temperature is constant, a chopper is needed to create an alternating current from the capacitor and if the chopper is turned off, long integration times (seconds) can be chosen. The first gas-correlation images of nitrous oxide in front of a heated background were created with a pyroelectric camera in 1995, see Section 6.1, Fig. 34.

#### 4.2 Photon detectors

Due to the direct annihilation of photons and creation of an electron in a photon detector, the temperature dependence is different for the two detector families. A thermal (energy) detector has a  $T^4$  dependence while the photon detector has a  $T^3$  dependence, see Eqs. 2.3 and 2.4. Photon detectors absorb a number of photons in the active region of a semiconductor, often in the bandgap between the conduction band and the valence band. The emerging Quantum Well Infrared Photodetector (QWIP) is based on band-gap engineered low-dimensional structures, giving rise to well defined energy levels, and thereby a narrow spectral band of photon annihilation. The prevailing state-of-the-art photon detectors are based on the Mercury Cadmium Telluride (MCT) semiconductor. Recently, the MCT detectors are available in matrixes of 512 x 640 elements [63]. The photon detectors must be cooled to reduce the dark current, and by practical means this is done either by liquid nitrogen at 77 K, or with a miniature Stirling cooler yielding 65-80 K. One obvious advantage of the solitary detector is that there exists no uniformity error, which can be a severe error in the focal plane array detectors.

An often-used figure of merit in the comparison of infrared detectors is the thermal resolution, given by the noise-equivalent temperature difference (*NETD*).

$$NETD_i = \frac{\Delta T}{\Delta V_i} V_{ni} \quad (4.1)$$

The *NETD* can be measured by acquiring a number of subsequent images of a blackbody for two temperatures  $T_1$  and  $T_2$  with a temperature difference  $\Delta T$ .

$V_i(T_{i,2})$  is the average voltage and  $V_{nti}$  is the temporal noise, evaluated as the standard deviation, for each pixel,  $i$ , in the sequence.

Some of the current most capable focal plane array detectors available in infrared cameras are listed in Table 3 below. The foreseen technological possibilities suggest a *NETD* of 2 mK and a pixel resolution of 2k x 2k in some ten years from now.

Table 3. State-of-the-art infrared radiation focal plane array detectors.

	Microbolometer	MCT	QWIP
Wavelength range ( $\mu\text{m}$ )	7.5-14	3-5	8-10
NETD at 300 K (mK)	100	20	18
Pixel resolution	320 x 240	512 x 640	512 x 640
Integration time (ms)	20	2	20
Detector temperature (K)	300 K	<85 K	<62 K
Lifetime (h)	10000	>4000	>6000
Manufacturer	FLIR Systems	AIM	AIM

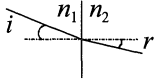
The first gas-correlation images of flowing nitrous oxide in a simulated working environment with a heated background were recorded with a scanning infrared camera, Agema THV900SW. The photon semiconductor detector, InSb (indium antimonide), was cooled to 77 K (Paper I). Visualization of simulated leaks of ammonia, ethene and methane at the Gas Test Station (GTS) in Malmö (Paper II) and at an polyethene plant (Paper III) was performed with a MCT detector in the scanning infrared camera THV900LW/Stirling.

It is in principle possible to tailor the quantum wells in a QWIP to match the absorption lines of a gas in the infrared region from 7 to 14  $\mu\text{m}$  [64-66]. The full width at half maximum of the spectral response curve can be constructed to less than 0.5  $\mu\text{m}$  [67]. This would increase the sensitivity of gas monitoring with infrared cameras as no bandpass filter would be needed.

## 5. Optical design considerations

Optics is the scientific study of light and vision. Light is generated, it propagates, it is manipulated and detected as electromagnetic radiation. One of the most fruitful early models for describing light propagation was explored by the ancient scientist Euclid (300 B.C.). In his book titled *Optics* he could with geometry describe the formation of images by spherical and parabolic mirrors. Another great achievement was performed in the year of 1621, when Snell formulated the law of refraction,

$$n_1 \sin i = n_2 \sin r, \quad (5.1)$$



where  $n_1$  is the index of refraction (speed of light in air / speed of light in medium) to the left of the surface,  $n_2$  is the index of refraction to the right of the surface,  $i$  is the angle of incidence and  $r$  is the angle of refraction. Ray tracing an optical system has been a tedious work until it was automated with computer machines in 1950. The computer has enabled us to simulate, optimize and design optical systems very fast. However, a word of caution is in place, even if a model of the optical system is well defined, a complex merit function has several local optima. An optimization process ends when the optima closest to the starting values is found. As soon as an alternative method exists to ray tracing, it should be used for reasonableness control. Therefore it is useful to divide a complex design into modules that solve specific tasks and then interface them [68]. The whole optical system performance is then determined by parts that can be optimized one at a time. This optical engineering methodology has been used to solve the design research tasks occurring during this thesis work.

The optical design in a ray-tracing program is defined by the curvature of the surfaces, the spacing and material between surfaces, the clear aperture and the coordinates of the axial and surface intercept. Other input parameters include the wavelengths of the incoming beams, the number of rays that should be traced through the surfaces and if the optical system has a special surface like a holographic surface or other features. A set of useful lens description parameters includes the effective focal length,  $EFL = y / \tan \theta$ , where  $y$  is the image height from the optical axis and  $\theta$  is the half field-of-view angle, and for conjugate systems (focal systems) the object and image distances. The tendency that several curved surfaces produce a curved image plane is the normal case (i.e. the retina) and the image curvature ( $1/\text{radius}$ ) is called the Petzval curvature of the design. In most engineered optical systems, the detector has a flat surface and the formed image should accordingly be flat.

After entering the optical components into the optical design program, a view of the lenses with the axial-, marginal and the chief ray is normally sketched. It is, however, only a sketch and the performance characteristics cannot be attributed to that sketch. If we would like to use such a sketch for presentation purposes, further aesthetic control parameters will have to be entered into the optical design program. However, real performance characteristics can now be derived through a variety of lens aberration plots.

Physical constraints (i.e. diameters and working distances) of the design can be entered as height, angle and distance parameters. The solving function fixes the constraint by varying the free parameters. When a paraxial ray trace has been performed, the result can be evaluated as ray intercept plots for the axis, half field, 0.7 field and full field. The field curvature, the astigmatism, i.e. the tangential (horizontal) field curve and the sagittal (vertical) field curve differ and the distortion, i.e. image shape, can also be evaluated. After a successful ray tracing, all the traced rays can be used to minimize the rms spot size on-axis by automatically varying the image plane and search for the smallest ray bundle. This procedure will result in a new focal length, which differs from the paraxial focal length. Ray tracing cannot tell if the optical system is diffraction limited but this is verified at this point with algorithms that are specific for diffraction theory. Only the most expensive and computer-power demanding ray-tracing programs can handle real diffraction theory, based on vectors. The technique used to circumvent this problem is called extended scalar diffraction theory [55]. The following subsections will present the specific optical designs that were developed to solve the encountered research problems during this work.

### *5.1 Gas-correlation telescopes*

In order to create a gas-correlation image we needed a telescope with two openings forming two adjacent images, which are captured at the same time and side-by-side by an infrared sensitive camera. The original telescope used in part of this work (Paper I-II) was based on the well-known Cassegrainian design, modified with a primary mirror split in four sections that could be positioned individually [69,70]. A ray trace of the gas-filter cell path of the telescope is shown in Fig. 26.

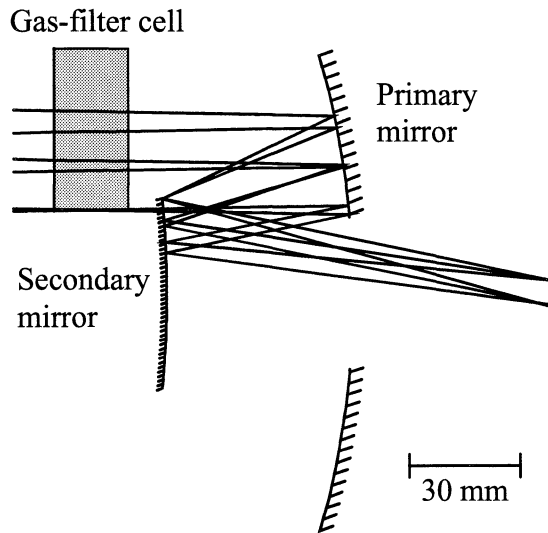


Fig. 26. Ray trace of the gas-filter cell path of the split-mirror Cassegrainian telescope.

Both the primary mirror and the secondary mirror were coated with aluminum and a protective silicone dioxide layer. The telescope was developed for visible fluorescence imaging prior to the infrared gas-correlation application. Several problems were encountered with this telescope design. The main problem was that the camera detector always sees itself (i.e. optical feedback) or the surrounding housing in the normal of the spherical secondary mirror. The two adjacent images must match each other exactly and this means that the stability of the focusing adjustment and the positioning of the split mirrors in the telescope are crucial. In order to minimize the parallax distortion in the final image the openings of the telescope should be as close to each other as possible. A severe crosstalk between the images and reflection from the walls inside the aluminum housing were identified as major problems. The split-mirror Cassegrainian design was based on spherical mirrors with the central part of the primary mirror removed and this results in poor image quality due to spherical aberration but also due to obstruction of the incoming rays by the secondary mirror. The spherical aberration is thus by definition severe for the split-mirror Cassegrainian design. The telescope was simulated and analyzed with the optics design program to gain more information and insights on how a new telescope should be constructed. Two fundamental performance indicators derived by ray tracing the Cassegrainian telescope and the physical specifications of the telescope are summarized in Table 4.

Table 4. The Cassegrainian telescope specifications and figures of merit.

<b>Cassegrainian Telescope</b>	<b>Primary mirror</b>	<b>Secondary mirror</b>
Radius (mm)	-220.84	+281.4
Diameter (mm)	125	50
Effective focal length (mm)	194	
Opening diameter, D (mm)	2 x 43	
f-number (Efl/D)	2.3	
Operational range (m)	10-100	
Dimensions (mm)	Diameter: 200, Length: 260	
Weight (kg)	7	
<b>Performance indicators</b>		
Spot size radius on axis ( $\mu\text{m}$ )	100	
Petzval radius (mm)	513	

The Petzval radius is calculated from the surface curvatures and it is the radius of the image curvature that would be formed by an extended plane object. Thus, an infinite Petzval radius represents the stigmatic (perfect) image of the object plane. The spot size represents the ray deviations from the stigmatic imaging case. This figure of merit should accordingly be as small as possible. The physical limit to geometrical ray tracing is the diffraction limit calculated as

$$r = \frac{1.22 \cdot \lambda}{D} \cdot b, \quad (5.2)$$

where  $r$  is the spot size radius,  $\lambda$  is the wavelength,  $D$  is the aperture and  $b$  is the image distance. The ray-tracing program calculates both the geometrical spot size and the diffraction limited spot size.

The optimum simulated solution to the problems of the Cassegrainian telescope was based on two off-axis parabolic mirrors and a folded mirror design with stable remote control of the focusing in a lightweight and compact aluminum housing. A ray-tracing plot of the gas-filter cell path of the telescope is shown in Fig. 27.

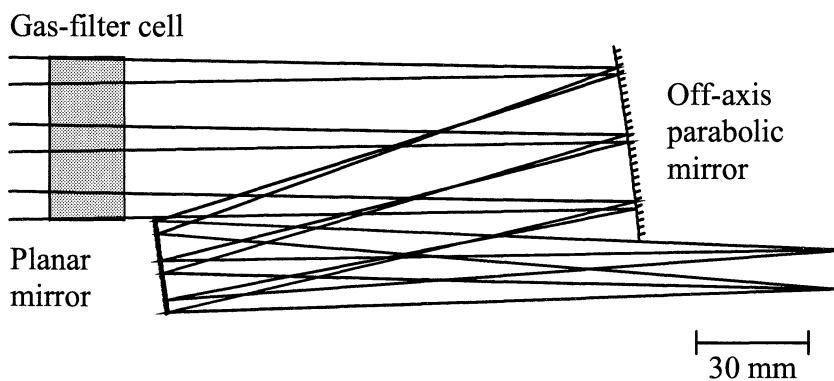


Fig. 27. Ray trace of the gas-filter cell path of the new telescope.

The walls, inside the telescope, have been covered with a high-emissivity paint to reduce reflections and uneven infrared emission from the telescope. We have evaluated the new design both by comparing the simulations and by comparing the real images formed by the two designs. Performance indicators and the physical specifications of the new diffraction limited telescope are summarized in Table 5.

Table 5. The Gas-Correlation Telescope specifications and figures of merit.

<b>Gas-Correlation Telescope</b>	<b>Off-axis parabolic mirror</b>	<b>Planar mirror</b>
Focal length, Efl (mm)	305	-
Diameter (mm)	2 x 50.8	2 x 25.4
Opening diameter, D (mm)	2 x 43	
f-number (Efl/D)	3.5	
Operational range (m)	10-1000	
Dimensions (mm)	Width: 145, Height: 105, Length: 260	
Weight (kg)	3	
<b>Performance indicators</b>		
Spot size radius on axis ( $\mu\text{m}$ )	22	
Petzval radius (mm)	305	

The f-number of the infrared camera has a value of 3.2, and to become interfaced, the telescope f-number must not be below this value as this would result in crosstalk between the images. Stray light analysis was performed with real images from the telescopes and the result is presented in Fig. 28. The images in Fig. 28(a) and (b) show an incandescent lamp placed in a desk lamp directed towards the telescopes 10 meters away. The resolution is seen to be lower in the image created by the Cassegrainian telescope, mainly due to the spherical aberration.

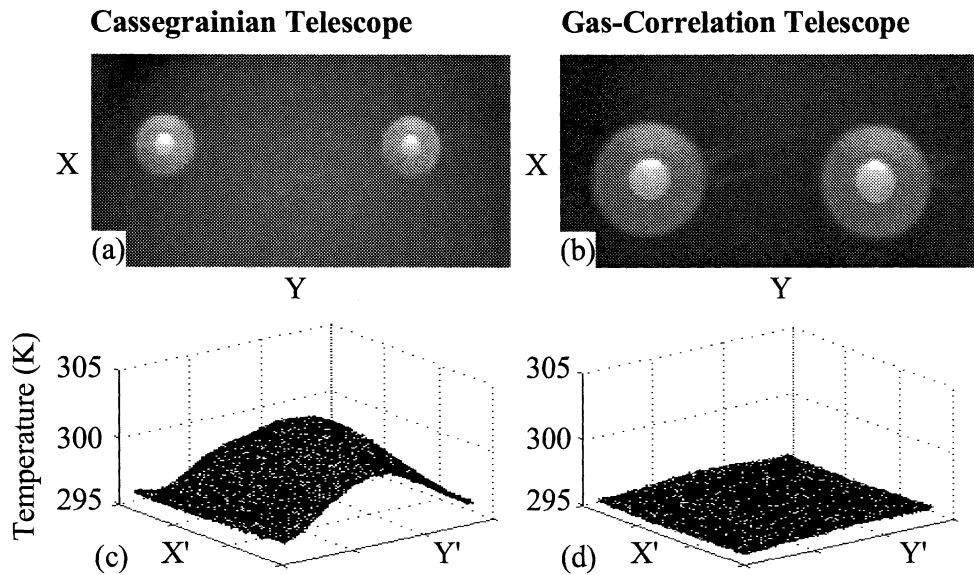


Fig. 28. Infrared split-mirror image of a desk lamp formed by the Cassegrainian telescope (a). Corresponding image formed by the new telescope (b). Cassegrainian telescope background image without lamps (c). Flat background formed by the new telescope without lamps (d).

The optical feedback from the secondary mirror in the Cassegrainian telescope was the cause of the curvature seen in Fig. 28(c). The image was taken by directing the telescope at a diffuse surface close to the telescope and out of focus. The solution to this problem is the planar angled mirrors in the gas-correlation telescope.

### 5.2 Gas-filter cell design

Two important aspects on the gas-filter cell are the thickness of the cell controlling the gas absorbance and the spectral transmittance of the window material and its anti-reflection coating. The gas absorbance can be tuned, by changing the partial pressure, so that fully saturated absorption lines are present in the spectrum. The window material and anti-reflection coating depends on the position of the gas absorbance band. The materials we have been using are Ge, ZnSe, KCl and  $\text{CaF}_2$ . The dimensions of the gas-filter cells are 50 mm diameter, 20 mm inner thickness, with two tubes with valves connected to the cylindrical walls. The tubes are used to fill or flow the cell with gas and they have been used to study the effect of fine-tuning the integrated line strength of the gas absorbance by changing the partial pressure of the gas with a flow meter. It is practical to work with the gas at atmospheric pressures as the visualized external gas is always at the atmospheric pressure if it is leaking to the atmosphere.

### 5.3 Aerosol particle sensor optics criteria

In this application, the extinction signal and the diffraction image from one single aerosol particle passing the sensing volume of the instrument should be recorded at the same time. We want to determine both an optical equivalent size and the shape of the particle. The optics that were chosen to the first prototype were simulated with the optics design program in order to optimize light gathering power, mechanical dimensions and the use of off-the-shelf optics. The optical components that were finally chosen for the prototype included a commercial diode laser, lasing at 780 nm and collimated with a diffraction limited lens [71-73]. The laser beam was directed back by a low-reflectance mirror, that was mounted in a home-built piezo-electrically controlled mount. A schematic picture of the aerosol particle sensor is shown in Fig. 29 and a picture of the setup is shown in Fig. 30.

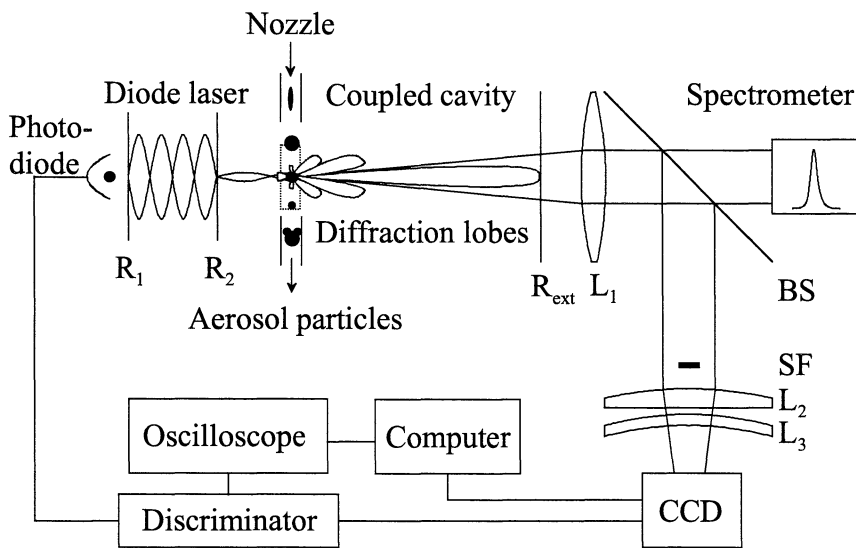


Fig. 29. Aerosol particle sensor schematic setup. The diode laser coupled cavity is created with the weak reflector  $R_{ext}$ . A spatial filter SF is used to block the direct laser light. The beamsplitter, BS is used for folding the scattered light to the CCD and part of the laser beam is directed via a fiber to a spectrometer for control of the coupled cavity. Near-forward scattered light from the particles is gathered by the Fourier lens  $L_1$  and a reduction is performed by the lenses  $L_2$  and  $L_3$ . The extinction signal sensed by the photo diode, inside the diode laser capsule, is used to trigger the capture of a diffraction image.

The weak reflector,  $R_{ext}$ , is the external mirror of the coupled cavity [74] and at the same time it should transmit near-forward scattered light. The experimentally chosen reflection of the mirror was 8%, which is in accordance with the theoretical models we have compared with [75-81]. By using such a weak reflector the

threshold current of the coupled cavity was reduced with 7%. Optical feedback into a diode laser can easily result in chaotic behavior, increased noise, intensity above the damage threshold and fringes. However, the operating characteristic of a diode laser with an external cavity has been described in [82], and one regime is free from unstable behavior (i.e. coherence collapse) when using a weak reflector. This regime is just below the injection current threshold of the free running diode laser and above the injection current of the coupled cavity laser. This regime must be used, as we want to collect near-forward scattered light from the particles inside the coupled cavity. We are using the forward- and backscattered radiation from the aerosol particles to trigger the infrared sensitive CCD camera (with an optimum sensitivity at 780 nm), which captures an image of the Fourier plane. The spatial frequencies in the Fourier plane from a particle inside the measurement volume, which is comprised of the laser beam cross section and the focal plane of the Fourier lens, are thus largely independent of the lateral particle position in the measurement volume. A particle passing the instrument yields the same minimum positions in the diffraction pattern all the way through the laser beam. A discriminator circuit is connected to the photodiode inside the diode laser capsule and it can be used to decide which particle size range we want to sample. For characterization and alignment purposes some of the laser light that is spatially filtered out of the near-forward scattered light was sent to a spectrometer.

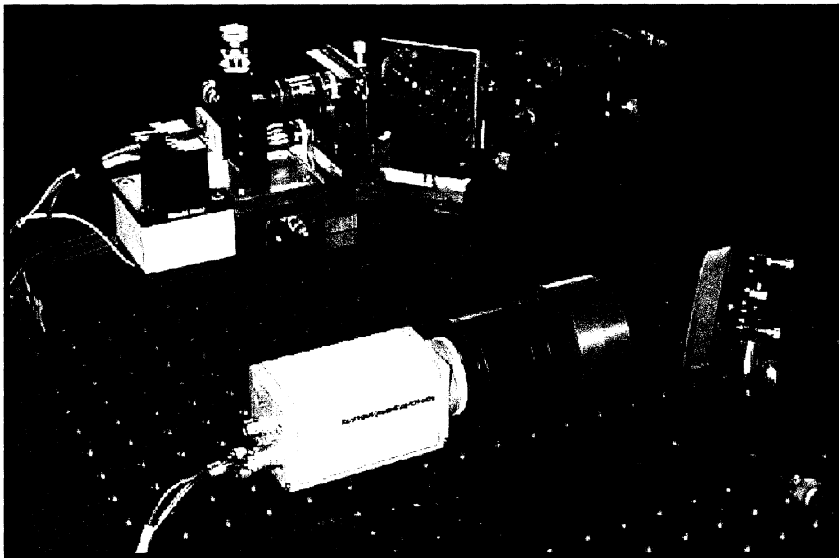


Fig. 30. Picture of the aerosol particle sensor with its coupled cavity top left and the CCD camera bottom left.

Just outside the coupled cavity design, the Fourier lens is placed to collect and transform the near-forward scattered light. A ray trace of the optical design that collects the scattered light after the coupled cavity is shown in Fig. 31.

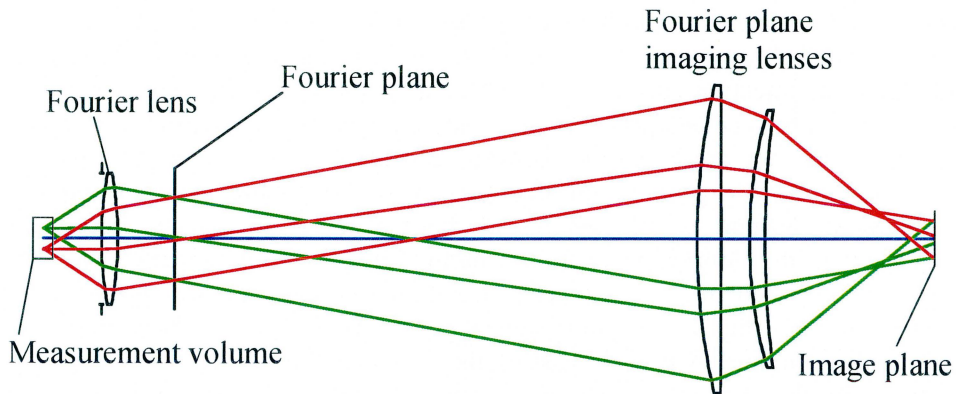


Fig. 31. Near-forward scattered light, ray traced through the Fourier lens and imaged on the CCD image plane. Notice that collimated laser light (not depicted) entering the measurement volume is focused in the Fourier plane, where it is spatially filtered out of the near-forward scattered light.

The Fourier plane imaging lenses create an image which fill the CCD focal plane array (size: 8.8 mm x 6.6 mm, 754 x 484 pixels). The angles of diffraction are increasing with a decreasing fiber diameter as tabulated in Section 3.4, Table 1. In order to collect the first diffraction minimum with the Fourier lens a particle with a size of at least 2  $\mu\text{m}$  is required. The upper particle size limit, 150  $\mu\text{m}$ , is set by the resolution of the CCD focal plane array.

A coupled cavity is a delicate instrument which is subject to disturbances such as vibrations and thermal expansion of the optical mounts. The length of the coupled cavity is in this case determined by the space needed for accessing the measurement volume and the length of the resonator. A short resonator improves the stability and it also makes the whole instrument more compact which should be favorable in many applications. The whole instrument should be built on a monolithic aluminum plate which is kept at a constant temperature with Peltier effect components. We have also explored the possibility of using an active stabilization control of the coupled cavity, which is based on an algorithm for radar tracking (Melles Griot, NanoTrak). This instrument is connected to the photodiode inside the diode laser capsule, and by maximizing the intensity of the single-mode coupled cavity by automatically adjusting the input coupling of the laser beam with the mirror mount, the coupled cavity can be made stable. However, the radar tracking instrument has a bandwidth of 5 Hz and the aerosol particle instrument is therefore still sensitive to sudden vibrations. Such problems can be addressed by

mounting the instrument in a vibration isolated environment, i.e., using shock absorbers.

### *5.3 Difference-frequency generation criteria*

One of the major issues in the development of a diode-laser based spectrometer for simultaneous measurements of methane (at 3.4  $\mu\text{m}$ ), oxygen (at 760 nm) and water vapor (at 980 nm) was to achieve appropriate signals at all three wavelengths. Several parameters must be optimized in order to achieve high conversion efficiency in the difference-frequency generation. This is especially important when using low-power diode lasers as difference-frequency generating sources. As mentioned in Section 2.4 the energy conservation condition determines the wavelength of the generated beam. The phase relationship must be maintained by the periodically poled crystal. The general conversion efficiency expressions are given in Paper IV and a comprehensive study was performed by [83]. Here we will focus on the optical considerations, such as input coupling lens selection and beam overlap. For this purpose ray tracing was performed to study beam overlap and focusing of the two generating beams inside the PPLN crystal.

Now, the non-linear interaction between the two beams (plane waves) in the crystal is a phenomenon normally described by Maxwell's equations and the polarisation. Here, the simplified model of ray tracing has been utilized. This is possible as we are mainly interested in optimizing the beam overlap. The Poynting vector  $\mathbf{S} = \mathbf{E} \times \mathbf{H}$ , where  $\mathbf{E}$  is the plane wave electric field and  $\mathbf{H}$  is the magnetic field, represents the amount and direction of instantaneous energy flow, which is in the direction of propagation of a plane wave. For each ray that is traced, there is an associated electromagnetic field that is planar in a small region around the ray. A spot diagram of rays from both of the generating wavelengths should accordingly show as much overlapping rays as possible.

Ray tracing has been performed for two different coupling lenses. The performance of a plano-convex lens, frequently used in laser applications, was compared with that of a diode laser doublet lens used in Paper IV. Before the focussing, we have used two anamorphic pairs of prisms to transform the elliptically shaped beams of the collimated diode lasers to circularly formed. A channel in the PPLN crystal has an entrance opening of 0.5 mm x 1 mm, as shown in Fig. 32 as a rectangular box around the incoming ray bundles.

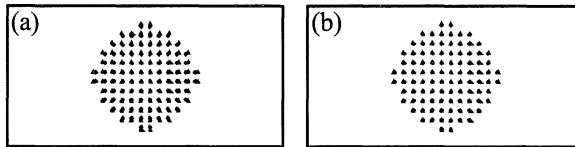


Fig. 32. The overlap of rays at the entrance opening of one PPLN channel from the two laser sources after being refracted by a plano-convex lens is seen in (a). The corresponding overlap after refraction by a diode laser doublet lens is seen in (b).

The ray bundles at the entrance opening of the PPLN crystal was also ray traced inside the channel through focus. In Fig. 33 the diode laser doublet lens is seen to produce improved beam overlap as compared to the plano-convex lens.

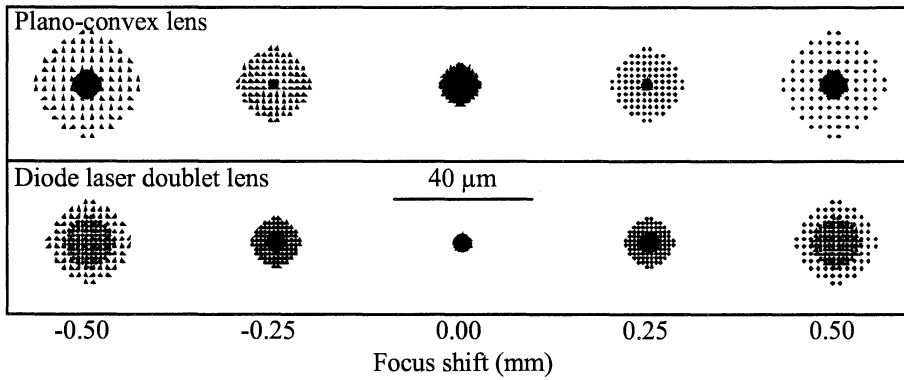


Fig. 33. Spot diagram of a ray trace through the focus inside the PPLN crystal.

The high performance of the diode laser doublet lens in this case, is mainly ascribed to spherical aberration correction and that the design wavelength is 830 nm, which is between the wavelengths of our diode lasers at 760 nm and 980 nm. The design wavelength of the plano-convex lens tested is 546 nm.

## 6. Image processing

### 6.1 Gas visualization

As mentioned in Section 2.1 the contrast in visible light photography is governed by the reflectance and the transmittance of the objects. In infrared thermography the contrast of an image is depending on surface temperatures and varying emissivity. By combining a visible image with an infrared image, more information is frequently obtained. Very often science can be inspired by solutions to problems in nature. The pit snake has a remarkable type of vision which is well suited for hunting mice against the cold desert sand at night. Infrared sensing is accomplished by detecting heat with small indentations around the mouth and eyes. The information from these “pits” and information from the normal eyes are sent to a region in the brain where image processing is performed. With the resulting superimposed image the snake is able to locate the mice even during the darkest of nights.

In this work the mice is exchanged with gas, the pit snake with the two-dimensional gas-correlation principle whereas the reptile brain image processing is performed mainly with Matlab on a PC.

The first gas-correlation image is shown in Fig. 34(c) and it will be used as a simple example of image processing [84,85] needed to obtain gas absorbance images. The image was created employing an infrared pyroelectric camera with a bandpass filter that cuts-out the spectral band of  $N_2O$  and an infrared heater was used as background radiation. One image was taken of the empty gas cell, see Fig. 34(b). Another image was later taken with  $N_2O$  gas in the cell, Fig. 34(a). The resulting image after computing the ratio between all pairs of corresponding pixels from (a) and (b) is shown in Fig. 34(c). Offset correction must be performed before the division if one wants to calibrate the gray scale with gas absorbance. The most pronounced noise in the image is the so called *salt-and-pepper* noise. It consists of random pixels being set to the extremes of the data range. The best method to reduce this noise is median filtering. A median filter consists of a small matrix, for example 3 x 3 pixels large, which is translated over the whole image and for every step a new central pixel is calculated by weighting with the pixels around. The main conclusion from the resulting image is that the cell walls and the varying radiance from the background is cancelled out and the remaining information is gas absorbance. An alternative to dividing the images would be to subtract (b) from (a). The final image noise consists in this case of the added noise terms from the two images (a) and (b). Subtraction can be used in gas visualization when quantification is not needed, e.g. in leak searching applications.

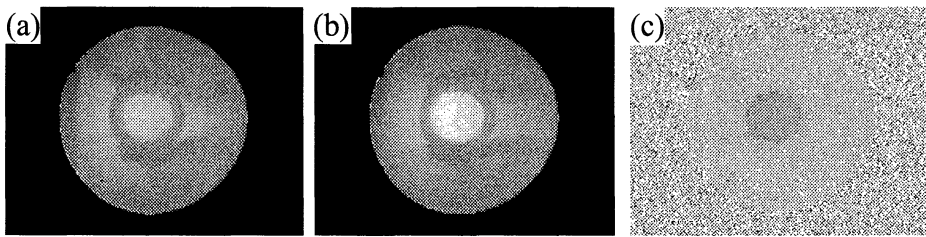


Fig. 34. The first gas-correlation image was captured with a camera employing a pyroelectric detector (c). The background was an infrared heater. (a) Dividend; Gas cell filled with  $N_2O$  seen in absorption (spectral band position:  $4.5 \mu m$ ). (b) Divisor; Empty gas cell. Notice that the *salt-and-pepper* noise in the result image, (c), increase outside the circular image area. This is due to electronic noise in the camera read-out circuits. In (c) the noise is seen to decrease towards the middle.

Raw data image format and gray- or color-scale use are other important aspects of image processing. The radiometric signal from the camera is stored as pixel values and it is favorable if the dynamic range is large (i.e. at least 12 bits) when dividing images. Compression algorithms (e.g. jpeg and gif) cannot be used as they are destroying the linear gas absorbance scale. Fast concatenated hard discs were used in order to record the raw data images in real-time. The data transfer rate of the longwave MCT camera was 9 Mbits/s, originating from images with a size of  $272 \times 136$ , 12 bits in intensity depth at a rate of 15 images per second. A linear gray scale is best suited for gas absorbance presentations but a color scale can also be added to a visible image to reflect the path-integrated absorbance if the background of the visible image is essentially free from the chosen color or if the gas absorbance replaces the pixels in the visible image. The latter method is, however, far more computer demanding. As an example of the former method, a gas absorbance image created in emission with the sky as background can be color coded in red simply by adding the gas absorbance values to the red matrix in an RGB image.

In Paper II a controlled leak of ammonia was set up in front of a gas tanker which was heated by the sun. Background images, without external gas, including the tanker, the gas-filter cell self emission and the imaging errors of the Cassegrainian telescope was captured and an average image of 4 seconds (60 images) was first calculated. A direct image, Fig. 35A, of the flowing gas was captured at the same time as an ammonia gas-filtered image, Fig. 35B. An offset value, derived by calibrating the system, see Section 3.3, was subtracted from the background image. An normalization image was derived by dividing the direct background image with the gas-filtered background image without any external gas as to handle the imperfections from the Cassegrainian telescope and the self emission from the gas-filter cell. Gas correlation was then performed by dividing the direct image with

flowing external gas with the ammonia gas-filtered image and the normalization image, the result is shown in Fig. 35C.

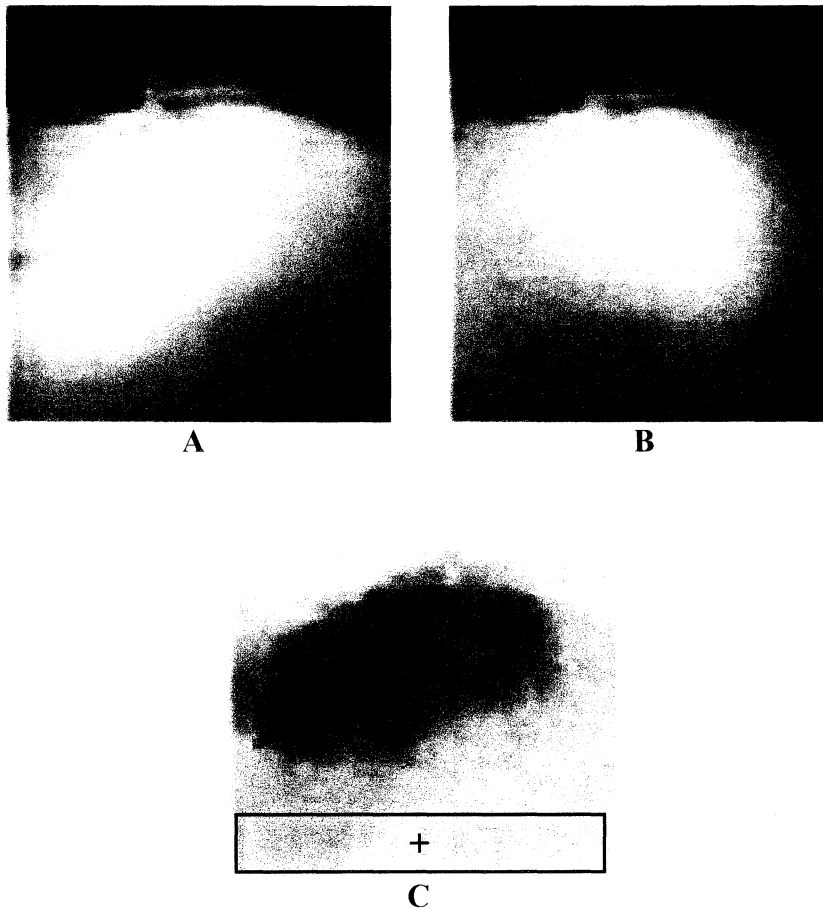


Fig. 35. Gas-correlation image processing. (A) is the direct image, notice the gas absorption in front of the tanker. (B) is the ammonia gas-filtered image and (C) is the gas-correlated image. The box down in image (C) defines the surface where the spatial noise is calculated. The plus sign shows the pixel position where the temporal noise through a sequence of images is evaluated.

The resulting gas absorbance image, Fig. 35C, was median filtered and the simulated gas absorbance values, see Section 3.3, were used as threshold values for path-integrated concentration. The gas image was finally merged with a visible image of the tanker, as shown in Fig. 36.

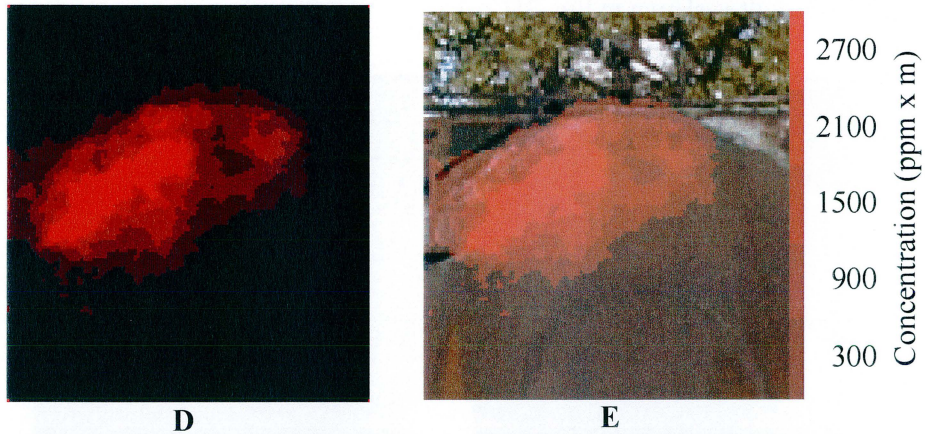


Fig. 36. The simulated gas absorbance values were used as thresholds to create the concentration color-coded image (D). A visible image was merged with the gas image (E).

### 6.2 Noise in gas-correlated images

Taking the mean of an ordinary image, including objects, gives a measure of the brightness of that image. The contrast in such an image can be measured by calculating the variance of the image. The temporal noise in a gas-correlated image sequence can be estimated by calculating the standard deviation in a pixel position, marked as a plus sign in Fig. 35C, which is free from gas, in several consecutive images in time. This was done for the calibrated ammonia sequence (50 images) in order to estimate the detection limit. The temporal noise result is as follows:

Standard deviation: 0.0019  
 Detection limit: 60 ppm x m

However, temporal noise calculation is not enough as the spatial noise was observed to be the limiting factor. In a sequence of images we cannot allow one single image to show ammonia if it is noise. The box in Fig. 35C, shows the area where the standard deviation of a gas free part of the image is calculated. A vector containing all the standard deviations are created and the maximum value in that vector is then used as the spatial noise. The spatial noise result is as follows:

Standard deviation: 0.0057  
 Detection limit: 165 ppm x m

A threshold of 300 ppm x m was used in the ammonia concentration sequence in Paper II. With the new gas-correlation telescope a detection limit of 30 ppm x m has been predicted. The same calculations must be performed for all the other gases that are tabulated as possible candidates for future gas-correlation imaging in Chapter 7, Table 7. The result is mainly depending on the sensitivity of the camera, the spectral filter, the band integrated absorbance of the gas and the temperature difference between the background and the gas. If the temporal resolution can be allowed to decrease, then the detection limit can be estimated by dividing the limit with the square root of the number of averaged images.

### *6.3 Gas flow evaluation by cross correlation in time*

After gas-correlation processing the resulting gas absorbance images are free from background and other interfering gases. An auto correlation of a gas image at time  $T_0$  can be cross correlated with a gas image at a later time  $T_1$ , yielding a vector for the whole moving gas structure [86,87]. The speed can then be multiplied with an area integrated gas concentration and this in turn yields the gas flow. By reducing the size of the spatial correlation matrix a map of vectors can be derived and a gas flow map can be created. These procedures were used in Paper III.

## 7. Applications

### 7.1 Gas visualization

An illustrative picture of the virtue of the method developed is shown in Fig. 37. Here the spectrally interfering gases ammonia and ethene are absorbing infrared background radiation from a burnt out gas tanker at the Gas Test Station in Malmö, as seen in the upper left inserted direct image. The gases are separated with the gas-correlation method using an ammonia gas-filter cell. The upper right insert image shows ammonia only, color-coded in red. The depicted situation is an example of a leak search application. In an industrial site there is often interfering water vapor around, but the monitored gas can be distinguished by the use of gas-correlation imaging.



Fig. 37. A burnt out gas tanker with spectrally interfering ammonia and ethene gas leaks. The ammonia gas is gas-correlated and seen in the upper right image.

The number of areas where gas visualization is important is large. A highly interesting application is the monitoring of flares that are used to burn excess hydrocarbon gases. The flare at a polyethylene plant should for example be optimized for the combustion of excess ethene coming from the production. Flares

are typically placed at a location and with a height that does not disturb the activities at the petrochemical industry and is environmentally satisfactory. The flare is therefore hard to access and it is difficult to monitor the combustion with existing point monitoring methods. The gas-correlation method has been used to visualize ethene escaping from a flare with incomplete or erratic combustion. The measurement equipment was placed at a distance of 400 m from the flare. The excess ethene gas is visualized and coded red in Fig. 38, and a sequence of such gas images can be used to optimize the flare combustion.

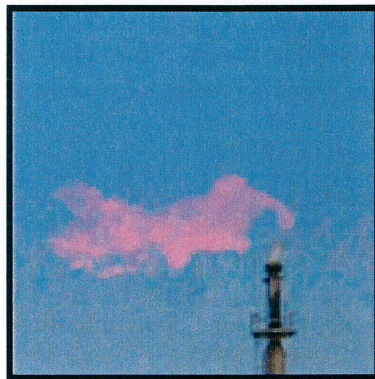


Fig. 38. Ethene escaping from a flare visualized with the gas-correlation system.

A measurement of the total flux of a gas from an industrial site is an interesting application for the environmental protection agencies.

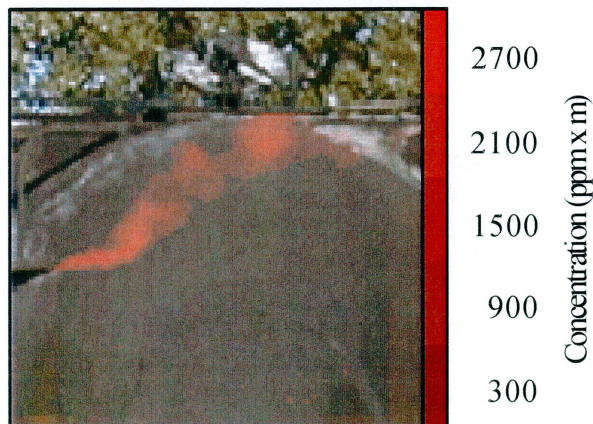


Fig. 39. Ammonia concentration image. Such an image in combination with wind vectors derived by cross-correlating gas images in time can be used for flux determinations.

The flux of ammonia in the concentration image shown in Fig. 39, is calculated by multiplying the area-integrated concentration with a wind vector, which is derived by the image processing method described in Section 6.3.

Inspections of leaks from refineries or tank farms has environmental, security and economical aspects. Inspection of gas pipelines is another possible application. Work has been done on methane at the Gas Test Station and the resulting images clearly shows that practical methane leakage detection is feasible. Landfill areas sometimes have high and localized evaporation of methane; an application that has to be investigated further. Emissions of geophysical origin (volcanoes, geothermal installations or mines) as well as natural emissions of greenhouse gases from agriculture, swamps, etc., are also interesting to assess.

Easily deployable surveillance techniques for assessing sites of accidents involving gas tankers or trains are desirable for public safety considerations. Accidents with leaking gases can evolve to become an even greater disaster. Accurate point monitoring of the site, involving all the valves and hoses, takes time and is extremely dangerous. The remote gas-correlation imaging method makes it possible to get an overview of the accident and direct the efforts to specific problem areas.

A leaking anaesthetic gas, like nitrous oxide, could possibly be monitored during an operating theatre so that the mask can be placed over the face in an appropriate way. We have imaged nitrous oxide at 4.5  $\mu\text{m}$  in a laboratory set-up with added thermal background radiation from an infrared heater in the short-wave region. The results are promising but it is too early to finally conclude if this is a possible application. Another working environment application could be the visualization of evaporating solvents. The possibility of imaging styrene evaporating from the production of the hull of a ship can be investigated further.

A special virtue of the passive gas-correlation technique is the possibility to adapt the system to a large variety of measurement platforms. The system can in principle be operated from essentially any vehicle, ranging from cars to small unmanned helicopters or satellites.

Some gases already imaged or potentially measurable, are summarized in Table 6 together with suitable interference filters when the Agema THV900 SW and LW infrared cameras are employed.

Table 6. Gases examined in the laboratory, at the Malmö Gas Test Station (GTS) and at the industrial sites. The gases listed as “to be explored” are well suited for gas-correlation imaging. The interference filters are described as long-wave pass (LP), short-wave pass (SP) and broad-band pass (BBP) filters with a wavelength position of for example 7.4  $\mu\text{m}$  if the figures are 7400.

Name	Filter Spectrogon	Alternative filter	Examined
Methane	LP7400	BBP7040-8500	Laboratory experiments, Malmö GTS
Ethene	LP9200		Laboratory experiments, Malmö GTS, Borealis AB, Polyethene and Cracker plants
Styrene	LP9200		To be explored
Ammonia	LP9200	LP8650, BBP9090-12255	Laboratory experiments, Malmö GTS, Path-integrated concentration calibrated
Carbon monoxide	SP5100	SP4900	To be explored
Nitric oxide	SP5600	BBP5150-5550	To be explored
Nitrous oxide	BP4560-260		Laboratory experiments with an infrared camera sensitive in 3-5 $\mu\text{m}$
Formaldehyde	BBP5425-6220	BBP5350-6255	To be explored
Vinyl chloride	LP10100		To be explored

In Table 7 all the gases that are identified, through their spectrum, as possible candidates for gas-correlation imaging are listed. Further investigations would be feasible to perform on selected gases in Table 7 and field studies could be performed in their specific application environments.

Table 7. Gases relevant for visualization and suitable for gas-correlation imaging. The letter P in the spectrum column denotes a spectrum with separated lines and the letter B denotes a broad spectrum. The positions are given as a coarse guidance to where the spectrum is located.

Name, Formula	Position		Spectrum		Notes
	cm <sup>-1</sup>	μm	P	B	
Methane, CH <sub>4</sub>	1300	7.7	x		Natural gas, H <sub>2</sub> O interference
Ethene, C <sub>2</sub> H <sub>4</sub>	1000	10	x		Large use, vinyl monomer
Propylene, C <sub>3</sub> H <sub>6</sub>	900	11	x	x	Raw material for detergents
Isoprene, C <sub>5</sub> H <sub>8</sub>	900	11	x	x	Obtained in processing petroleum
Styrene, C <sub>8</sub> H <sub>8</sub>	900	11	x	x	Plastic raw material
Toluene, C <sub>6</sub> H <sub>5</sub> CH <sub>3</sub>	1100	9.1		x	Antiknock additive in aviation gasoline
Ammonia, NH <sub>3</sub>	1000	10	x		One of the most used chemicals
Hydrazine, N <sub>2</sub> H <sub>4</sub>	1000	10	x	x	Reducing agent
Carbon monoxide, CO	2200	4.5	x		Exhaust gas, incomplete combustion
Ethylene oxide, C <sub>2</sub> H <sub>4</sub> O	800	12		x	Detergent raw material, toxic, explosive
Hydrogen peroxide, H <sub>2</sub> O <sub>2</sub>	1250	8.0	x	x	Bleaching agent e.g. for cotton
Ozone, O <sub>3</sub>	1000	10		x	Produced by electric discharge, toxic
Propylene oxide, C <sub>3</sub> H <sub>6</sub> O	1000	10		x	Used for antiknock gasoline additives
Tetrahydrofuran, C <sub>4</sub> H <sub>8</sub> O	1100	9.1		x	Used in nylon production
Acetic acid, CH <sub>3</sub> COOH	1200	8.3		x	Vinegar
Acrylic acid, C <sub>3</sub> H <sub>4</sub> O <sub>2</sub>	1000	10		x	Production of polymers e.g. acrylates
Formic acid, CH <sub>2</sub> O <sub>2</sub>	1100	9.1		x	Processing textiles and leather
Acetaldehyde, CH <sub>3</sub> CHO	1200	8.3		x	Start chemical for acetic acid
Acrolein, C <sub>3</sub> H <sub>4</sub> O	1000	10		x	Used in organic synthesis
Benzaldehyde, C <sub>6</sub> H <sub>5</sub> CHO	1200	8.3		x	Perfume industry
Acetone, (CH <sub>3</sub> ) <sub>2</sub> CO	1200	8.3		x	Solvent and used in organic synthesis
Allyl alcohol, C <sub>3</sub> H <sub>5</sub> OH	1000	10		x	Flavoring agents
n-Butyl alcohol, C <sub>4</sub> H <sub>9</sub> OH	1100	9.1		x	Solvent
m-Cresol, C <sub>7</sub> H <sub>8</sub> O	1200	8.3		x	Disinfectant, many bands
Ethanol, C <sub>2</sub> H <sub>5</sub> OH	1050	9.5		x	Solvent
Isobutanol, C <sub>4</sub> H <sub>9</sub> OH	1100	9.1		x	Many bands
Isopropanol, C <sub>3</sub> H <sub>7</sub> OH	1100	9.1		x	Solvent
Methanol, CH <sub>3</sub> OH	1000	10	x	x	Solvent and fuel
Phenol, C <sub>6</sub> H <sub>5</sub> OH	1200	8.3		x	Highly toxic
n-Butyl acetate, C <sub>6</sub> H <sub>12</sub> O <sub>2</sub>	1250	8.0		x	Ester
Ethyl acetate, C <sub>4</sub> H <sub>8</sub> O <sub>2</sub>	1200	8.3		x	Solvent for resins, paints and lacquer
Methyl acetate, C <sub>3</sub> H <sub>6</sub> O <sub>2</sub>	1250	8.0		x	Ester
Vinyl acetate, C <sub>4</sub> H <sub>6</sub> O <sub>2</sub>	1250	8.0		x	Polymerize to resins used as coatings and adhesives
Chloromethyl methyl ether, C <sub>2</sub> H <sub>5</sub> ClO	1200	8.3		x	Strong bands; highly volatile liquid
Diethyl ether, C <sub>4</sub> H <sub>10</sub> O	1150	8.7		x	Solvent and anesthetic
Nitric acid, HNO <sub>3</sub>	1300, 800	7.7, 12		x	Used for fertilizers, explosives and dyes

Nitric oxide, NO	1800	5.6	x		Combustion
Nitrogen dioxide, NO <sub>2</sub>	1600	6.2		x	Combustion
Nitrous oxide, N <sub>2</sub> O	2250, 1300	4.4, 7.7	x		Anesthetic gas
Acrylonitrile, C <sub>3</sub> H <sub>3</sub> N	1000	10	x	x	Volatile flammable liquid, used in polymer manufacturing
Methyl isocyanate, CH <sub>3</sub> NCO	2250	4.4	x		Extremely toxic, used in pesticide production
Iodomethane, CH <sub>3</sub> I	1200, 900	8.3, 11	x		Produced by ocean-living organisms
Tributyl phosphate, (C <sub>4</sub> H <sub>9</sub> ) <sub>3</sub> PO <sub>4</sub>	1000	10		x	Antifoaming agent, hydraulic fluid, solvent
Vinyl chloride, C <sub>2</sub> H <sub>3</sub> Cl	1600, 900	6.3, 11	x	x	Flammable gaseous carcinogenic compound, used to make vinyl resins

### 7.2 Aerosol particle sensor

Pollen grain identification and number density determination is an application of great interest for people suffering from allergy. The instrument has been built with on-the-shelf optics and an inexpensive mirror-positioning mount in order to make it available at low cost.

Presently, the instrument is extremely sensitive to disturbances such as variations in the airflow inside the measurement volume but also to vibrations from the environment. This could be taken care of in the next prototype by reducing the length of the coupled cavity and by building all the optical components on a common thermally stabilized platform.

### 7.3 Diode laser spectrometer

The prevailing natural outdoor concentration of methane is 1.7 ppm. The spectrometer is capable of monitoring ambient methane concentrations at the C-H bond-stretching vibrational bands of hydrocarbons. The spectrometer can provide absolute calibration of passive gas correlation imaging measurements for hydrocarbons [Paper I-III]. In low-pressure recordings of methane gas the low abundance isotope <sup>13</sup>CH<sub>4</sub> could be monitored. The isotopic ratio of <sup>13</sup>CH<sub>4</sub>/<sup>12</sup>CH<sub>4</sub> can be used in geo- and biochemical applications for characterization of methane sources [88].

## 8. Summary of papers

**Papers I-III** describe a new method for specific visualization of freely flowing gases utilizing an infrared camera and a gas-correlation telescope. In *Paper I*, experiments were performed on flows of methane, nitrous oxide and carbon dioxide at a workplace test setup. An infrared camera sensitive in the spectral region from 3-5  $\mu\text{m}$  was used in combination with interference filters and a split-mirror Cassegrainian telescope. Gas-correlated images in sequence showed nitrous oxide in a mixture of carbon dioxide and water vapor in front of a heated background. In *Paper II*, the camera was exchanged with a long-wavelength sensitive camera, 7-14  $\mu\text{m}$ , enabling passive remote visualization of controlled leaks of ammonia, ethene and methane in front of a gas tanker. An ammonia gas calibration procedure was developed employing a spectral line position database and convolution with Lorentzian line profiles. In *Paper III*, we used the gas visualization system with a newly developed gas-correlation telescope to find an unknown leakage of ethene at a polyethene plant. Ethene escaping from flares was visualized in emission against the cold sky background. A method for deriving the flux of the gas plume by combining a wind vector map with a calibrated gas path-integrated concentration image has also been investigated.

**Paper IV** describes simultaneous open-air monitoring of methane, water vapor and oxygen using diode laser absorption spectroscopy. Two near-infrared diode laser beams were combined in a difference-frequency scheme yielding a third beam. The methane monitoring at 3.4  $\mu\text{m}$  was possible with ambient methane levels over a 15 m path and an isotopic molecular selectivity at reduced pressures was demonstrated.

**Paper V** describes a new instrument based on a diode laser in a coupled cavity for single aerosol particle size and shape determination. A novel feature is the simultaneous recording of the optical extinction due to a particle and the resulting diffraction image in the near-forward scattered light.

The author is responsible for a major part of the work in Papers I-III and V, including system construction and integration, programming, computer simulations, experimental work and the writing of manuscripts. For Paper IV, the author was involved in the experimental work, the evaluation of data and the writing of manuscript.

## **Acknowledgements**

I wish to express my sincere gratitude to all those who have contributed and made these Ph D studies pleasant and interesting and particularly to:

Sune Svanberg, supervisor, for giving me the opportunity to study more physics and for sharing with me his scientific ideas in high spirits.

Hans Edner, supervisor, for his friendship and all the invaluable discussions.

Ulf Gustafsson, for his friendship and interesting discussions.

Gabriel Somesfalean, for his collaboration, enthusiasm and sense of humor.

Petter Weibring, for helping me with measurements at the Gas Test Station in Malmö and for long friendship throughout the years of studies.

Sven-Åke Ljungberg, Royal Institute of Technology, Centre of Built Environment, for helping me with measurements at the Gas Test Station in Malmö and for stimulating discussions concerning infrared cameras.

Dag von Gegerfelt, Melles Griot AB, for support and encouragement.

Jan Hultqvist, at the workshop for all the help in making excellent instruments.

Mats Bohgard, Ergonomics and Aerosol Technology, and Erik Swietlicki, Nuclear Physics, for sharing their insightful knowledge on light scattering and for introducing me to the science of aerosol particles.

Maria Hansson, Department of Applied Electronics, for many fruitful discussions concerning image processing methodology.

The colleagues at Atomic Physics and especially, Anders Persson, Sven-Göran Pettersson, Bertil Hermansson, Stefan Andersson-Engels, Stefan Kröll, Anne L'Huillier, Åke Bergquist, Claes af Klinteberg, Laila Lewin, Lena Roos and Göran Werner.

My parents Margot and Per, for the never-ending love, support and encouragement.

My well-beloved Maria, with her understanding and love this work could be accomplished. And finally, Erik –let's build some railway now.

## References

1. M. W. Sigrist (Ed.), *Air Monitoring by Spectroscopic Techniques* (John Wiley & Sons, New York 1994).
2. U. Platt, "Differential optical absorption spectroscopy (DOAS)" in Ref. 1.
3. P. L. Hanst and S. T. Hanst, "Gas measurement in the fundamental infrared region" in Ref. 1.
4. M. L. Polak, J. L. Hall and K. C. Herr, "Passive Fourier-transform infrared spectroscopy of chemical plumes: an algorithm for quantitative interpretation and real-time background removal," *Appl. Opt.* **34**, 5406-5412 (1995).
5. D. Spänkuch, W. Döhler, J. Güldner and E. Schulz, "Estimation of the amount of tropospheric ozone in a cloudy sky by ground-based Fourier-transform infrared emission spectroscopy," *Appl. Opt.* **37**, 3133 (1998).
6. H. I. Schiff, G. I. Mackay and J. Bechara, "The use of tunable diode laser absorption spectroscopy for atmospheric measurements" in Ref. 1.
7. S. Svanberg, "Differential absorption LIDAR" in Ref. 1.
8. H. Edner, K. Fredriksson, A. Sunesson, S. Svanberg, L. Unéus and W. Wendt, "Mobile remote sensing system for atmospheric monitoring," *Appl. Opt.* **26**, 4330 (1987).
9. H. Edner, P. Ragnarson and E. Wallinder, "Industrial emission control using lidar techniques," *Environ. Sci. Technol.* **29**, 330 (1995).
10. T. G. McRae and T. J. Kulp, "Backscatter absorption gas imaging: a new technique for gas visualization," *Appl. Opt.* **32**, 4037 (1993).
11. T. G. McRae and L. L. Altpeter, "Natural gas leak dispersion studies using an infrared gas imaging system," *Proc. SPIE* **2366**, 124 (1995).
12. T.J. Kulp, P.E. Powers and R. Kennedy, "Remote imaging of controlled gas releases using active and passive infrared imaging systems," in *Infrared Technology and Applications XXIII*, B.F. Andresen and M. Strojnik Scholl, eds., *Proc. SPIE* **3061**, 269 (1997).
13. T. J. Kulp, P. Powers, R. Kennedy and U.-B. Goers, "Development of a pulsed backscatter-absorption gas-imaging system and its application to the visualization of natural gas leaks," *Appl. Opt.* **37**, 3912 (1998).
14. P. E. Powers, T. J. Kulp and R. Kennedy, "Demonstration of differential backscatter absorption gas imaging," *Appl. Opt.* **39**, 1440 (2000).
15. S.-Å. Ljungberg, T. J. Kulp and T. G. McRae, "State-of-the-art and future plans for IR imaging of gaseous fugitive emission," in *Thermosense XIX*, R. N. Wurzbach and D. D. Burleigh, eds., *Proc. SPIE* **3056**, 2 (1997).
16. C. Allander, P. Carlsson, B. Hallén, B. Ljungqvist and O. Norlander, "Thermocamera a macroscopic method for the study of pollution with nitrous oxide in operating theatres", *Acta Anaesth. Scand.* **25**, 21-24 (1981).
17. W. M. ter Kuile, J. J. F. van Veen, and B. Knoll, "Design and use of the infrared gas cloud scanner for measurements and imaging of the spatial distribution of gases at workplaces," *Proc. SPIE* **2366**, 135 (1995).
18. C. T. Nguyễn, A. Galais and G. Fortunato, "Pollution imagery by optical interferometry: application to SO<sub>2</sub> gas," *Appl. Opt.* **34**, 5398 (1995).

19. C. T. Nguyễn, B. Journet and G. Fortunato, "Description of an acquisition unit for optical interferometry treatment: Application to the pollution imagery of SO<sub>2</sub> gas," *Rev. Sci. Instrum.* **66**, 5183 (1995).
20. W. J. Marinelli, C. M. Gittins, A. H. Gelb and B. D. Green, "Tunable Fabry-Perot etalon-based long-wavelength infrared imaging spectroradiometer," *Appl. Opt.* **38**, 2594 (1999).
21. D. R. Suhre and E. Villa, "Imaging spectroradiometer for the 8-12- $\mu$ m region with a 3-cm<sup>-1</sup> passband acousto-optic tunable filter," *Appl. Opt.* **37**, 2340 (1998).
22. J. R. Drummond, "Novel correlation radiometer: the length-modulated radiometer," *Appl. Opt.* **28**, 2451 (1989).
23. J. R. Drummond, G. V. Bailak, and G. Mand, "Measurements of carbon monoxide and methane from space," in *Proceedings of the International Geoscience and Remote Sensing Symposium* (Institute of Electrical and Electronics Engineers, New York, 1994), p. 681.
24. J. C. Gille, L. Pan, M. W. Smith, and P. L. Bailey, "Retrieval of carbon monoxide profiles and total methane columns from MOPITT measurements," in *Proceedings of the International Geoscience and Remote Sensing Symposium* (Institute of Electrical and Electronics Engineers, New York, 1994), p. 684.
25. M. W. Smith, "Bandpass optimization for total column measurements of atmospheric CO and CH<sub>4</sub> using a length modulated gas filter correlation radiometer," in *Proceedings of the International Geoscience and Remote Sensing Symposium* (Institute of Electrical and Electronics Engineers, New York, 1994), p. 687.
26. M. W. Smith, "Method and results for optimizing the MOPITT methane bandpass," *Appl. Opt.* **36**, 4285 (1997).
27. P. Chazette, C. Clerbaux and G. Mégie, "Direct estimate of methane radiative forcing by use of nadir spectral radiances," *Appl. Opt.* **37**, 3113 (1998).
28. V. Norkus, T. Sokoll and G. Gerlach, "Thermal infrared radiators for analytical applications," in *Infrared Sensors & Systems 6*, *Proc. IRS<sup>2</sup>* **2.3**, 65 (2000).
29. K. J. Ebeling, *Integrated Optoelectronics - Waveguide Optics* (Springer-Verlag, 1993).
30. S. M. Sze, *Semiconductor Devices* (John Wiley & Sons, Singapore 1985), pp. 267-278.
31. M. J. Missey, S. Russell, V. Dominic, R. G. Batchko and K. L. Schepler, "Real-time visualization of domain formation in periodically poled lithium niobate," *Opt. Exp.* **6**, 186 (2000).
32. K. P. Petrov, S. Waltman, E. J. Dlugokencky, M. Arbore, M. M. Fejer, F. K. Tittel and L. W. Hollberg, "Precise measurement of methane in air using diode-pumped 3.4- $\mu$ m difference-frequency generation in PPLN," *Appl. Phys. B* **64**, 567 (1997).

33. U. Simon, C. E. Miller, C. C. Bradley, R. G. Hulet, R. F. Curl and F. K. Tittel, "Difference-frequency generation in AgGaS<sub>2</sub> by use of single-mode diode-laser pump sources," *Opt. Lett.* **18**, 1062 (1993).
34. R. M. Michalcea, M. E. Webber, D. S. Baer, R. K. Hanson, G. S. Feller, W. B. Chapman, "Diode-laser absorption measurements of CO<sub>2</sub>, H<sub>2</sub>O, N<sub>2</sub>O, and NH<sub>3</sub> near 2.0 μm," *Appl. Phys. B* **67**, 283 (1998).
35. D. G. Lancaster, D. Richter, R. F. Curl and F. K. Tittel, "Real-time measurements of trace gases using a compact difference-frequency-based sensor operating at 3.5 μm," *Appl. Phys. B* **67**, 339 (1998).
36. K. P. Petrov, R. F. Curl and F. K. Tittel, "Compact laser difference-frequency spectrometer for multicomponent trace gas detection," *Appl. Phys. B* **66**, 531 (1998).
37. D. G. Lancaster, D. Richter, R. F. Curl, F. K. Tittel, L. Goldberg and J. Koplow, "High-power continuous-wave mid-infrared radiation generated by difference frequency mixing of diode-laser-seeded fiber amplifiers and its application to dual-beam spectroscopy," *Opt. Lett.* **24**, 1744 (1999).
38. T. Kelz, A. Schumacher, M. Nägele, B. Sumpf and H.-D. Kronfeldt, "Detection of CO in air using diode laser pumped difference-frequency generation in modular setup," *J. Quant. Spectrosc. Radiat. Transfer* **61**, 591 (1999).
39. L.S. Rothman, C.P. Rinsland, A. Goldman, S.T. Massie, D.P. Edwards, J.-M. Flaud, A. Perrin, C. Camy-Peyret, V. Dana, J.-Y. Mandin, J. Schroeder, A. McCann, R.R. Gamache, R.B. Wattsin, K. Yoshino, K.V. Chance, K.W. Juck, L.R. Brown, V. Nemtchechin, P. Varanasi, The HITRAN molecular spectroscopic database: 1996 edition., *J. Quant. Spectrosc. Radiat. Transfer* **60**, 665 (1998).
40. P. L. Hanst, QASoft '96, Database and quantitative analysis program for measurements of gases (Infrared Analysis, Anaheim, Ca, 1996).
41. B. Funke, F. J. Martin-Torres, G. P. Stiller, M. Lopez-Puertas and N. Glatthor, "Spectroscopic requirements for MIPAS/ENVISAT non-LTE analysis," *Proc. 6<sup>th</sup> Biennial HITRAN Database Conference* (2000).
42. G. Herzberg, *Molecular spectra and molecular structure I. Spectra of diatomic molecules* (Krieger, Malabar 1989), pp. 121-126.
43. E. J. McCartney, *Absorption and Emission by Atmospheric Gases* (John Wiley & Sons, New York 1983).
44. K. F. Luft, "Über eine neue methode der registrierenden gasanalyse mit hilfe der absorption ultraroter strahlung ohne spektrale zerlegung," *J. Tech. Phys.* **24**, 97 (1943).
45. R. Goody, "Cross-correlating spectrometer," *J. Opt. Soc. Am.* **58**, 900 (1968).
46. T. V. Ward and H. H. Zwick, "Gas cell correlation spectrometer: GASPEC," *Appl. Opt.* **14**, 2896 (1975).
47. H. S. Lee and H. H. Zwick, "Gas filter correlation instrument for the remote sensing of gas leaks," *Rev. Sci. Instr.* **56**, 1812 (1985).

48. S. Cha, "Application of an infrared gas-filter correlation spectrometer for measurement of methanol concentrations in automobile exhausts," *Proc. SPIE* **685**, 211 (1986).
49. M. B. Sinclair, M. A. Butler, A. J. Ricco and S. D. Senturia, "Synthetic spectra: a tool for correlation spectroscopy," *Appl. Opt.* **36**, 3342 (1997).
50. G. Mouret, W. Chen, D. Boucher, R. Bocquet, P. Mounaix and D. Lippens, "Gas filter correlation instrument for air monitoring at submillimeter wavelengths," *Opt. Lett.* **24**, 351 (1999).
51. H. Edner, S. Svanberg, L. Un eus, and W. Wendt, "Gas-correlation lidar," *Opt. Lett.* **9**, 493 (1984).
52. GRAMS/32, Array basic programming language (Galactic Industries).
53. J. Gebhart, D. J. Rader, T. J. O'Hern, P. A. Baron, M. K. Mazumder, and Y. S. Cheng, "Aerosol Measurement," K. Willeke and P. A. Baron, eds. (Van Nostrand Reinhold, New York, 1993), Chap. 15-17.
54. L. Morawska, N. D. Bofinger, and M. Maroni, eds., *Indoor Air* (Elsevier Science, Oxford, 1995).
55. OSLO, Optics Software for Layout and Optimization Ver 5.4, Optics Reference pp. 349-351 (Sinclair Optics, 2000).
56. H. C. van de Hulst, *Light scattering by small particles* (John Wiley & Sons, New York, 1983).
57. C. F. Bohren and D. R. Huffman, *Absorption and Scattering of Light by Small Particles* (John Wiley & Sons, New York, 1983).
58. M. Bottlinger and H. Umhauer, "Modeling of light scattering by irregularly shaped particles using a ray-tracing method," *Appl. Opt.* **30**, 4732 (1991).
59. A. Macke, M. I. Mishchenko, K. Muinonen and B. E. Carlson, "Scattering of light by large nonspherical particles: ray-tracing approximation versus T-matrix method," *Opt. Lett.* **20**, 1934 (1995).
60. J. R. Zijp and J. J. ten Bosch, "Pascal program to perform Mie calculations," *Opt. Eng.* **32**, 1691 (1993).
61. M. Fayngold, "Spherical particle imaging and glare-ring spectroscopy with backscattered light," *J. Opt. Soc. Am.* **14**, 1825 (1997).
62. C. Heffels, D. Heitzmann, E. D. Hirleman and B. Scarlett, "Forward light scattering for arbitrary sharp-edged convex crystals in Fraunhofer and anomalous diffraction approximations," *Appl. Opt.* **34**, 6552 (1995).
63. R. Breiter, W. Cabanski, R. Koch, K.-H. Mauk, W. Rode, J. Ziegler, K. Eberhardt, R. Oelmaier, M. Walther and H. Schneider, "Large format focal plane array IR detection modules and digital signal processing," in *Infrared Sensors & Systems 6*, *Proc. IRS<sup>2</sup>* **1.1**, 25 (2000).
64. J. Y. Andersson, L. Lundqvist and Z. F. Paska, "Quantum efficiency enhancement of AlGaAs/GaAs quantum well infrared detectors using a waveguide with a grating coupler," *Appl. Phys. Lett.* **58**, 2264 (1991).
65. J. Y. Andersson and L. Lundqvist, "Near-unity quantum efficiency of AlGaAs/GaAs quantum well infrared detectors using a waveguide with a doubly periodic grating coupler," *Appl. Phys. Lett.* **59**, 857 (1991).

66. L. Lundqvist, J. Y. Andersson and J. Borglind, "GaAs/AlGaAs Quantum Well Infrared Photodetector Arrays for Thermal Imaging Applications," *Physica Scripta* **T54**, 131 (1994).
67. J. Y. Andersson and L. Lundqvist, "Grating-coupled quantum-well infrared detectors: Theory and performance," *J. Appl. Phys.* **71**, 3600 (1992).
68. B. H. Walker, *Optical Engineering Fundamentals* (McGraw-Hill, New York, 1994).
69. P. S. Andersson, S. Montán and S. Svanberg, "Multispectral system for medical fluorescence imaging," *IEEE J. Quantum Electron.* **QE-23**, 1798 (1987).
70. P. Kauranen, S. Andersson-Engels and S. Svanberg, "Spatial mapping of flame radical emission using a spectroscopic multi-colour imaging system," *Appl. Phys. B* **53**, 260 (1991).
71. B. G. Schuster and R. Knollenberg, "Detection and sizing of small particles in an open cavity gas laser," *Appl. Opt.* **11**, 1515 (1972).
72. J. Sandsten, "Optical methods for detection of very small vibrations and Design of a laser diode system using optical feedback," *Lund Reports on Atomic Physics* **LRAP-163** (1994).
73. D. M. Kane and A. P. Willis, "External-cavity diode lasers with different devices and collimating optics," *Appl. Opt.* **34**, 4316 (1995).
74. R. P. Salathé, "Diode lasers coupled to external resonators," *Appl. Phys.* **20**, 1 (1979).
75. R. Lang and K. Kobayashi, "External optical feedback effects on semiconductor injection laser properties," *IEEE J. Quantum Electron.*, **QE-16**, 347 (1980).
76. J. Sacher, W. Elsässer and E. O. Göbel, "Nonlinear dynamics of semiconductor laser emission under variable feedback conditions," *IEEE J. Quantum Electron.*, **QE-27**, 373 (1991).
77. J. Mørk, B. Tromborg and J. Mark, "Chaos in semiconductor lasers with optical feedback: Theory and experiments," *IEEE J. Quantum Electron.* **QE-28**, 93 (1992).
78. P. Besnard, B. Meziane and G. M. Stéphan, "Feedback phenomena in a semiconductor laser induced by distant reflectors," *IEEE J. Quantum Electron.*, **QE-29**, 1271 (1993).
79. M.-W. Pan, B.-P. Shi and G. R. Gray, "Semiconductor laser dynamics subject to strong optical feedback," *Opt. Lett.* **22**, 166 (1997).
80. J. S. Lawrence and D. M. Kane, "Influence of the angular alignment of the optical feedback field on external cavity diode laser characteristics," *Opt. Comm.* **159**, 316 (1999).
81. J. Kitching, R. Boyd, Y. Shevy and A. Yariv, "Amplitude noise reduction in semiconductor lasers with weak, dispersive optical feedback," *Opt. Lett.* **19**, 1331 (1994).
82. J. Mørk, B. Tromborg, J. Mark and V. Velichansky, "Instabilities in a laser diode with strong optical feedback," *Proc. SPIE* **1837**, (1992).

83. G. D. Boyd and D. A. Kleinman, "Parametric interaction of focused Gaussian light beams," *J. Appl. Phys.* **39**, 3597 (1968).
84. R. C. Gonzalez and R. E. Woods, *Digital Image Processing* (Addison Wesley, New York, 1993).
85. M. Petrou, P. Bosdogianni, *Image Processing The Fundamentals* (John Wiley & Sons, England 1999).
86. C. Werner, R. Haus, F. Köpp and K. Schäfer, "Remote sensing of mass fluxes of trace gases in the boundary layer," *Appl. Phys. B* **61**, 249 (1995).
87. P. Weibring, M. Andersson, H. Edner and S. Svanberg, "Remote monitoring of industrial emissions by combination of lidar and plume velocity measurements," *Appl. Phys. B* **66**, 383 (1998).
88. P. Bergamaschi, M. Schupp and G. W. Harris, "High-precision direct measurements of  $^{13}\text{CH}_4/^{12}\text{CH}_4$  and  $^{12}\text{CH}_3\text{D}/^{12}\text{CH}_4$  ratios in atmospheric methane sources by means of a long-path tunable diode laser absorption spectrometer," *Appl. Opt.* **33**, (1994).

I

# Gas imaging by infrared gas-correlation spectrometry

Jonas Sandsten, Hans Edner, and Sune Svanberg

Department of Physics, Lund Institute of Technology, P.O. Box 118, S-221 00 Lund, Sweden

Received July 8, 1996

We describe a new method for visualization of gas flows based on infrared absorption and gas-correlation techniques. This result is a gray-scale or false color-coded image showing the distribution of a specific gas in the area studied. A sequence of images showing the workplace test setup with a turbulent flowing gas is presented. © 1996 Optical Society of America

In many applications there is an interest in finding and visualizing gas plumes in real time. Images of gas concentration distributions are needed in several environmental studies. Global mapping of greenhouse gases from spacecraft-based systems is important.<sup>1-3</sup> Two industrial applications are hydrocarbon emission monitoring from petrochemical installations and leakage detection along pipelines. Indoor monitoring of the working environment and surveillance of hazardous gases are other fields for which imaging is useful. Nitrous oxide leaking from anesthetic masks in operating theaters has been studied with an IR camera with absorption of the gas throughout the spectral region of the camera.<sup>4</sup> The gas can be confined by turbulent flow around the breathing zone of the anesthetist, and ventilation aspects are studied with this method. An active method that uses a carbon dioxide laser that scans the detector field of view is one way to detect gas leaks in industrial environments.<sup>5</sup> Another method uses IR emitters and a retroreflector screen to visualize gas absorption.<sup>6</sup> Gas-correlation spectrometry<sup>7</sup> is a particularly simple and powerful technique that uses an absorption spectrum in a measuring system that is compared with the spectrum of incoming light, and a signal proportional to the number of absorbing molecules of a specific kind is generated. Gas-correlation spectrometry was employed previously in passive point monitoring<sup>8</sup> and in laser radar.<sup>9</sup>

We describe a new method that makes it possible to visualize gases and estimate their concentrations in a two-dimensional image based on IR absorption and gas-correlation techniques. First we recapitulate the point monitoring principle (Fig. 1). The incoming light is sent through a cell containing the gas to be studied at such high concentration that little or no light can pass at the absorption wavelength and then through a variable neutral-density filter. With no external gas present the variable filter is adjusted so that equal intensities are obtained in the spectral region cut out by a bandpass filter. Now, if an external pollution plume is present the signal in the gas cell arm is not affected (except for a minor broadening of the absorption lines) because no more than full absorption can be obtained. The incoming light in the other arm is reduced because of absorption lines in the plume. The imbalance introduced into the two arms is a measure of the gas

concentration in the plume. Note that the presence of interfering gases does not affect the concentration measurement.

In our experiments two images of the flowing gases are formed at the same time on an IR-sensitive camera with a compact Cassegrainian split-mirror telescope.<sup>10</sup> A bandpass filter is used to isolate a small spectral region containing absorption features of the gas to be studied. In front of one part of the telescope a short CaF<sub>2</sub> cell filled with a high concentration of the gas is mounted. The other part of the telescope gives a direct image. The images are correlated in a computer to eliminate differences in background illumination as well as the interference by other gases and particles. The correlation or image processing consists of mainly two steps, in which the first step is to

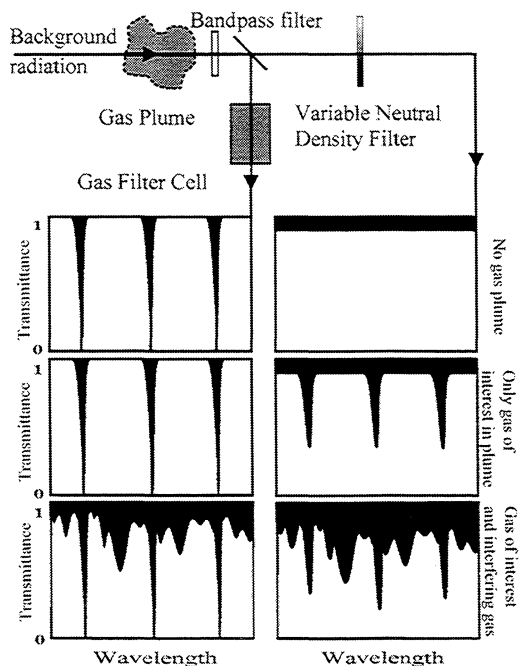


Fig. 1. Point monitoring principle of a gas-correlation spectrometer.

choose a region of interest in the direct image. The direct image is then divided with the gas-filtered image. To divide the images without losing intensity dynamics we multiply the gas-filtered image by a factor. The other step is to optimize the overlap between the images by minimizing the standard deviation of the divided images, which cancels the background and interfering gases. The result is a gray-scale or false color-coded picture showing only the distribution of the specific gas. Flow and concentration in two dimensions can be presented in nearly real time.

Experiments have been performed on flows of methane, nitrous oxide, and carbon dioxide at a workplace test setup as shown in Fig. 2. An Agema Thermovision 900 SW system was employed, and the images were converted from an industrial file format to standard file formats and processed with Concept V.i software on a LabView platform. The camera detector (InSb) was cooled to 77 K, and its sensitivity to IR radiation in the region 2–5.6  $\mu\text{m}$  was restricted by use of either of two bandpass filters, with center wavelengths at 3.35 and 4.54  $\mu\text{m}$  and full half-widths of 0.16 and 0.27  $\mu\text{m}$ , respectively. We chose the filters by using the HITRAN database<sup>11</sup> for the detection of methane and nitrous oxide, but carbon dioxide and water also absorb in these regions. An IR heater was used to illuminate the background. We created a turbulent flow from the nozzle by letting the gases pass through a water lock. In our experiments we mixed the gases by using pressure regulators and in that way controlled the composition of the gas flow. Figure 3 shows the spectral region cut out by the bandpass filter with a center wavelength of 4.54  $\mu\text{m}$ . As can be seen,  $\text{CO}_2$  and  $\text{N}_2\text{O}$  do not interfere in this region, but the simultaneous capture of the direct and the gas-filtered images has the advantage of ensuring that background radiation variation and motion do not affect the resulting image.

Correlation spectrometry enhances the signal-to-noise ratio in the small spectral region cut out by the bandpass filters by turning the gas of interest into its own spectral filter, thereby specifically selecting the gas. In Fig. 4, as an example, the absorption lines of  $\text{C}_2\text{H}_6$  (solid curves) are seen to interfere with the absorption lines of  $\text{CH}_4$ , but it is possible to discriminate  $\text{C}_2\text{H}_6$  from  $\text{CH}_4$  with the gas-correlation approach. Several interesting and environmentally important gases, such as hydrocarbons, sulfur compounds, and nitrous compounds, have vibration-rotation absorption in the IR region. The absorption strength of the gases that we examined increases with the wavelength in the region 2–5.6  $\mu\text{m}$ , but the detector sensitivity falls off with increasing wavelength. This trade-off forced us to choose spectral regions within 3–4.5  $\mu\text{m}$ . Another trade-off is the fact that more energy hits the detector with broad bandpass filters but the specificity of the gas as a spectral filter, with respect to signal-to-noise, is worse with broad bandpass filters. Careful design of the bandpass filters and estimates of the total gas absorption strengths are needed. Water absorbs over broad spectral regions, with strong absorption in some cases, and we take this into account by positioning the bandpass

filters in spectral windows where water absorption is weak.

The resulting images in a sequence of four with 1 s between successive images are shown in Fig. 5. In image 1 a person is approaching the workplace setup with turbulent flowing gases from the water lock. The gas that is seen is nitrous dioxide in a mixture of carbon dioxide and water. In image 2 the person starts to move against the nozzle and thereby disturbs the flow. Image 3 shows the person in profile holding his breath. Image 4 shows a movement with the left arm. The sequence continues with six more images and can be shown as a movie. One of the more important aspects of these photographs, besides the fact that a specific gas can be visualized, is the effect that such a movie

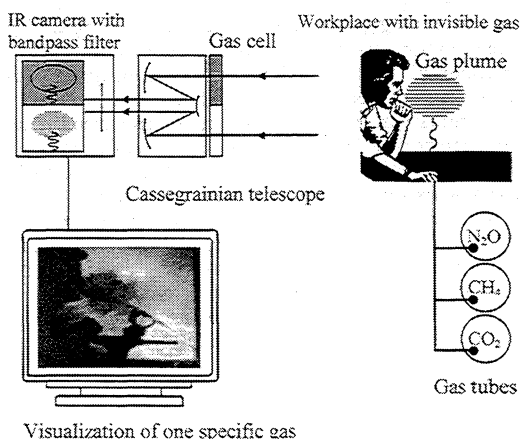


Fig. 2. Schematic diagram of the experimental arrangement.

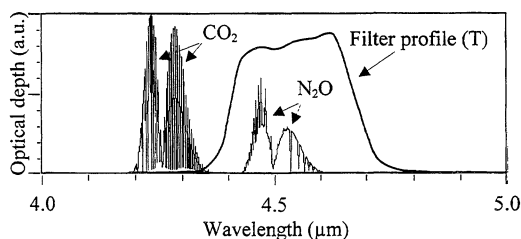


Fig. 3. Spectral features of  $\text{CO}_2$  and  $\text{N}_2\text{O}$ . The transmission of the bandpass filter used is also indicated ( $T_{\text{max}} = 85\%$ ).

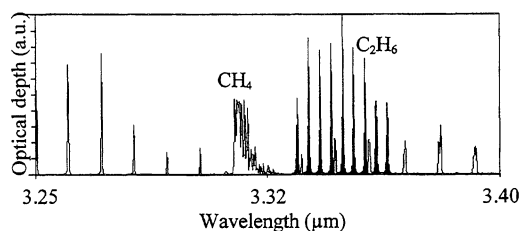


Fig. 4. Interfering spectral features of  $\text{CH}_4$  and  $\text{C}_2\text{H}_6$ .

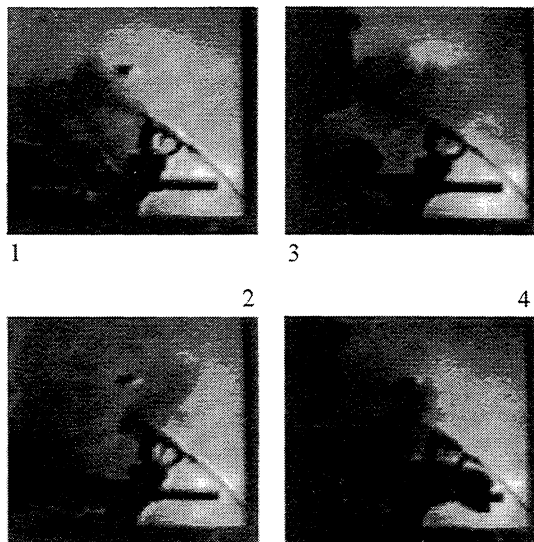


Fig. 5. Gas-correlated images in sequence (without gray-scale manipulation). The visualized gas was  $N_2O$  in a mixture of water vapor and  $CO_2$ . The time between successive pictures was 1 s.

has on workers in real working environments.<sup>12</sup> The power of showing his or her exposure to a worker makes it possible for him or her to avoid certain dangerous work steps, and the ability to use the movie as a tool for creative discussions between employee and employer is useful in designing protection and avoiding hazardous gas. For qualitative purposes the images in Fig. 5 can be enhanced with a gray-scale equalization.

To estimate the concentration of a specific gas one can calibrate the instrument against a group of cells with known gas partial pressures. Various mixtures of air and the gas of interest can be used in standard cells. A nonlinear model is suited to curve-fit data to the standard cells.<sup>13</sup> In the present setup the optical system gives some parallax and vignetting errors, which it should be possible to mitigate with another design of the Cassegrainian telescope. The vignetting is most easily seen in image 1 of Fig. 5 as a dark area in the lower left-hand corner and as a light area in the lower right-hand corner. The parallax results from the finite separation of the two openings of the telescope, through which the workplace setup was observed at a rather short distance. The background was illuminated by an IR lamp because the camera was not sensitive enough for the detection of passive thermal radiation with the available standard bandpass filters. However, better bandpass filters tuned to regions where the absorption lines are stronger and more sensitive cameras [e.g., an Agema Thermovision 1000

system using a Stirling cooled MCT signal-processing-in-the-element (SPRITE) detector, in the region of 8–12  $\mu\text{m}$ , with  $798 \times 400$  pixels/image] are available, making practical gas-correlation imaging using thermal background light fully feasible.

In conclusion, we have visualized environmentally important gases with a simple and straightforward technique, using the IR spectral features of the gas as its own spectral filter. Our system is capable of separating interfering gases, and it is insensitive to background and motion variations because of simultaneous capture of the direct and the gas-filtered images. The capture rate is two images/s. Methane, nitrous oxide, and carbon dioxide were gas correlated to give images in nearly real time of the flowing gas at a workplace test setup.

We thank Thomas Blomberg, Department of Building Physics, Lund Institute of Technology, for lending us the IR camera and Ulf Gustafsson and Mats Andersson for their help with computers. This research was funded in part by the National Institute for Working Life and in part by the Swedish Space Board.

## References

1. J. R. Drummond, G. V. Bailak, and G. Mand, in *Proceedings of the International Geoscience and Remote Sensing Symposium* (Institute of Electrical and Electronics Engineers, New York, 1994), p. 681.
2. J. C. Gille, L. Pan, M. W. Smith, and P. L. Bailey, in *Proceedings of the International Geoscience and Remote Sensing Symposium* (Institute of Electrical and Electronics Engineers, New York, 1994), p. 684.
3. M. W. Smith, in *Proceedings of the International Geoscience and Remote Sensing Symposium* (Institute of Electrical and Electronics Engineers, New York, 1994), p. 687.
4. C. Allander, P. Carlsson, B. Hallén, B. Ljungqvist, and O. Norlander, *Acta Anaesth. Scand.* **25**, 21 (1981).
5. T. G. McRae and L. L. Altpeter, *Proc. SPIE* **2366**, 124 (1995).
6. W. M. ter Kuile, J. J. F. van Veen, and B. Knoll, *Proc. SPIE* **2366**, 135 (1995).
7. T. V. Ward and H. H. Zwick, *Appl. Opt.* **14**, 2896 (1975).
8. H. S. Lee and H. H. Zwick, *Rev. Sci. Instrum.* **56**, 1812 (1985).
9. H. Edner, S. Svanberg, L. Unéus, and W. Wendt, *Opt. Lett.* **9**, 493 (1984).
10. P. S. Andersson, S. Montán, and S. Svanberg, *IEEE J. Quantum Electron.* **QE-23**, 1798 (1987).
11. HITRAN database, 1992 ed., V. 2.41, developed by the University of South Florida and the Ontar Corporation, based on L. S. Rothman, R. R. Gamache, R. H. Tipping, C. P. Rinslaud, M. A. H. Smith, D. C. Benner, V. Malathi Devi, J.-M. Flaud, C. Camy Peyret, A. Goldman, S. T. Massie, L. R. Brown, and R. A. Toth, *J. Quant. Spectrosc. Radiat. Transfer* **48**, 469 (1992).
12. I. M. Andersson and G. Rosén, *Appl. Occup. Environ. Hyg.* **10**, 537 (1995).
13. S. Cha, *Proc. SPIE* **2252**, 211 (1986).

II

# Real-time gas-correlation imaging employing thermal background radiation

Jonas Sandsten, Petter Weibring, Hans Edner and Sune Svanberg  
Department of Physics, Lund Institute of Technology, P.O. Box 118, S-221 00 Lund, Sweden  
Jonas.Sandsten@fysik.lth.se

<http://www-atom.fysik.lth.se>

**Abstract:** Real-time imaging of gas leaks was demonstrated using an IR camera employing outdoor thermal background radiation. Ammonia, ethylene and methane detection was demonstrated in the spectral region 7-13  $\mu\text{m}$ . Imaging was accomplished using an optical filter and a gas-correlation cell matching the absorption band of the gas. When two gases, such as ammonia and ethylene, are absorbing in the same wavelength region it is possible to isolate one for display by using gas-correlation multispectral imaging. Results from a field test on a leaking gas tanker are presented as QuickTime movies. A detection limit of 200 ppm  $\times$  meter for ammonia was accomplished in this setup when the temperature difference between the background and the gas was 18 K and the frame rate was 15 Hz.

©2000 Optical Society of America

**OCIS codes:** (040.3060) Detectors, infrared; (110.3080) Infrared imaging; (280.1120) Air pollution monitoring; (300.6340) Spectroscopy, infrared

---

## References and links

1. T.J. Kulp, P.I. Powers and R. Kennedy, "Remote imaging of controlled gas releases using active and passive infrared imaging systems," in *Infrared Technology and Applications XXIII*, B.F. Andresen, M. Strojnik Scholl, eds., Proc. SPIE **3061**, 269-278 (1997).
2. S.-A. Ijungberg, T.J. Kulp and T.G. McRae, "State-of-the-art and future plans for IR imaging of gaseous fugitive emission," in *Thermosense XIX*, R.N. Wurzbach, D.D. Burleigh, eds., Proc. SPIE **3056**, 2-19 (1997).
3. C. Allander, P. Carlsson, B. Hallén, B. Ljungqvist and O. Norlander, "Thermocamera a macroscopic method for the study of pollution with nitrous oxide in operating theatres", *Acta Anaesth. Scand.* **25**, 21-24 (1981).
4. T.G. McRae and T.J. Kulp, "Backscatter absorption gas imaging: a new technique for gas visualization," *Appl. Opt.* **32**, 4037-4050 (1993).
5. J. Sandsten, H. Edner and S. Svanberg, "Gas imaging by infrared gas-correlation spectrometry," *Opt. Lett.* **21**, 1945-1947 (1996). <http://www-atom.fysik.lth.se/JonasSandsten/GasCorrelationImaging.htm>.
6. T.V. Ward and H.H. Zwick, "Gas cell correlation spectrometer: GASPEC," *Appl. Opt.* **14**, 2896-2904 (1975).
7. H.S. Lee and H.H. Zwick, "Gas filter correlation instrument for the remote sensing of gas leaks," *Rev. Sci. Instr.* **56**, 1812-1819 (1985).
8. H. Edner, S. Svanberg, L. Unéus and W. Wendt, "Gas-correlation lidar," *Opt. Lett.* **9**, 493-495 (1984).
9. P.S. Andersson, S. Montán and S. Svanberg, "Multi-spectral system for medical fluorescence imaging," *IEEE J. Quant. Electr.* **QF-23**, 1798-1805 (1987).
10. L.S. Rothman, C.P. Rinsland, A. Goldman, S.T. Massie, D.P. Edwards, J.-M. Flaud, A. Perrin, C. Camy-Peyret, V. Dana, J.-Y. Mandin, J. Schroeder, A. McCann, R.R. Gamache, R.B. Wattsin, K. Yoshino, K.V. Chance, K.W. Juck, L.R. Brown, V. Nemtchechin, P. Varanasi, The HITRAN molecular spectroscopic database: 1996 edition., *J. Quant. Spectrosc. Radiat. Transfer* **60**, 665-710 (1998).
11. M.L. Polak, J.L. Hall and K.C. Herr, "Passive Fourier-transform infrared spectroscopy of chemical plumes: an algorithm for quantitative interpretation and real-time background removal," *Appl. Opt.* **34**, 5406-5412 (1995).
12. P.L. Hanst, QASoft '96, Database and quantitative analysis program for measurements of gases, Infrared Analysis Inc., Anaheim, Ca, 1996.
13. GRAMS/32. Array basic programming language, Galactic Industries Corp.

---

## 1. Introduction

Real-time gas imaging is of great interest in many contexts [1,2]. Inspection of leaks from chemical installations, petrochemical plants, tank farms or pipelines has economical,

environmental and security aspects. Easily deployable surveillance techniques for assessing sites of accidents involving gas tankers or trains are desirable for public safety considerations. In the indoor working environment, gas flow monitoring around air inlets and outlets, extraction hoods or local ventilation units is useful for optimizing the construction and adjustment of installations. Emissions of geophysical origin (volcanoes, geothermal installations or mines) as well as natural emanations of greenhouse gases from agriculture, swamps etc., are also interesting to assess. Useful spectroscopic absorption features of the molecules of interest occur in the visible or infrared spectral regions. The vibrational-rotational bands in the fundamental infrared region,  $3700\text{ cm}^{-1}$  to  $500\text{ cm}^{-1}$ , are particularly suitable for sensitive gas detection. While active monitoring of gases using lidar techniques is possible, range and imaging capabilities are limited. A passive system using ambient background radiation is more attractive for real-time imaging. In the present paper we demonstrate, as we believe for the first time, practical gas passive imaging with gas identification using a sensitive infrared camera combined with optical filter and gas cell correlation techniques. The method relies on simultaneous multi-spectral imaging and computer processing of the data. Results from a field test on a leaking gas tanker are presented.

Previous IR work has involved the use of heat blankets or IR illuminators to enhance the natural radiation level [3]. Scanning laser irradiation has been employed for close-range applications [4]. Recently, we demonstrated selective gas imaging using gas-correlation spectrometry for automatic gas identification, in a working environment scene employing added IR radiation [5]. The gas-correlation principle was originally introduced for line-of-sight monitoring and has later also been used in combination with lidar [6-8].

The virtue of the gas-correlation technique is the holistic discrimination between spectral frequencies with specific gas absorption and transparent areas, which is obtained by comparing a direct recording to a recording through an optically thick gas absorption cell. In our previous work we extended the principle to imaging by employing a technique for simultaneous multi-spectral recording using a specially designed split-mirror Cassegrainian telescope, allowing up to 4 geometrically similar but spectrally differently filtered images to be simultaneously recorded in the four quadrants of the 2D detector [9]. Two of the images were used, one direct image and one, which was filtered through a gas cell. Gas flows in an indoor working environment were visualized, but the IR camera employed, an Agema THV900 SW unit, had a sensitivity limit calling for the slight heating of the background scene using a 1000 W IR illuminator equipped with a reflector. Our present work has overcome some of the previous limitation by utilizing a more sensitive Agema THV900 LW system and more powerful image processing techniques to actually allow ambient thermal outdoor background radiation as the only illumination in real-time recordings at 15 frames/s. The special virtue of the gas-correlation technique is that it allows the separation of gases which have overlapping spectra (e.g. ammonia and ethylene). A proper IR wavelength window where the gases of interest absorb is chosen by a bandpass filter, but the high-resolution "holistic" filtering is performed by the optically thick correlation gas. The lay-out of the present paper is as follows. Detailed spectral considerations are presented in the next section, including a method to estimate gas concentration  $\times$  length, followed by a description in Sect. 3 of the experimental arrangements used in the field measurements. Our data processing and dynamic gas flow presentation are discussed in Sect. 4, followed by a section presenting our results. Finally, we conclude with a discussion section with suggestions for technology improvements and future work.

## 2. Spectral consideration

By using remote infrared detection techniques most species, except homonuclear diatomic species, can be detected and quantified due to their unique infrared spectral properties in the wavelength region  $3\text{-}13\ \mu\text{m}$  [10]. In order to choose the optimal wavelength region for passive detection several factors have to be taken into account. The most important factors are atmospheric transmission (i.e. water and carbon dioxide absorption), background radiation

flux and the integrated oscillator strengths of the absorption lines of the species of interest. Fig. 1 shows a typical atmospheric transmission in the IR region, together with the spectral radiances of five blackbody radiators with normal background temperatures ranging from 273 K to 313 K. As can be seen, water and carbon dioxide absorption block part of the spectrum or limit the effective range of optical measurements. The region from 8-13  $\mu\text{m}$  contains more water bands than the 3-4  $\mu\text{m}$  region, but the background radiation is more than 30 times higher at normal terrestrial temperatures, i.e. 300 K. The strength of the absorption band of many species of interest is also considerable higher in the 8-13  $\mu\text{m}$  region. Even though water interference in the 7-8.5  $\mu\text{m}$  (1400-1200  $\text{cm}^{-1}$ ) wavelength region is severely affecting the signals, it is possible to utilize this region for measurements of methane, employing the gas-correlation technique.

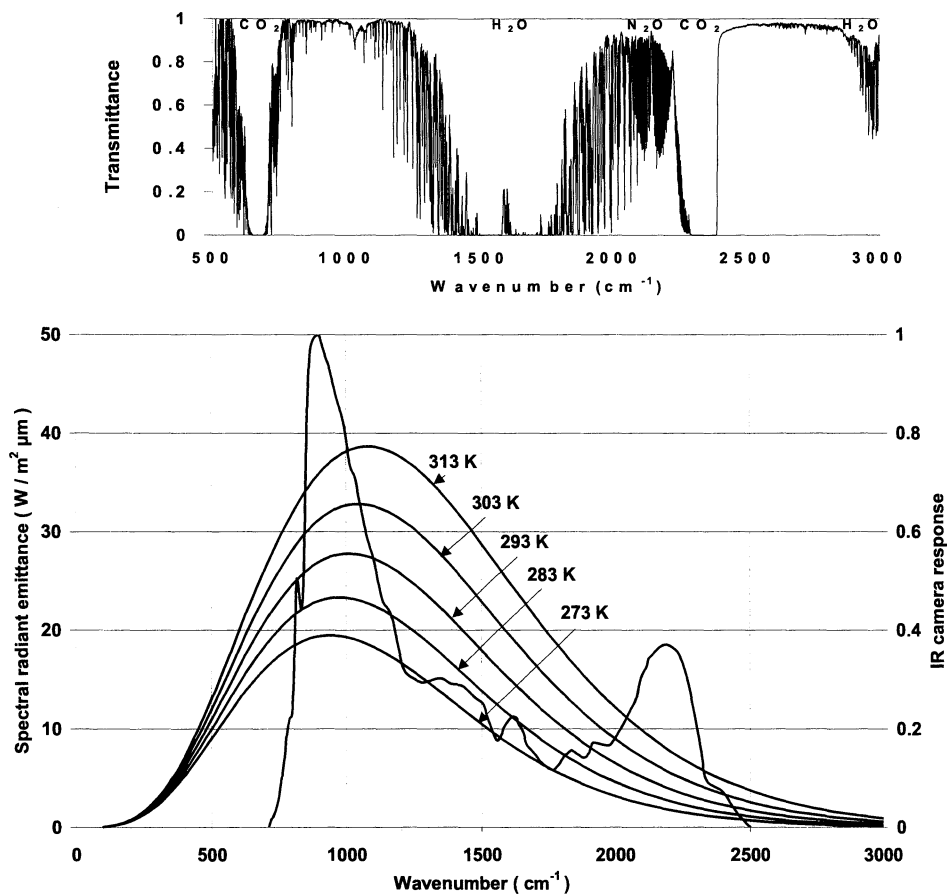


Fig. 1. Top: Atmosphere transmittance through 300 meters of urban air [12]. Bottom: Spectral radiance of five blackbody radiators (left axis) and the normalized spectral response curve of our IR camera (right axis).

Passive techniques using natural thermal background radiation for gas detection is very suitable around 1000  $\text{cm}^{-1}$  due to maximum spectral radiance for such temperatures and a greatly transparent atmosphere. Gases that absorb infrared radiation in this atmospheric window are affecting the sun-earth radiative balance, which in turn is affecting the temperature on earth. IR cameras manufactured for use in the atmospheric window around 1000  $\text{cm}^{-1}$ , are by definition also very suitable for visualization of greenhouse gas concentration gradients. Varying thermal background, reflectance or emittance over the image are compensated when using the imaging gas-correlation technique.

Taken into account these spectral considerations we choose an Agema Thermovision 900 LW infrared camera, which has a low noise-equivalent temperature difference, NE $\Delta$ T, of 80 mK. The relative spectral response, which is at its maximum at 900  $\text{cm}^{-1}$  (11  $\mu\text{m}$ ), is also shown in Fig. 1. together with the spectral radiances of five blackbody radiators.

Computer based convolution simulations for the spectral response of the camera system, comprised of the detector, camera optics, filters and gas-correlation cells, were performed. The simulation enabled determination of the properties of the whole optical transmission system except the Cassegrainian telescope which was considered not to influence the spectral response notably. Also profiling and determination of different filter types were possible. To achieve an optimal sensitivity is a question of balancing the use of narrow bandpass filters, optimized on strong spectral features, to yield a high contrast response, against the overall photon transmission in the system. Static noise in the detector requires the photon flux to be over a certain level to achieve a good signal-to-noise ratio. Furthermore, a bandpass filter is in itself radiating more than a short- or long-wavelength-pass filter. Therefore, by varying the wavelength region and its width, maximizing the ratio between the integrated total absorption of the gas of interest and the integrated total optical transmission of the system, an optimal filter profile can be selected.

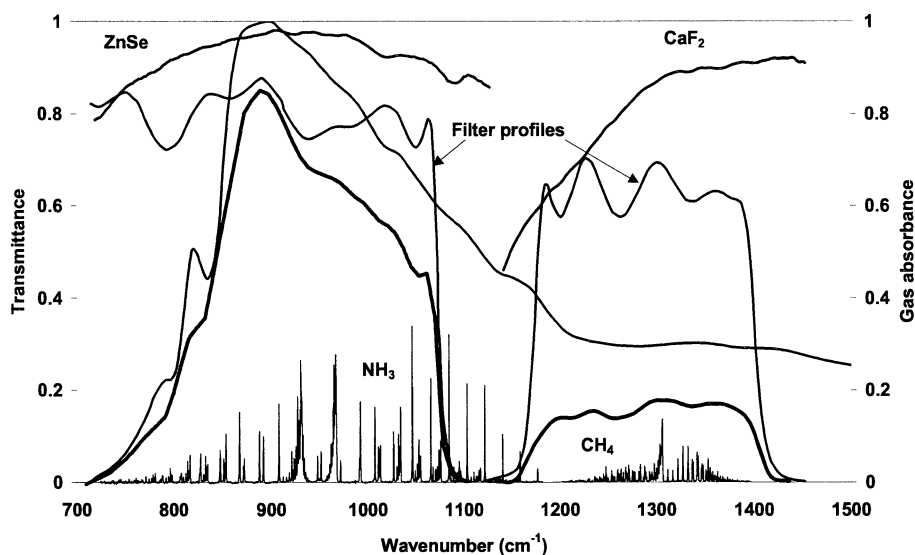


Fig. 2. The normalized spectral response of the IR camera (dark blue curve) is convoluted with the transmittance of two different gas cell window materials and optical filter profiles, yielding two regions of relative response (black curves). The gases are both shown in absorbance at concentrations of 200 ppm  $\times$  m.

As a result of the simulations, a best effort filter for detection of ammonia and ethylene in the 8-13  $\mu\text{m}$  wavelength region is a long-wavelength-pass filter (cut-on at 9.2  $\mu\text{m}$ ) with 80 % transmission and a best effort filter for detection of methane is a broad bandpass filter (half power points at 7  $\mu\text{m}$  and 8.5  $\mu\text{m}$ ) with 60 % transmission.

For the gas-correlation cell windows, several materials with transmission in the 2-13  $\mu\text{m}$  wavelength region were considered. We choose ZnSe for measurements of species with absorption around 10  $\mu\text{m}$ , and CaF<sub>2</sub> for species around 8  $\mu\text{m}$ ; see Fig. 2. The ZnSe window surfaces were antireflection coated to reduce the reflection loss due to a high index of refraction, yielding more than 90 % transmission with a maximum of 99 % at 10.6  $\mu\text{m}$ .

In Fig. 2 the transmittances of the discussed elements are shown together with the convoluted total response (black curves). FT-IR recorded spectra of 200 ppm  $\times$  meters of ammonia and methane are shown in units of gas absorbance as red and orange lines, respectively [12].

## 2.1 Gas concentration calibration

Gas concentration calibration for ammonia was performed by integrating the relative transmittance of the system over wavenumbers from 700 to 1100  $\text{cm}^{-1}$ , with increasing gas concentrations, and then dividing the decreasing integrated relative transmittance with the integrated relative transmittance without gas. This procedure is primarily described for the case of direct absorption measurements. In the process the databases HITRAN 1996, QASoft '96 and the software GRAMS/32 were used [10,12,13]. Fig. 3 shows convoluted spectra at two different concentration levels. The absorption line wing contribution influence was taken into account by using HITRAN composite spectra.

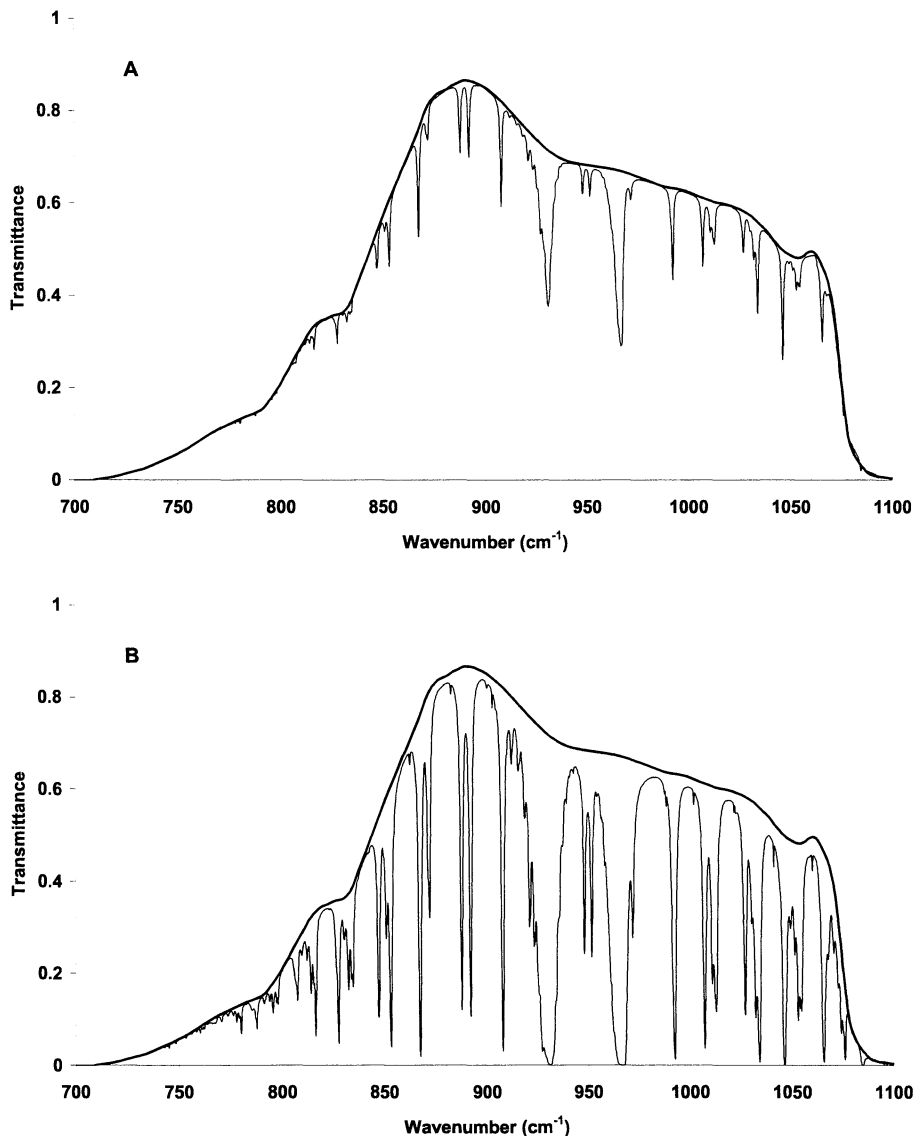


Fig. 3. A. Ammonia transmittance spectrum at a concentration of 400 ppm × m, convoluted with the system response. The black envelope integrated transmittance (no gas) divided by the integrated transmittance under the gas spectrum corresponds to the transmittance of the system. B. Ammonia transmittance spectrum at a concentration of 4000 ppm × m, convoluted with the system response.

Fig. 4 shows the integrated transmittance for different concentrations of ammonia, calculated from several convoluted spectra. This calculation was first performed for a very large temperature difference between the background and the gas. However, in a practical situation with a thermal background, the self-radiance from the gas has to be taken into account. The gas will selectively radiate at the absorption lines with an intensity of  $[(1 - \text{Transmittance}) \times B_G]$ , where  $B_G$  is the intensity of a blackbody radiator at the gas temperature  $T_G$ . This will be seen as a higher effective transmittance of the gas, and this effect can be calculated by adding the emitted intensity of the gas at temperature  $T_G$  to the transmitted intensity of the background at temperature  $T_B$ . The resulting corrected transmittance as a function of the concentration at the prevailing experimental value of  $\Delta T = 18 \text{ K}$  ( $\Delta T = T_B - T_G$ ) is shown in Fig. 4. We did not expect to find a Beer-Lambertian like relationship between gas transmittance and concentration since we have not monochromatic light, but a wavelength distribution requiring an extension of the law obtained by integration over wavenumbers. At small concentration levels we find a near linear relationship while going towards higher concentration levels the function becomes asymptotic. It should be noted that  $\Delta T$  has to be known for a correct calibration and that for  $\Delta T = 0$  no absorption will be observed due to the fact that the absorption and emission cancel out.

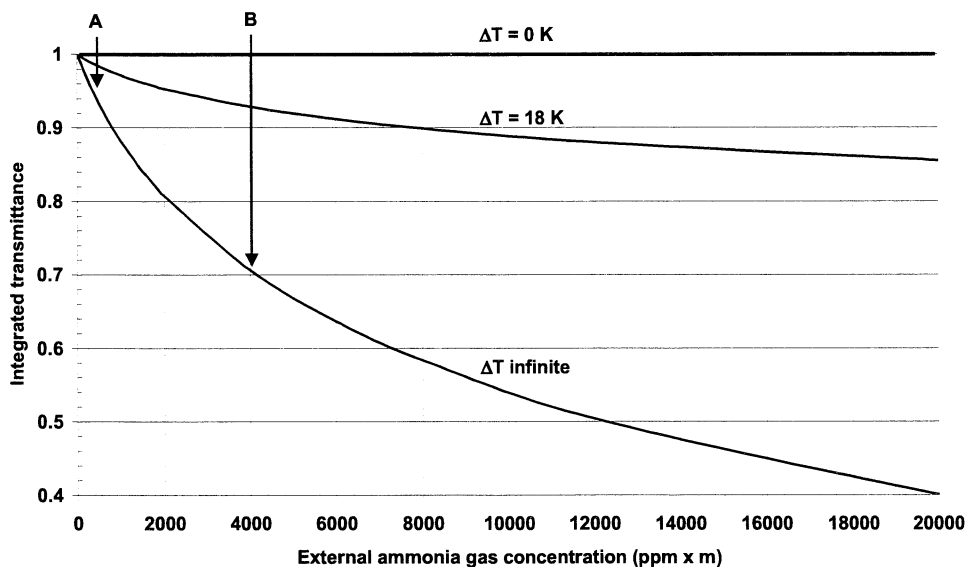


Fig. 4. Resulting calibrated ammonia gas concentration. Integrating the black envelopes in Fig. 3 corresponds to a transmittance value of one. Arrows A and B correspond to the integrated transmittance of the spectra in Fig. 3.

The theoretically calculated integrated transmittance values for different  $\Delta T$  were validated in a laboratory set-up. A  $8 \times 8 \text{ cm}^2$  aluminum plate, coated with a high-emissivity black paint and coupled to a Peltier element, was used as the background target. In front of this a 20 mm thick cell filled with 20000 ppm  $\times$  m ammonia gas was placed. The gas cell was held at a constant temperature of 294 K, while the temperature of the background target was varied. The results for 6 different values of  $\Delta T$  are displayed in Fig. 5 together with the theoretical curve, showing good agreement. Please note, that for negative values of  $\Delta T$ , a relative transmittance larger than 1 can be obtained. The temperature of the background surface was measured using a non-contact thermometer with laser aiming (Mikron® Instrument, model M101HT) with an accuracy of 1 K. The laboratory set-up was also used to determine the offset of the signal levels detected by the camera. This offset is mostly due to thermal emissions from the camera itself, the filter and the telescope. By plotting the detected

signal from the aluminum plate versus the band emittance from a blackbody at the measured temperature, the offset could be calculated.

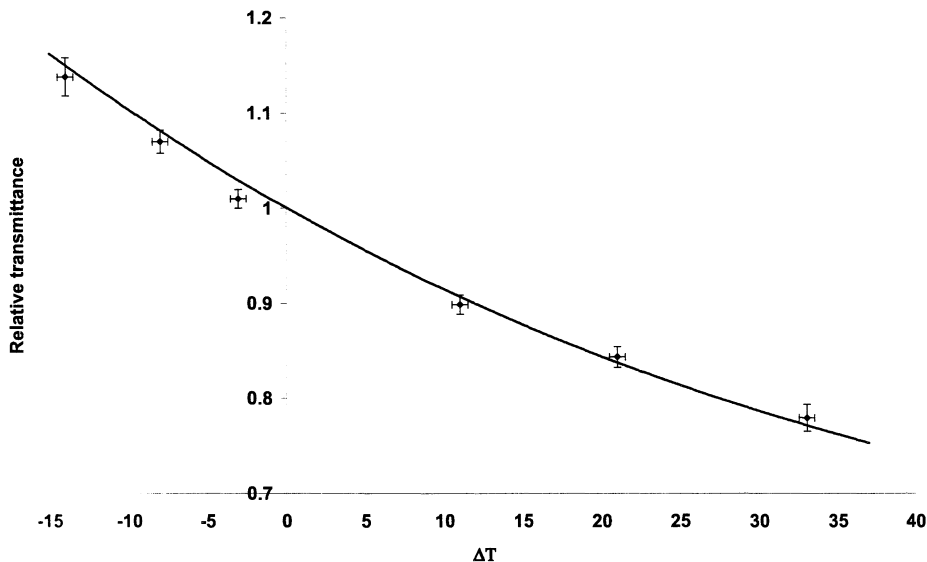


Fig. 5. Theoretically calculated relative transmittance through 20000 ppm  $\times$  m ammonia gas as a function of  $\Delta T = T_B - T_G$  with  $T_G = 294$  K. The results of an experimental verification are inserted with error bars in the figure.

### 3. Field experiment arrangements

Field experiments with the techniques developed were performed at the training station of the Malmö Fire Brigade. This site is located in southern Sweden and the measurements were performed in the month of September during mostly sunny conditions with an ambient air temperature of 18-21 °C and a relative humidity of 50%. Rather windy conditions with gusts up to 12 m/s prevailed. The measurement scenario and optical arrangements are illustrated in Fig. 6. A burnt-out rusty gas tank trailer was used as the target, forming a background with a surface temperature of 30-40 °C and an emissivity of 0.9. Gas bottles with ammonia, ethylene and methane were connected through long tubes attached to the trailer, simulating leaks. This set-up enabled controlled releases of one or several gases with different flow rates at or near the ambient air temperature.

The optical equipment was placed at a distance of 20 m from the trailer. Two images of the object were formed at the same time on the IR-sensitive camera with the Cassegrainian split-mirror telescope, with a total receiving area of  $2 \times 10$  cm<sup>2</sup>. The all-reflective optics of the telescope are comprised of two primary spherical aluminum mirrors and a secondary spherical aluminum mirror. The aluminum with MgF<sub>2</sub> coating has 96% reflectance over the spectral region of the camera. The positions of the primary mirrors are adjustable by fine threaded screws and focusing is done by translating the secondary mirror along the common optical axis. The Agema Thermovision 900 LW camera is using a Stirling-cooled MCT signal-processing-in-the-element (SPRITE) detector and a scanner which, line by line, scans the object. Timing circuits create an image of the line scans resulting in a resolution of 272  $\times$  136 pixels. The image is split by the Cassegrainian telescope into two regions of 136  $\times$  136 pixels each.

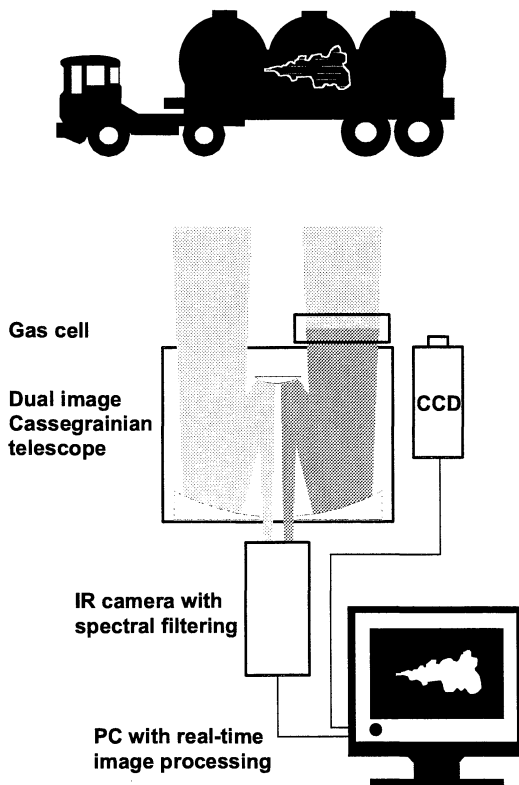


Fig. 6. Measurement scenario and optical arrangements.

The camera was equipped with suitable interference filters, used to isolate a small spectral region containing absorption features of the gas to be studied, as discussed earlier. The interference filters were mounted on a filter wheel in front of the detector inside the camera. In front of the telescope a 20 mm gas cell makes an additional filtering on one of the images. The gas cell was filled with an appropriate amount of a certain gas, making the cell essentially opaque at the stronger absorption lines. The two images thus produced can be used to extract a pure gas image and eliminate differences in the thermal background radiation as well as the interference by other gases or particles. A simultaneous recording of the scene in the visible spectral region was performed with a CCD camera mounted close to the telescope.

#### 4. Data processing and dynamic presentation

The IR camera is connected to a PC with an Imaging Technology frame grabber and a fast SCSI hard disk, allowing real-time recordings of 12-bit,  $272 \times 136$  pixels, at 15 frames/s. Image processing was performed on a PC with the Agema Irwin Research software and Matlab with the Image Processing Toolbox. After processing, the gas images could be overlaid on a normal image of the scene recorded with the CCD camera. The image processing was performed according to the following scheme:

- Two images A and B are captured at the same time using the Cassegrainian telescope, the IR camera and the frame grabber.  
A – image of the infrared scene from one of the telescope openings.  
B – image of the same scene with a gas cell in front of the other opening.
- The appropriate offset is subtracted from the images.
- An error (normalization) image, E, from the Cassegrainian telescope is created to handle imperfections such as asymmetrical vignetting, and stray-light from the two openings,  $E = A_0 / B_0$ . E is recorded with no gas present in the scene.

- The images are digitally overlapped by translation and optimization within a region of interest containing the gas, and subsequent image processing is restricted to this region.
- A gas-correlation image is calculated,  $G = (A / B) / E$ .
- On the result image,  $G$  a two-dimensional spatial median filter with a  $3 \times 3$  neighborhood averaging is performed to reduce the strong spike-like noise components (salt-and-pepper noise).
- The concentration levels (of ammonia) are set by threshold values obtained from simulations in GRAMS/32 and calculations with Excel as described in Sect. 2.1.
- Finally, the gas-correlation image is overlaid onto a visible image of the background and the resulting 15 frames/s movie is presented in Matlab.

For presentation purposes QuickTime movies are created in which we electronically zoom into the gas leakage and compress the gas-correlation resulting movies for fast access on Internet. An additional advantage of the normalization procedure described above is that gas concentration evaluations for the case of gas-correlation imaging can be handled in a similar way as described for the direct absorption case in Fig. 4 and 5.

## 5. Measurements and results

Results from the measurements at the Malmö Fire Brigade gas training station are presented in three PC image processing modes; all of them based on the two-dimensional spectroscopic gas-correlation image processing. In Sect. 5.1 binary images of ammonia, ethylene and methane overlaid on a visible image of the gas tanker background are presented. In Sect. 5.2 the ammonia gas is presented together with a color-scale of the concentration overlaid onto the visible background image, and in Sect. 5.3 the ammonia gas is shown together with the spectrally interfering ethylene gas, but the ammonia gas is distinguished from the ethylene gas and colored red with the gas-correlation image processing mode.

### 5.1 Visualization of ammonia, ethylene and methane leaks

To the left in Fig. 7 we show one or more gases (green colored) which absorb infrared light from the background in the spectral region defined by the filter, cell window material and camera response. The right-hand image is the result of gas-correlation image processing and we are thus certain that the gas is ammonia (red colored) and not interfering gases or varying background reflectances, emissivities or temperatures. The gas correlation cell, with a length of 20 mm, was filled with ammonia at a pressure of 1 atm., resulting in 20000 ppm  $\times$  meters with fully saturated spectral lines. It was not possible to detect external ammonia gas through the gas cell as expected.

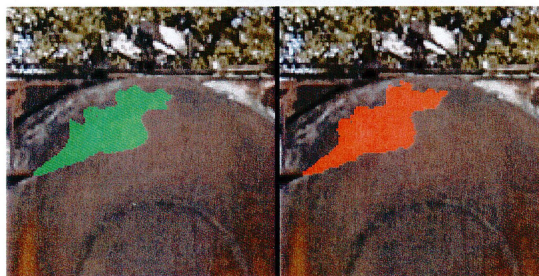


Fig. 7. (2 MB) Movie of an ammonia leak, left: by direct absorption and right: by gas-correlation. Binary gas images merged with visible images. Measurement conditions: Time 14:30, Air temperature 18 °C, Surface temperature 36 °C, Relative humidity 48 %, Gas flow 100 l/min, ZnSe gas cell with ammonia at 1 atm., Filter: Spectrogon LP9200.

In Fig. 8 we show leaking ethylene with the same method as for ammonia above. Again, we are certain that it is ethylene in the red-colored image due to gas correlation with an

ethylene gas cell. Notice that we have to somewhat sacrifice signal-to-noise ratio if we want to gain this information.

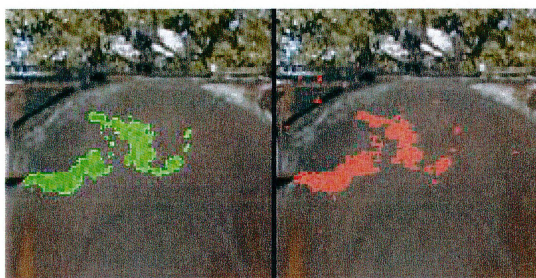


Fig. 8. (1.7 MB) Movie of an ethylene leak, left: by direct absorption and right: by gas correlation. Measurement conditions: Time 15:10, Air temperature 20 °C, Surface temperature 38 °C, Relative humidity 50 %, Gas flow 10 l/min, ZnSe gas cell with ethylene at 1 atm., Filter: Spectrogon LP9200

In Fig. 9 methane is visualized by direct absorption in the region from 7-8.5  $\mu\text{m}$  which is very sensitive to water vapor, see Fig. 12. Water vapor interferes spectrally with methane gas but this problem is alleviated by gas correlation; the gas itself is the perfect spectral filter for discrimination against other gases. The lower sensitivity of the camera in this region gives a slightly lower signal-to-noise ratio.



Fig. 9. (1.8 MB) Movie of a methane leak, left: by direct absorption and right: by gas correlation. Measurement conditions: Time 15:40, Air temperature 22 °C, Surface temperature 40 °C, Relative humidity 50 %, Gas flow 90 l/min,  $\text{CaF}_2$  gas cell with methane 1 atm., Filter: Spectrogon BBP7040-8500

## 5.2 Ammonia gas concentration visualized with a concentration color-scale

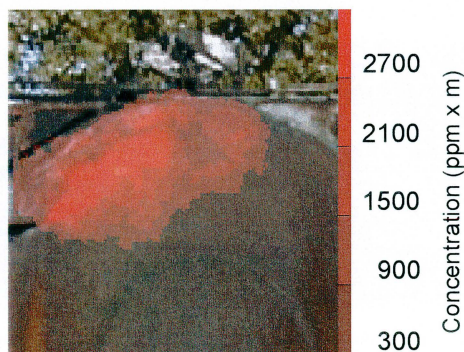


Fig. 10. (1.8 MB) Movie of an ammonia leak, color-scale concentration image. Measurement conditions: Time 14:30, Air temperature 18 °C, Surface temperature 36 °C, Relative humidity 48 %, Gas flow 10-100 l/min, ZnSe gas cell with ammonia at 1 atm., Filter: Spectrogon LP9200.

The spatial two-dimensional concentration  $\times$  length of ammonia, with an increasing flow from the first to the last image, is shown in Fig. 10. The concentration calculation was performed according to the method described in Sect. 2.1. This sequence of images was used to determine a detection limit of 200 ppm  $\times$  m in the present set-up.

### 5.3 Spectrally interfering ammonia and ethylene separated by gas correlation



Fig. 11. (1.9 MB) Simultaneous imaging of ammonia and ethylene leaks showing the isolation of the ammonia flow using the gas-correlation technique. Measurement conditions: Time 17:25, Air temperature 19.2 °C, Surface temperature 31.5 °C, Relative humidity 50 %, Ammonia gas flow 15 l/min, Ethylene gas flow 10 l/min, ZnSe gas cell with ammonia 1 atm., Filter: Spectrogon LP9200.

In Fig. 11 the result of gas-correlation with ammonia and spectrally interfering ethylene is shown. The image on the left hand shows both ammonia (upper gas) and ethylene (lower gas) leaks in direct absorption and the image on the right hand is the result after gas correlation, showing ammonia only. We observe that a slight cross talk from ethylene is visible in some of the resulting ammonia frames; this is due to a few interfering spectral lines; see Fig. 12.

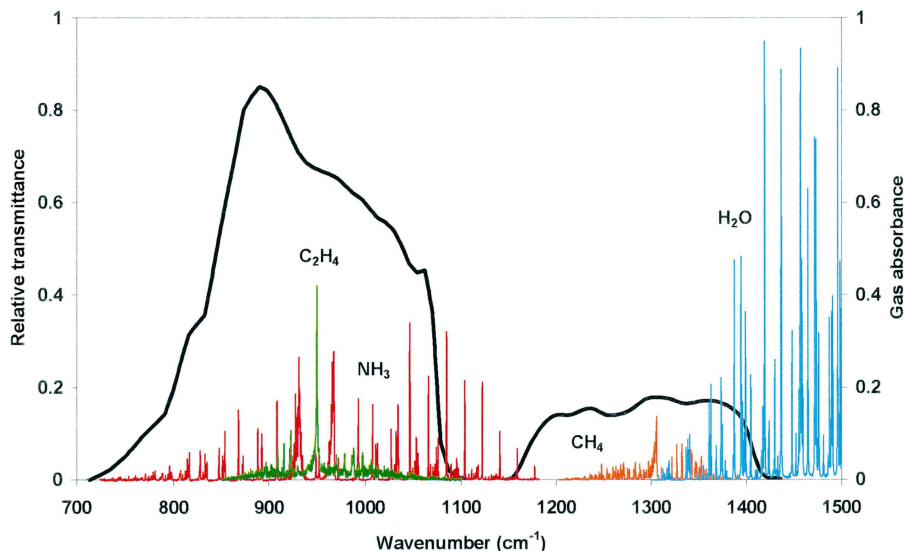


Fig. 12. Absorbance spectra of ammonia, ethylene and methane (200 ppm  $\times$  m). Water vapor is interfering with methane. IR camera system relative response (black curves).

## 6. Discussion and conclusions

Real-time gas visualization using IR thermal background radiation and gas correlation is demonstrated, as we believe, for the first time. Live sequences of ammonia, ethylene and methane leaks are shown and gas separation for spectrally overlapping species is demonstrated. As shown in the paper there is a possibility to quantify the emissions. However,

an accurate knowledge of the temperature difference between the gas and the background is then necessary. Calibrated measurements also put a higher demand on control of the camera and telescope temperatures. Present sensitivities are in the range of 200 ppm  $\times$  meters for ammonia ( $\Delta T = 18$  K) at a frame rate of 15 Hz, with an estimated sensitivity improvement of a factor 10 if moderate temporal and spatial averaging is performed. This detection limit is presently limited by imperfections in the telescope construction, resulting in image errors and varying offset problems. These effects could here be handled by recording an image without the gas present in the scene. With a better construction of the telescope, this procedure should not be necessary and the two sub-images, with and without the gas correlation cell, could be used to fully compensate for a varying background. Potentially, several gases could be monitored with a camera sensitive in the 8-14  $\mu\text{m}$  region. The emerging QWIP (Quantum Well Infrared Photon) detector with tailored spectral sensitivities will clearly strongly improve future performance. The techniques presented have considerable potential for real-time monitoring of pipelines, even by helicopters, since the two images are captured exactly simultaneously, effectively eliminating spurious effects due to motion. Since the techniques rely on a temperature difference between the air and background temperature, it is important to select suitable time intervals for the monitoring [11].

### **Acknowledgements**

The authors gratefully acknowledge interesting discussions with Sven-Åke Ljungberg, and the support of the Malmö Fire Brigade in performing the field experiments. Further, we are very grateful to Dr. Mats Kleverman of the Solid State Physics Division, LTH, for his kind help in performing the Fourier transform spectrometry recordings. This work was supported by the Swedish Space Board, the Swedish Engineering Sciences Research Council and the Knut and Alice Wallenberg Foundation.

III

# Gas visualization of industrial hydrocarbon emissions

J. Sandsten, H. Edner, and S. Svanberg  
Department of Physics, Lund Institute of Technology,  
P.O. Box 118, S-221 00 Lund, Sweden

## Abstract

Gases leaking from a polyethene plant and a cracker plant were visualized with the gas-correlation imaging technique. Ethene escaping from flares due to incomplete or erratic combustion was monitored. A leakage at a high-pressure reactor tank could be found and visualized by scanning the camera system over the industrial site. The image processing methods rely on the information from three simultaneously captured images. A direct and a gas-filtered infrared image are recorded with a split-mirror telescope through a joint band-pass filter. The resulting path-integrated gas concentration image, derived from the two infrared images, is combined with a visible image of the scene. The gas-correlation technique also has the potential to estimate the flux in the gas plume by combining a wind vector map, derived by cross-correlating the images in time, with a calibrated gas path-integrated concentration image. The principles of the technique are outlined and its potential discussed.

## 1. Introduction

Visualization of gases from industrial areas is of interest for many reasons. Hydrocarbon gas emissions are important for environmental considerations. Health and safety of the operating personnel at petrochemical plants are directly affected by gas emissions at the workplace. Monitoring of gas leaks is therefore of great importance in controlling and stopping gas outflow. Easily deployable surveillance techniques for assessing sites of accidents involving gas tankers or trains are desirable for safety considerations. We have developed a technique for the imaging of a certain gas employing IR cameras and gas filter correlation techniques [1]. Our first measurements were performed using a camera sensitive in the 3-5  $\mu\text{m}$  region. More recently, a camera sensitive in the 8-12  $\mu\text{m}$  region and a split-mirror Cassegrainian telescope has been employed, enabling passive gas imaging through absorption or emission of thermal radiation [2]. The present paper

illustrates gas visualization and leak detection at a polyethene producing petrochemical plant in Sweden. Specific gas visualization and quantification with a technique that relies on passive background radiation and elimination of problems with interfering gases, aerosol particles and varying background radiation have not existed until now. Two complementary techniques, based on lasers are the lidar- (light detection and ranging) and the bagi- (backscatter absorption gas imaging) techniques [3-5]. The lidar technique has been used to map cross-sections of the air downwind from industrial sites by vertical scanning a pulsed laser beam [6]. The lidar systems are based on sensitive and costly laser systems often placed in trucks on optical tables. The lidar technique is especially interesting for environmental protection authorities because of the possibility to ascribe a total flux to an industrial site of diffuse leaks. The bagi technique is based on a laser, which is spectrally tuned to a gas absorption line and synchronously scanned with an infrared sensitive camera. The method depends on diffusely backscattered light from a surface with an even reflectance behind the gas and the speckle noise in the images produced is of concern. The use of a high-power laser makes eye safety a problem when searching for real leaks in an industrial site. Both the lidar and the bagi techniques depend on lasers and are therefore not as flexible and viable as the new gas-correlation imaging technique.

## **2. Measurements**

Performing gas visualization at industrial sites places a number of demands on the monitoring system. The most important system characteristics, some of them may seem obvious, are a rugged and compact design, an easily moveable setup and an insensitivity to interference, such as from varying background emissivities and other gases including the frequently occurring water vapor. The precise location of a leak must also be registered in parallel with the detection of emitted gas. The gas of interest must be visualized at least at concentration levels prescribed by the regulating authorities. As an example, in the Swedish oil industry the operating personnel will immediately fit tight a hydrocarbon leak if its value is above 900 ppm (measured as a propane equivalent with a calibrated point monitoring instrument as close to the potential leak as possible). A leak between 100-900 ppm should be taken care of on a scheduled basis, and leaks below 100 ppm can be left without taking any measures. Finally, the measurements must not disturb the activities in the industrial site.

The detection system that solves the problems mentioned above is based on the passive two-dimensional gas-correlation principle. It consists of a newly developed split-mirror telescope, an infrared camera and a ccd camera used for taking visible images. The essential component in optical and spectroscopic gas correlation is the split-mirror telescope [7]. The telescope was designed and evaluated using a ray-tracing program [8] and it has enhanced the signal-to-noise ratio and improved the image quality of the real-time gas correlation movies compared to a former solution, which was based on a Cassegrainian telescope [9]. It takes less than 10 minutes to set the system up and start taking the first gas images. The distance to the objects is normally between 10 and 1000 meters. The infrared camera generates an image built up from 272 x 136 pixels making it well suited for the formation of two 136 x 136 pixels images at the same time [10]. Visible images are generated together with the gas images and used as a background to guide the eye and locate the leakage. The camera system made it possible for us to visualize ethene gas clouds and leakages from a polyethene plant and a cracker plant in Sweden. The system is shown in Fig. 1 in front of the cracker plant.



Fig. 1. The gas-correlation infrared camera system in front of a cracker plant.

The measurement positions could be chosen freely inside the site or outside the fence. A major feature of the passive gas-correlation imaging is the possibility to visualize and measure gas emissions from places difficult to access with other methods. A flare is exceedingly hard to monitor but an important contributor of hydrocarbons if the combustion is incomplete or erratic. The combustion of ethene should preferably always be visualized and optimized in the flare. During the flare measurements at the petrochemical plant the meteorological conditions were: varying wind speeds (mean value 4 m/s) and directions, air temperature 5 °C and the blue sky or clouds were providing the background. The detection limit of the passive gas-correlation method is strongly influenced by the temperature difference between the gas cloud of interest and the background [2]. We make the assumption that the ethene gas temperature quickly assumes the same temperature as the surrounding air. The gas reaches thermal equilibrium with the air downwind the flare exit by relaxation through vibrations and rotations in parts of a second. It should be noted, that it is necessary to measure sufficiently far downwind from an optically thick outlet, so that the plume becomes optically thin; in order to derive the concentration times length (path-integrated concentration) through the plume for flux evaluations. This is in practice a few meters from the flare exit. The projected wind vector is derived by cross-correlating the processed gas-correlation images in time. The image processing will be described in detail in section 4.

### **3. Results**

Flares are used to burn excess hydrocarbon gases, hydrogen and other gases. By directing the camera system to flares, we could visualize the flow of ethene that escapes from the flares. Two flares at the polyethene plant, LT1 and LT2, have a height of 40 m and in our measurements they were 340 m and 430 m from the camera system, respectively. A photograph of the flare LT1 is shown in Fig. 2(a). The result from the LT1 flare, after gas-correlation image processing and merging with a visible ccd image, is shown in Fig. 2(b). We could observe water vapor just above the exits with the naked eye and the ccd camera, as shown in Fig. 2(b).

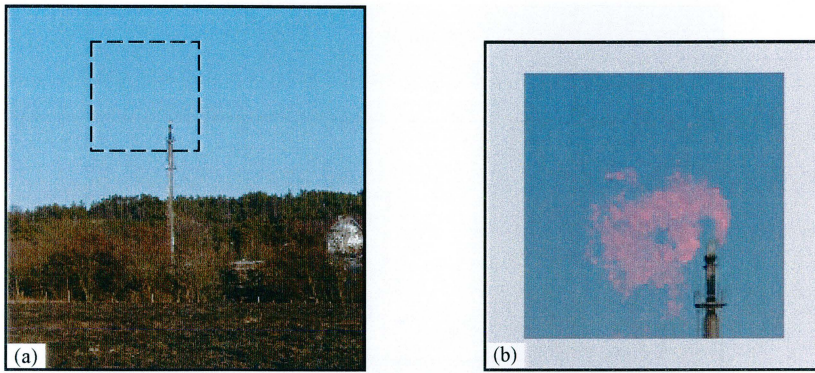


Fig. 2. (a) Flare LT1 at the polyethene plant. (b) Ethene gas cloud escaping from flare LT1 as visualized with the system.

The other flare, LT2, was burning ethene more effectively. Figure 3 shows three consecutive images with one second between each image from a sequence of 500 images (33 seconds).

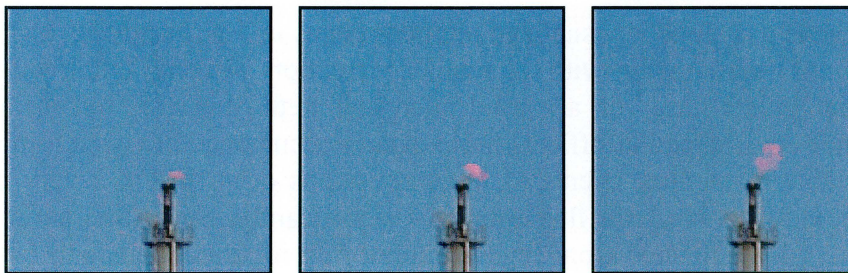


Fig. 3. More effective ethene combustion in flare LT2 as visualized with the system.

Thirty minutes after the image in Fig. 2. was captured, the high pressure (2300 bar) reactor tank safety valve released 1 – 2 tons of ethene in five minutes to the atmosphere. The gas cloud covered the industrial site for 15 minutes before it was blown away and diluted in air. A visible ccd image of the site is shown in Fig. 4.

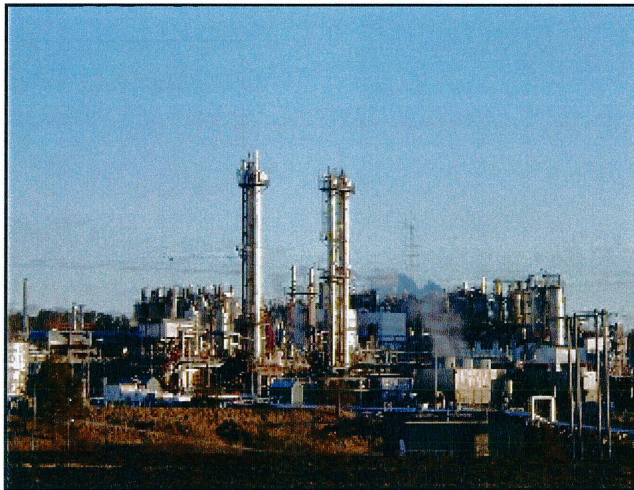


Fig. 4. Image of the polyethene plant taken from the same position as the flare measurements. The high pressure reactor is seen behind the gas purification site in the middle of the image.

The ethene gas cloud is visualized in three scenes in Fig. 5 and Fig. 6. These recordings were taken with a simpler detection system, employing an infrared camera based on a staring microbolometer detector. According to the chief environmental officer, these events occur once or twice a month. Being able to monitor events of large emissions occurring in a very short time could improve total flux estimates significantly. Spike-like emissions are often discriminated from regular monitoring measurements and labeled outliers, but the inclusion of such events is of great importance for controlling authorities. Visualizing such events has the strong pedagogical power of images and pinpoints environmental problems.

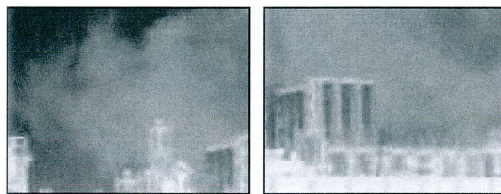


Fig. 5. Optically dense ethene gas cloud one minute after the safety valve release.

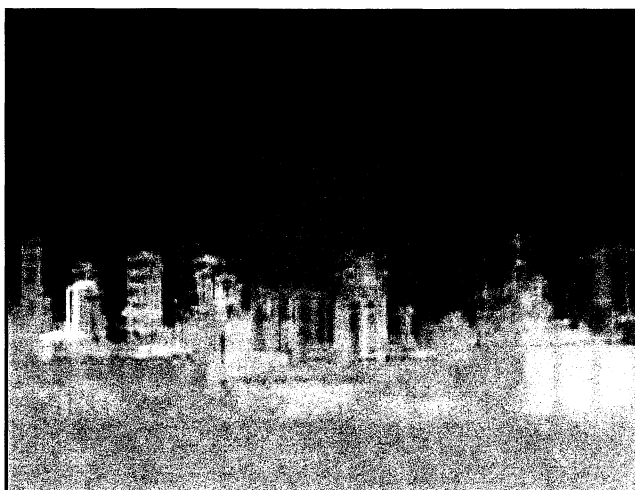


Fig. 6. Ethene gas cloud covering part of the industry five minutes after the high-pressure reactor safety valve release of 1 – 2 tons of ethene into the atmosphere.

So far, all the measurements were performed from outside the plant during the evening before the official measurement day. The next day we started measurements at the gas purification site and monitored the flares again. During that sample test, the flares did not burn any ethene or they were not fed with ethene. By sweeping the camera system over the polyethene plant, we could find an ethene leakage despite the presence of the interference from water vapor and other gases. This leak was taken care of immediately by the operating personnel. The leak was due to a sheaving valve in connection with the high-pressure reactor gas release the evening before. This leak is visualized in Fig. 7.



Fig. 7. By sweeping the camera system over the polyethylene plant, a leakage was found. A visible image and a sequence of gas images are shown. The gas-correlated images are merged with the zoomed visible image. The ethene gas leakage was taken care of immediately by the operating personnel.

Measurements were also performed on the cracker plant with the camera system placed outside the fence at the power-interlocking machine. The flare seen from this site is shown in Fig. 8. It was not clear, by the beforehand information from the chief environmental officer, whether the flares were burning ethene during the sample test, or some other gas, but the result clearly shows that no ethene escapes from the flares. This indicates that no ethene was fed to the flares. Otherwise, there would have been traces of ethene gas. The two light spots in the image, shown in Fig. 8(b), are the visible parts of the flame.

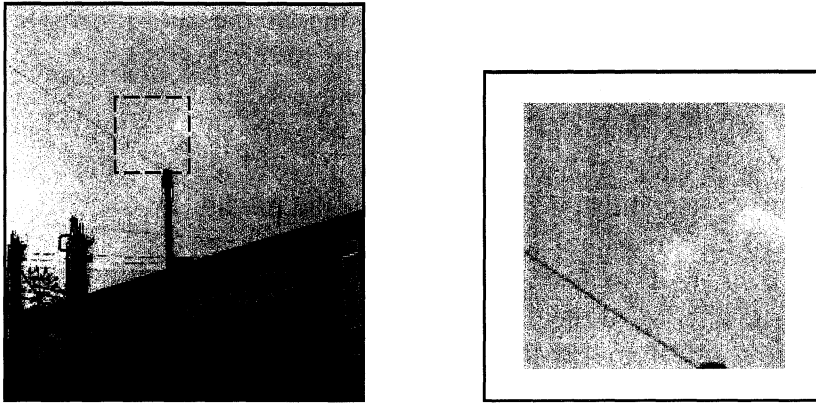


Fig. 8. A cracker flare with a visible flame is seen in the left frame. In the right frame, the flare is seen after gas correlation, showing no traces of ethene gas. The light spots are the visible flame parts.

At the next site, in close proximity to a small oil harbor, we used the camera system in both the absorption and the emission modes of operation. Flares were monitored in emission against clouds in the background sky and the hot cracker plant was used as the background in the gas absorption mode. Searching for leaks and fitting them tight is of interest from an economical point of view, because it can reduce valuable raw material spill, but it is also extremely interesting for the operating personnel, because of health and safety aspects. Further, the awakening environmental consciousness among the public cannot allow greenhouse gas emissions that could easily be visualized and eliminated.

#### **4. Gas-correlation telescope design and image processing**

In this section, we will describe the gas-correlation image processing in detail. The final images in the previous section will be dealt with and the derivation of the path-integrated concentration, the procedures for retrieving the wind vector and the flux calculations will be explained. Two image-processing strategies have been developed and they are selected depending on how we want to visualize the flowing gases. The first strategy is used when searching for leaks and the other one is used if there is a need for flux measurements. The reasons for dividing the image processing into two parts are that searching for specific gas leaks can be made in real-time, while the flux measurements involve cross-correlation of complete matrixes, which is time consuming and therefore is better suited for post processing. The image

generating system including the new design of the split-mirror telescope will also be evaluated and compared with the former system.

In earlier work on gas visualization, we have been using a Cassegrainian telescope [8]. The telescope consists of a primary spherical mirror divided into four separated parts and a secondary spherical mirror. This telescope is a classical Cassegrainian design except for the possibility to fine adjust the positions of four images. The design was found to cause a number of image errors, which are described in Ref. [7]. Here we will summarize the results from ray-tracing [9] of the Cassegrainian telescope and compare the design with the results from ray-tracing of the new Gas-Correlation Telescope (GCT), see Table 1.

**Table 1. Comparison of the two telescopes used for gas-correlation imaging.**

	<b>Cassegrainian Telescope</b>	<b>Gas-Correlation Telescope</b>
Primary mirror	Spherical	Off-axis parabolic
Secondary mirror	Spherical	Folded planar
Focal length (mm)	194	305
Reduction	1:1550	1:980
Opening diameters (mm)	43	43
<b>Ray-tracing results:</b>		
Spherical aberration coeff.	-1.84	0.006457
Spot size radius on axis ( $\mu\text{m}$ )	100	22

The Cassegrainian telescope is based on two spherical mirrors, which are used off-axis. The spherical aberration coefficient is therefore the largest aberration representing the transverse displacement in the paraxial image plane. With the new gas-correlation telescope design, a diffraction limited spot size radius five times smaller than the former Cassegrainian design was reached. This was accomplished by using off-axis parabolic mirrors and planar mirrors for motorized focusing and ray folding. A ray-trace of the GCT with an object of five meters height, placed 300 meters from the telescope results in the rays shown in Fig. 9, forming two simultaneous images of 5.1 mm height each.

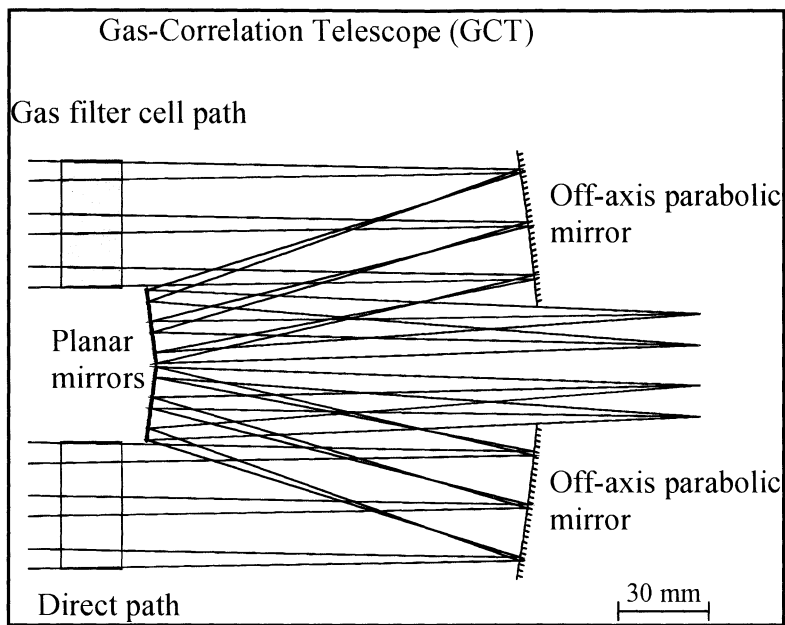


Fig. 9. Ray-tracing the gas-correlation telescope.

The new telescope design enabled us to find specific gas leaks in the industrial environment as reported in the results section before. The raw images belonging to the result image in Fig. 2, of the flare at LT1, are shown in Fig. 10. Both images are captured at the same time with the infrared camera [10] equipped with a bandpass filter; the left image in the figure is a direct infrared image of the flare and all the gases and water vapor that are escaping. The right image in Fig. 10 is an ethene gas-filtered image, showing the same objects as in the direct infrared image but no ethene. Notice the self-emission from the ethene in the gas cell, seen all over the image as a slight brightness increase.

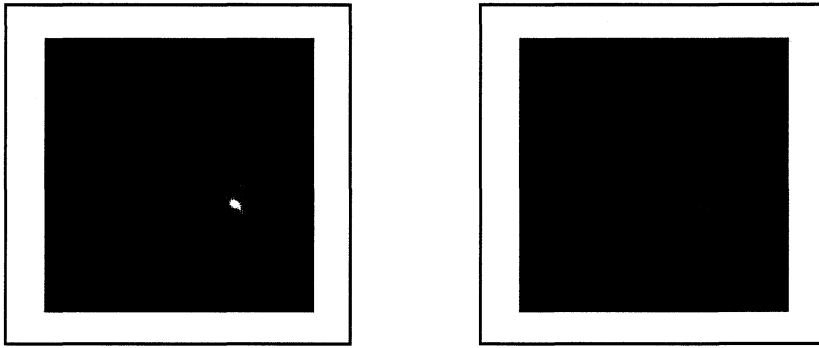


Fig. 10. Raw split-mirror image of the flare at LT1. The left part of the figure shows the infrared image of the flare and at the same time the ethene gas-filtered image is captured and shown to the right in the figure.

From the raw images, we subtract a background image that includes telescope and gas cell self-emission. This image is recorded against the sky background. The result is shown in Fig. 11. The next step in the image processing is to divide the infrared image with the ethene gas-filtered image. After that step we reduce the salt-and-pepper noise with median filtering and enhance the contrast by thresholding the image with respect to a residue of ethene that survives the division. The resulting ethene gas images are then merged with visible images and presented as a movie [11].

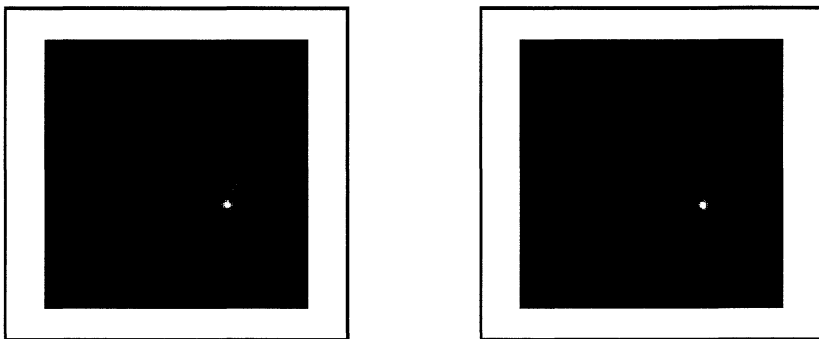


Fig. 11. Raw split-mirror image of the flare at LT1 with the background image removed.

The leak image as shown in Fig. 7 that was obtained as part of a sweep of the camera system field of view over the polyethene plant, was processed as the flare, except for a stronger thresholding, that yielded binary images. The gas is coded as one where it is sensed and zero everywhere else in the gas image.

At the cracker plant, the raw images belonging to the result image in Fig. 8, of the flare at the power-interlocking machine, are shown in Fig. 12. As before, both images are captured at the same time; the left image in the figure is a direct infrared image of the flare and all the gases and water vapor that are escaping. The right image in Fig. 12 is an ethene gas-filtered image, showing the same object as in the infrared image but no ethene. Notice the self-emission from the ethene in the gas cell, seen all over the image as a slight brightness increase.

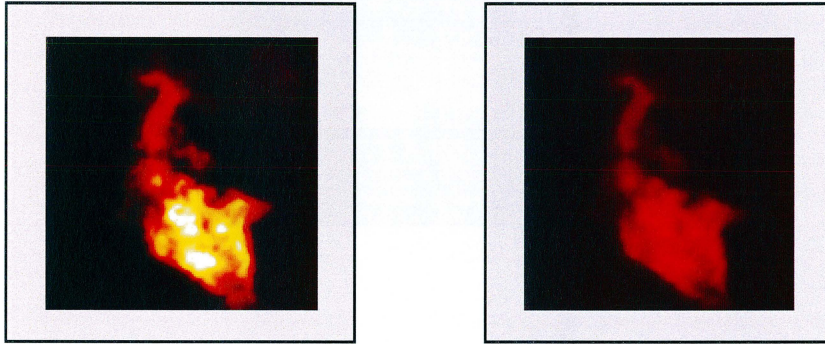


Fig. 12. Cracker plant flare; raw split-mirror images. The left part of the figure shows the direct infrared image of the flare and at the same time the ethene gas-filtered image is captured and shown to the right in the figure.

From the raw images, we subtract a background image. The result is shown in Fig. 13. The same image processing is used as for the flare at LT1 described above.

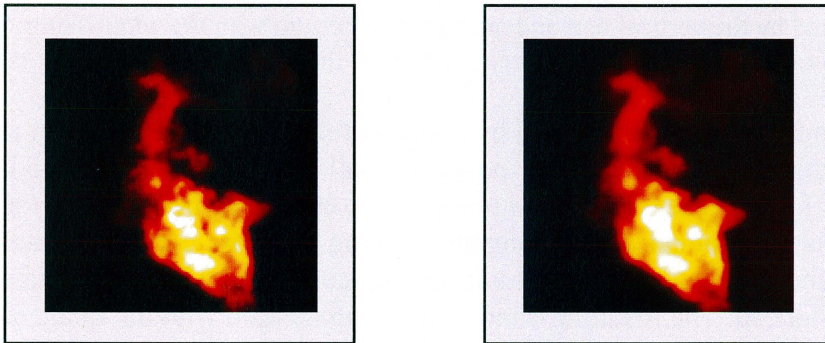


Fig. 13. Raw split-mirror image of the flare with the background image removed. In this case, the right image in the figure is corrected for ethene gas cell absorption. Notice that no ethene is escaping from the flare.

With a calibrated gas-correlated image as discussed in Ref. [2], the flux can be calculated using techniques described in Ref. [6]. The path-integrated concentration in Fig. 14(a) corresponding to the individual pixel values are summed in the column depicted by the vertical bar, shown in Fig. 14(b). The wind is blowing from the right in the image and downwind at the vertical bar, the gas cloud is optically thin.

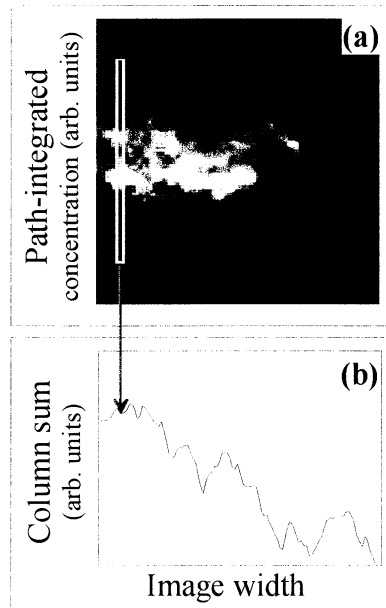


Fig. 14. (a) Gas-correlated ethene image. The concentration times the depth in the image corresponds to a pixel value in the calibrated image. (b) By summing the pixel values in the column downwind where the gas cloud is optically thin, depicted by the vertical bar, and multiplying the sum with the wind vector obtained from cross-correlating two gas images in time, the ethene flux can be estimated.

A wind vector map is derived by cross-correlating a small matrix in an image at time  $T_0$  with a corresponding small matrix in an image at a later time,  $T_1$ . The size of the small matrixes are chosen by maximizing the cross-correlation product. By creating and moving the cross-correlation matrixes over the complete images a resulting time-correlated wind vector map can be produced. The resulting wind vector map merged with the image at time  $T_0$  is shown in Fig. 15(c). A typical time interval,  $T_1 - T_0$ , has been 1/15 s.

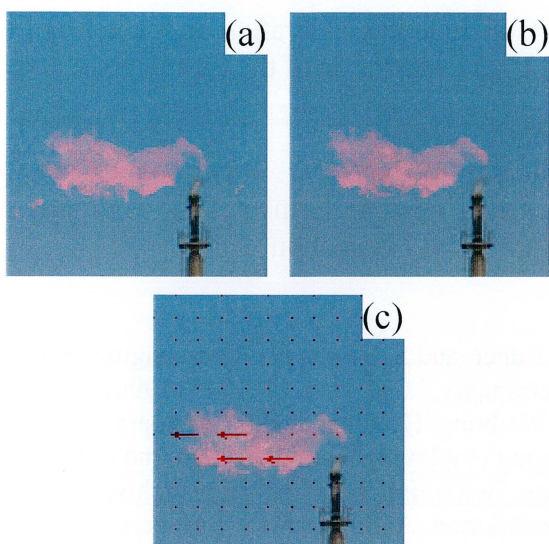


Fig. 15. (a) Gas-correlated ethene image at time  $T_0$ . (b) Gas-correlated ethene image at time  $T_1$ . (c) Wind vector map derived by cross-correlating the gas-correlated images at time  $T_0$  and  $T_1$ . The resolution of the vector map is determined by the size of the small cross-correlation matrixes.

The magnitude of the wind vectors in Fig. 15 (c) are varying from 6.6 m/s to 7.1 m/s. The leftmost arrow in Fig. 15(c) multiplied with an ethene calibrated pixel value in Fig 14(a) yields the flux of ethene from the flare.

## 5. Discussion

We have showed that the gas-correlation imaging technique is well suited for industrial leakage detection and visualization. The imaging methods described can also be used for flux determinations. Incomplete flare combustion can be monitored in real-time using the emission mode. The main advantage of the passive gas-correlation method is the simultaneous capture of two images, which are divided, yielding a result image free from interfering gases and varying background conditions. A great advantage over active methods is that there is no need for a costly and sensitive laser or spectrometer. The gas-correlation cell acts as a perfectly matched specific gas filter.

Further planned measurements include the study of the gas distribution of ethene leaking from a petrochemical plant, where comparisons with a long-path solar tracking FTIR spectrometer will be made. The distance from the camera system to the petrochemical plant can be chosen between 10-1000

m. Future prospects include the calibration of several hydrocarbon gases as described in Ref. [2] and adaptation of the technique to other applications.

### Acknowledgements

The authors would like to thank Mr. Jonny Andersson for his kind help when the measurements were performed. This work was supported by the Knut and Alice Wallenberg Foundation.

### References

1. J. Sandsten, H. Edner, and S. Svanberg, "Gas imaging by infrared gas-correlation spectrometry," *Opt. Lett.* **21**, 1945 (1996)
2. J. Sandsten, P. Weibring, H. Edner, and S. Svanberg, "Real-time gas-correlation imaging employing thermal background radiation," *Optics Express* **6**, 92 (2000); <http://www.opticsexpress.org/oearchive/source/19020.htm>
3. H. Edner, K. Fredriksson, A. Sunesson, S. Svanberg, L. Unéus, and W. Wendt, "Mobile remote sensing system for atmospheric monitoring," *Appl. Opt.* **26**, 4330 (1987).
4. H. Edner, S. Svanberg, L. Unéus, and W. Wendt, "Gas-correlation lidar," *Opt. Lett.* **9**, 493 (1984).
5. T. J. Kulp, P Powers, R. Kennedy, and U-B. Goers, "Development of a pulsed backscatter-absorption gas-imaging system and its application to the visualization of natural gas leaks," *Appl. Opt.* **37**, 3912 (1998).
6. P. Weibring, M. Andersson, H. Edner, and S. Svanberg, "Remote monitoring of industrial emissions by combination of lidar and plume velocity measurements," *Appl. Phys B* **66**, 383 (1998).
7. J. Sandsten, "Development of infrared spectroscopy techniques for environmental monitoring," *Lund Reports on Atomic Physics* **LRAP-257**, 2000.
8. P. S. Andersson, S. Montán, and S. Svanberg, "Multi-spectral system for medical fluorescence imaging," *IEEE J. Quant. Electr.* **QE-23**, 1798 (1987)
9. OSLO, Optics Software for Layout and Optimization, Ver 5.4, Sinclair Optics 2000.
10. Camera system specifications; Detector: MCT Sprite Stirling, 4–13  $\mu\text{m}$ , NE $\Delta$ T = 80 mK, Filterwheel with 5 positions; Visualised gases: Methane, Ethene, Ammonia, Nitrous Oxide; Ammonia: Detection limit 30 ppm  $\times$  m at  $\Delta$ T = 18 K with split-image telescope (present), Range and resolution: 10-1000 meters, 136  $\times$  136 pixels gas image combined with high resolution visible image; Frame rate: 15 images/s.
11. <http://www-atom.fysik.lth.se/JonasSandsten/GasVisualisation.htm>

IV

# Simultaneous detection of methane, oxygen and water vapour utilising near-infrared diode lasers in conjunction with difference-frequency generation

Ulf Gustafsson, Jonas Sandsten, Sune Svanberg  
Department of Physics, Lund Institute of Technology  
P.O. Box 118, SE-221 00 Lund, Sweden

## Abstract

An all-diode laser based spectrometer is used for the simultaneous detection of methane, oxygen and water vapour. This is accomplished using a 760 nm diode laser and a 980 nm diode laser in conjunction with difference-frequency generation to 3.4  $\mu\text{m}$  in a periodically poled lithium niobate crystal. Each of the output wavelengths is resonant with one of the molecular species. Simultaneous recordings over a 15 m open path of laboratory air are demonstrated. The recording scheme shows the wide applicability of a diode-laser-based difference-frequency spectrometer for the detection of molecular species in different wavelength ranges. By increasing the frequency of the 760 nm diode laser and decreasing the frequency of the 980 nm diode laser, a maximum continuous tuning range in the mid-infrared of 3.6  $\text{cm}^{-1}$  is achieved. This enables the recording of several methane lines at atmospheric pressure. Pressure dependence studies of methane lineshapes are also performed in an absorption cell. An indoor air methane background level of 3 ppm is measured. The signal-to-noise ratio in the recorded methane spectra indicate that sub-ppm detection of methane at atmospheric pressure is feasible.

PACS: 42.55.Px; 42.62.Fi; 42.65.Ky

Laser absorption spectroscopy is a powerful technique for fast and sensitive detection of many gases in e.g. atmospheric monitoring, process control, and combustion diagnostics. The technique has been widely employed in the mid-infrared spectral region (2-15  $\mu\text{m}$ ), where numerous species of interest have strong fundamental vibrational absorption bands, and in the near-infrared region (0.6-2  $\mu\text{m}$ ), where weaker overtone and combination bands occur. Available laser sources in the mid-infrared region, e.g. lead-salt diode lasers, colour centre lasers, and CO or CO<sub>2</sub> lasers, each suffer from various practical drawbacks such as the need for cryogenic cooling, limited tuning range, poor amplitude and frequency stability, large size, high cost or high power consumption. The promising and newly developed but not yet commercially available quantum-cascade lasers have been used in spectroscopic investigations in the infrared [1-3] but continuous-wave operation requires cryogenic cooling and rather high supply voltages. In the near-

infrared region, on the other hand, diode laser technology offers several hundred milliwatts of narrow-band tuneable radiation at room temperature from small and low-cost devices. Using these near-infrared diode lasers and/or compact high-power diode-pumped solid-state lasers, great efforts have been made during the last years in developing difference-frequency generation (DFG) in non-linear materials for trace gas detection using the mid-infrared absorption bands [4-13].

All DFG implementations have so far only focused on the spectroscopic use of the generated mid-infrared radiation, disregarding the possibility of also using the generating laser wavelengths for probing the absorption bands in the near-infrared region. In the present study we explore simultaneous detection of atmospheric oxygen at 760 nm, water vapour at 980 nm and methane at 3.4  $\mu\text{m}$  using near-infrared lasers in conjunction with difference-frequency mixing in a periodically poled lithium niobate (PPLN) crystal. Such simultaneous detection of interacting species is frequently of great interest, e.g. in connection with combustion. Certain important molecules, such as oxygen can be detected in the near-infrared region but do not have strong mid-infrared absorption.

Actually, a similar use of coincidences of excitation spectra occurring in sum-frequency mixing of pulsed dye laser radiation has been used to simultaneously induce fluorescence in the important flame species OH, NO and O (two-photon excitation) [14] and in  $\text{HN}_3$ , OH, and NO [15]. More cumbersome, simultaneous  $\text{O}_2$ ,  $\text{H}_2\text{O}$  and temperature measurements have been performed by individually scanning three different near-infrared diode lasers [16], just as simultaneous flame fluorescence imaging of  $\text{C}_2$  and OH could be achieved with independent laser systems [17]. Alternatively, simultaneous fluorescence detection of flame species can be achieved when absorption lines are inter-mingled in a certain spectral region, such as for OH, NH, CH and CN around 312.2 nm [18]. Similarly, in the mid-infrared region, where difference-frequency mixing has been used for absorption measurements,  $\text{CH}_4$  and  $\text{H}_2\text{O}$  could be detected around 3.4  $\mu\text{m}$  [8,11],  $\text{CH}_4$  and  $\text{H}_2\text{CO}$  around 3.5  $\mu\text{m}$  [10],  $\text{CO}_2$  and  $\text{N}_2\text{O}$  around 4.4  $\mu\text{m}$  [9], or CO and  $\text{H}_2\text{O}$  around 4.8  $\mu\text{m}$  [12].

## 1 Experimental set-up

Our experimental set-up is schematically illustrated in Fig. 1. The two Fabry-Perot type diode lasers (Laser Components Specdilas F760 and Power Technology LD1313), operating around 760 nm and 980 nm and having a maximum output power of 55 mW and 200 mW, respectively, are placed in thermoelectrically cooled mounts. Temperature and current are controlled by low-noise diode laser drivers (Melles Griot 06DLD103). Coarse wavelength tuning of the diode lasers is accomplished by changing the temperature around the diode laser capsules between 10°C and 40°C, resulting in a tuning range of about 5 nm for the 760 nm diode laser and of 8 nm for the 980 nm diode laser. Fine tuning is accomplished by changing the diode laser currents. Wavelength scanning is made by adding a 110-Hz current ramp (Hewlett-Packard 33120A) to the operating current of one or both of the two diode lasers.

The vertically polarised diode laser outputs are first collimated by anti-reflection coated moulded glass aspherical lenses (Geltech C230TM-B), and the elliptical beam profiles are then made circular by two anamorphic prism pairs (Melles Griot 06GPA004). The two collimated and circular beams are spatially overlapped in a dichroic beamsplitter (Melles Griot 88NPDC875) and focused by an 8.5-cm focal length achromatic lens into the PPLN crystal (Crystal Technologies 97-02355-01). The focusing into the crystal was simulated with a ray-tracing program (Sinclair Optics OSLO) to choose an optimal lens. The 19-mm long and 0.5-mm thick PPLN crystal without antireflection coating has 10 grating periods, each 1-mm wide, between 18.6  $\mu\text{m}$  and 20.4  $\mu\text{m}$  in 0.2  $\mu\text{m}$  increments. A crystal oven (Super Optronics OTC-PPLN-20) ensures stable temperature of the PPLN crystal and fine tuning of the grating period for proper phasematching.

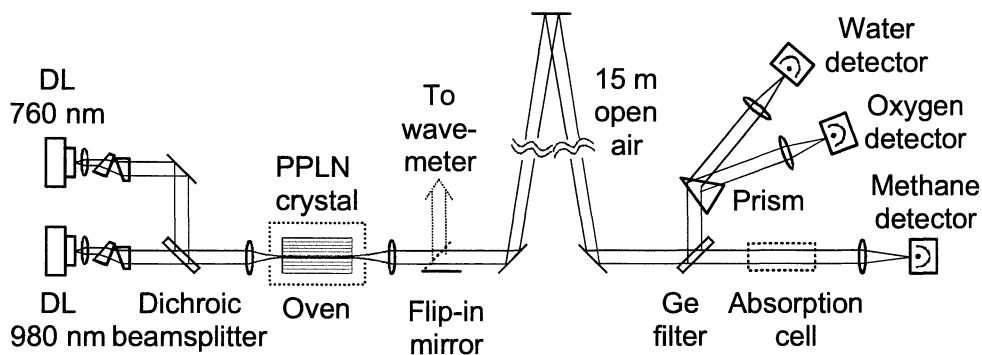


**Fig. 1** Experimental set-up for simultaneous ambient air monitoring of  $\text{O}_2$ ,  $\text{H}_2\text{O}$  and  $\text{CH}_4$ .

After the PPLN crystal, the two near-infrared beams and the generated mid-infrared beam are collimated by a 10-cm focal length  $\text{CaF}_2$  lens, and then transmitted through approximately 15 m of laboratory air in a common open path. An anti-reflection coated germanium filter is used as a beamsplitter, to reflect the near-infrared radiation and transmit the mid-infrared radiation. A  $\text{CaF}_2$  lens with a focal length of 10 cm focuses the mid-infrared beam onto a thermoelectrically cooled  $\text{HgCdZnTe}$  detector (Boston Electronics PDI-2TE-5) with an active area of 1  $\text{mm}^2$  and an immersed focusing lens. Combining an external focusing lens and a detector with an immersed lens simplifies the positioning of the small-area detector. A glass prism separates the two near-infrared wavelengths, and the intensities are detected by two pin photodiodes (Hamamatsu S-5821). The mid-infrared beam is in some of the experiments directed through a 10-cm long absorption cell with wedged  $\text{CaF}_2$  windows for high-resolution measurements at low pressures and studies of pressure broadening.

The detected signals are amplified and low-pass filtered at 30 kHz in low-noise preamplifiers (Stanford SRS560) and viewed in real-time on two-channel digitising

oscilloscopes (Tektronix TDS520B). The data are then transferred to a computer for processing and evaluation. A germanium etalon with a free spectral range of  $0.05\text{ cm}^{-1}$  can be inserted in the mid-infrared beam for relative frequency calibration, and a glass etalon with a free spectral range of  $0.08\text{ cm}^{-1}$  can likewise be used for the near-infrared beams. A flip-in mirror is used to redirect the two diode laser beams to a wavemeter (Burleigh WA-4500) for precise measurements of the diode laser wavelengths at different temperature and current settings.

No optical isolators are used in the experiments. Instead, all optics are placed with a small angle to the laser beams to avoid optical feedback. Especially important is to angle (1 to 2 degrees is sufficient) the PPLN crystal, since placing it exactly perpendicular to the input beams resulted in severe optical feedback to both diode lasers. Another important factor is the immersed lens on the mid-infrared detector. Tests using a detector without an immersed lens, also showed significant instabilities in the output spectra of the two diode lasers. The tilting scheme probably means that we have a somewhat less than optimum conversion efficiency in the PPLN crystal due to a slight beam walk-off, but it also has the added benefit of reducing etalon effects, often encountered in infrared absorption experiments, to a minimum.

The simplest and most often used tuning method in the mid-infrared utilising difference-frequency generation is achieved by changing the wavelength of one laser, while the wavelength of the other laser is fixed. The tuning range in the mid-infrared is then limited by the maximum tuning range of only one laser. Alternatively, both lasers can be tuned synchronously, resulting in a very large tuning range in the mid-infrared. By temperature tuning of the two near-infrared diode lasers a theoretical mid-infrared tuning range of about  $170\text{ cm}^{-1}$  is possible (from  $2895\text{ cm}^{-1}$  to  $3065\text{ cm}^{-1}$ ). Due to the mode jump behaviour of all Fabry-Perot type diode lasers some regions will not be accessible. We have investigated some regions in this range, and once a region of interest was established by temperature tuning, we applied the finer and much faster current tuning. In the experiments we use both of the near-infrared diode lasers for molecular spectroscopy and therefore they are driven by current ramps. Depending on the relative scan directions a long or a short mid-infrared scan can be achieved. By increasing the frequency of the high-frequency diode laser (760 nm) with a negative current ramp and decreasing the frequency of the low-frequency diode laser (980 nm) with a positive current ramp, a maximum continuous tuning range in mid-infrared of  $3.6\text{ cm}^{-1}$  has been achieved. A recording of the germanium-etalon fringes during such a scan is shown in Fig. 2. By changing scan directions, very short frequency scans are possible, and in principle, it is also possible to fix the mid-infrared frequency.

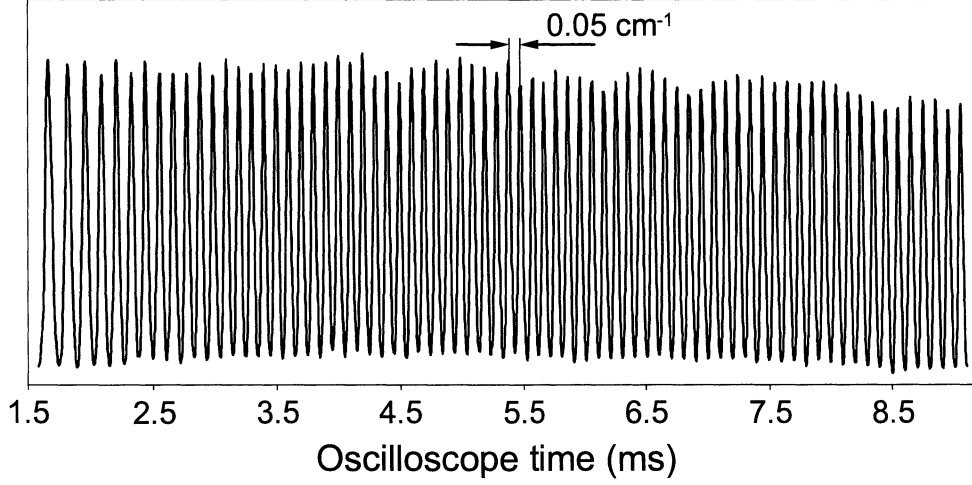


**Fig. 2** Ge etalon fringes around  $3.4 \mu\text{m}$  corresponding to a continuous tuning range of  $3.6 \text{ cm}^{-1}$  (72 fringes).

With near-infrared input powers of  $P_1 = 45 \text{ mW}$  and  $P_2 = 195 \text{ mW}$  at  $760 \text{ nm}$  and  $980 \text{ nm}$ , respectively, a maximum mid-infrared power of about  $9 \mu\text{W}$  at  $3.4 \mu\text{m}$  was generated. From the theory of difference-frequency mixing of focused Gaussian beams, the mid-infrared power can be expressed by [19]

$$P_3 = \frac{4\omega_3 d_{\text{eff}}^2 l}{\pi \epsilon_0 c n_1 n_2 n_3 (k_1^{-1} + k_2^{-1})} h\left(\frac{k_2}{k_1}, \frac{l}{b}\right) T P_1 P_2, \quad (1)$$

where

$$h(\mu, \xi) = \frac{1}{2\xi} \int_{-\xi}^{\xi} d\tau \int_0^{\xi} d\tau' \frac{1 + \tau\tau'}{(1 + \tau\tau')^2 + \left(\frac{1 + \mu^2}{1 - \mu^2}\right)^2 (\tau - \tau')^2}. \quad (2)$$

Here the subscripts  $i = 1, 2$  and  $3$  refer to the beams at  $760 \text{ nm}$ ,  $980 \text{ nm}$  and  $3.4 \mu\text{m}$ , respectively,  $n_i$  are the refractive indices of the PPLN crystal,  $P_i$  are the powers,  $k_i$  are the wave vectors,  $\omega_i$  are the angular frequencies,  $d_{\text{eff}} = (2/\pi) \times 27 \text{ pm/V}$  is the effective non-linear coefficient,  $l$  is the crystal length,  $b = 10 \text{ mm}$  is the confocal parameter of the two mode-matched input beams,  $T = 65 \%$  accounts for the reflection losses at the crystal input and output facets,  $\mu$  is the ratio of the input wave vectors ( $k_2/k_1$ ),  $\xi$  is the ratio of the crystal length and the confocal parameter,  $c$  is the speed of light and  $\epsilon_0$  is the permittivity of free space. Inserting our experimental values, we calculate a theoretical mid-infrared power of  $P_3 = 11.8$

$\mu\text{W}$ . The deviation between measured and calculated mid-infrared powers can most likely be ascribed to our inclination of the PPLN crystal.

## 2 Spectroscopic studies

Studies of the absorption spectrum of methane were performed with the generated mid-infrared beam passing through the 10 cm absorption cell. Recordings of a methane line from the P-branch of the  $\nu_3$  band at  $2927.075\text{ cm}^{-1}$  are shown in Fig. 3 for 3.5 mbar of pure methane in a total pressure of 5 mbar and then this methane concentration is successively diluted by air up to 800 mbar. In these recordings only the 760 nm diode laser was scanned. We observe a line broadening from 390 MHz to 2.4 GHz, corresponding to a pressure broadening coefficient of 2.6 MHz/mbar, in good agreement with previous results [20]. The laser system linewidth was estimated to 280 MHz with a  $\text{CH}_4$  Doppler linewidth of 270 MHz and the observed lowest linewidth of 390 MHz. We note that a very good signal-to-noise ratio is achievable, allowing sensitive trace-gas detection at low pressures. At atmospheric pressure the lines broaden and overlap, and it is impossible to distinguish the weak transitions. In particular, at low pressures it is possible to observe the minor isotopic species  $^{13}\text{CH}_4$  in the presence of the most abundant  $^{12}\text{CH}_4$  isotope (mixing ratio 1:100) as illustrated in Fig. 4. The mixing ratio is not given directly by the observed intensity relation, since the studied lines do not originate from the same energy levels, but in principle, knowing the relative oscillator strength it is possible to deduce the exact mixing ratio.

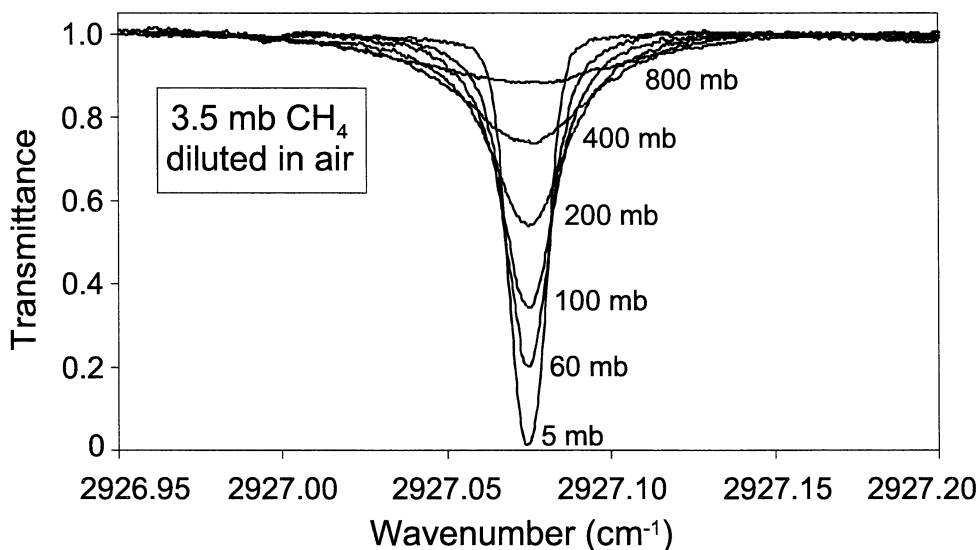


**Fig. 3** Methane spectrum as a function of pressure at  $3.42\ \mu\text{m}$ . The recordings are 500 scan averages, corresponding to a total sampling time of 4.5 sec for each curve.

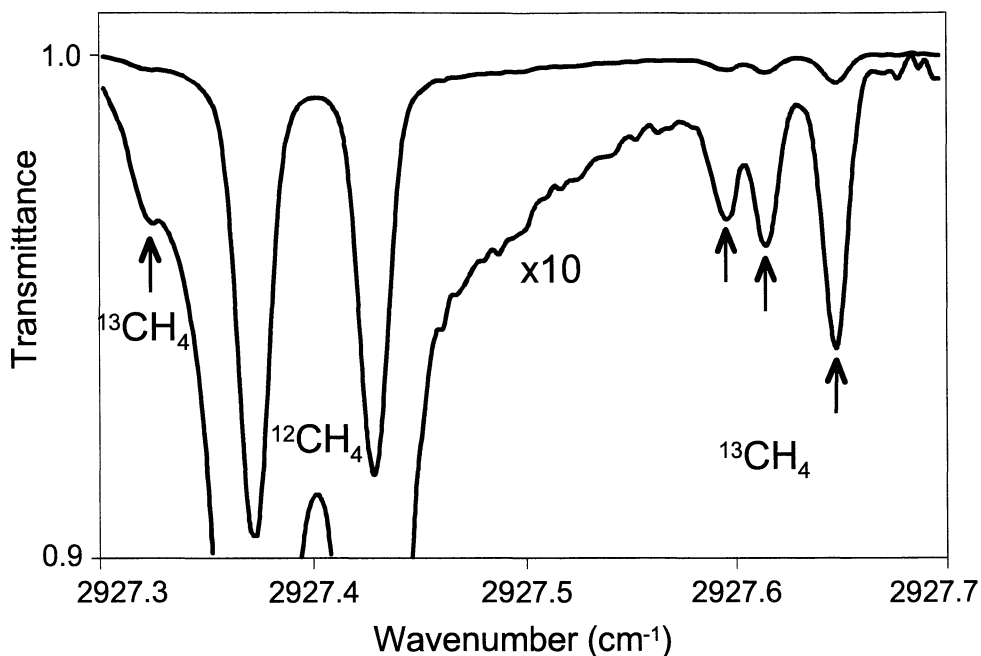


**Fig. 4** Low-pressure recording of methane gas exhibiting the low abundance species  $^{13}\text{CH}_4$  in the presence of the normal  $^{12}\text{CH}_4$  isotope.

After this demonstration of DFG spectroscopy we want to focus on the main theme of this work, namely the simultaneous detection of  $\text{O}_2$ ,  $\text{H}_2\text{O}$  and  $\text{CH}_4$ . Simultaneous recordings of the three species are shown in Fig. 5 for the 15 meter open air pathlength in the laboratory, together with computed spectra from the HITRAN molecular spectroscopic database [20]. The figure shows the single  $\text{O}_2$  A-band line, R7Q8, the single  $\text{H}_2\text{O}$   $5_{33} \leftarrow 6_{34}$  line in the  $\nu_1+2\nu_2+\nu_3$  water band, and a portion of the  $\text{CH}_4$  P-branch of the fundamental  $\nu_3$  methane band. By recording the whole oxygen and water profiles, and by scanning the frequency of the two diode lasers in opposite directions, a total frequency scan of  $3.6 \text{ cm}^{-1}$  is obtained in the mid-infrared. We choose to show  $1.8 \text{ cm}^{-1}$  of the scanned region where methane has prominent absorption lines. One can observe that the atmospheric pressure methane experimental and theoretical curve show some deviations not present in the low-pressure short-pathlength data. We conclude that the deviations can then not be due to some spurious laser mode running. The residual non-methane spectrum is most likely due to a low concentration of some interfering non-identified indoor environment hydrocarbon. We do not believe that the deviations are due to etalon fringes, since the structure is insensitive to small adjustments of the optical components, and fringes were ascertained to be absent in independent measurements.

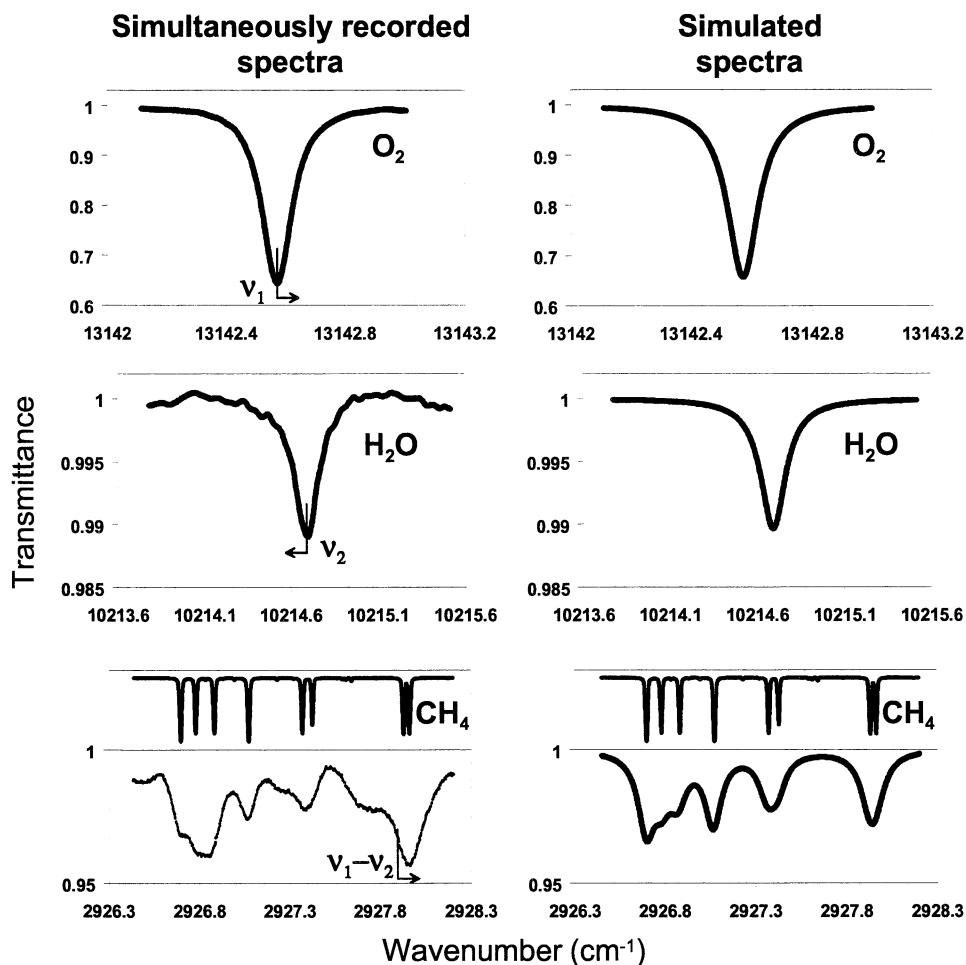


**Fig. 5** Simultaneous recordings of oxygen, water vapour and methane in a 15 m atmospheric path and corresponding spectral simulations based on HITRAN. Recording time is 4.5 sec. Scan directions in the individual laser sweeps and for the difference-frequency recording are indicated. Low-pressure, high-resolution spectra are included in the methane data.

$\text{CH}_4$  has an outdoor background atmospheric abundance of 1.7 ppm, and a somewhat higher concentration in the indoor air is expected. By fitting non-interfering experimental methane lines with Lorentzian line shapes, we have deduced that the typical methane background concentration in our laboratory is 3 ppm. With an observed signal-to-noise ratio (SNR) of about 20 in our recorded spectra at atmospheric pressure, we conclude that sensitivity in the 150 ppb range is achievable. The SNR was calculated as the ratio of the absorption peak value and

the peak-to-peak value of the noise. During our measurements the relative humidity of the air was fairly constant, ranging from 35 % to 45 %. On the day of the recording in Fig. 5, the relative humidity was measured to 40% with a hygrometer (equivalent to 11300 ppm H<sub>2</sub>O). According to the observed SNR of 40, the detection limit for H<sub>2</sub>O is 280 ppm. The normal O<sub>2</sub> concentration of 21% was measured and, as expected, this O<sub>2</sub> concentration value does not change at all from one day to another. The SNR in the O<sub>2</sub> recording was approximately 1300, indicating a detection limit of 170 ppm.

As an example of recordings, relevant to, e.g., the working environment, a 15 minute sequence of concentration determinations is shown in Fig. 6, exhibiting the response to the release of methane from a gas tank. The close-lying CH<sub>4</sub> transitions at 2928 cm<sup>-1</sup> shown to the right in the spectral recordings of Fig. 5 were used. Raw data from recordings of the pressure-broadened single-peak feature are shown as insets in the figure (0.9 sec. integration time). We note that the methane concentration is reduced to its background level after approximately 15 minutes. The structure occurring at 2 minutes was due to one of the authors walking around in the room inducing turbulent mixing.

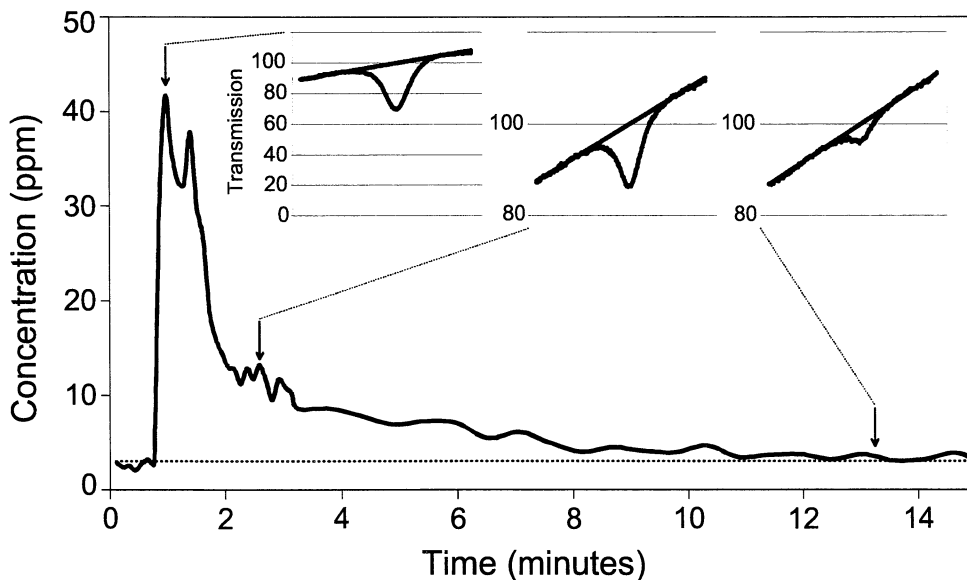


**Fig. 6** Monitoring of indoor methane concentration following the release of a small amount of gas from a tank. The measurement was performed over a 15 m pathlength. Raw data spectral recordings are shown as insets in the figure.

### 3 Conclusions

We have used two near-infrared diode lasers and difference-frequency generation in a periodically poled lithium niobate crystal for simultaneous detection of oxygen at 760 nm, water vapour at 980 nm, and methane at 3.4  $\mu\text{m}$ . This is accomplished by probing each molecular species by the two near-infrared wavelengths and the generated mid-infrared wavelength, respectively. Recordings of atmospheric pressure broadened lines over a 15 m open path of laboratory air are demonstrated, and show the potential of the new measurement scheme for multispecies detection. Especially interesting is the possibility to simultaneously probe mid-infrared-absorbing molecular species and near-infrared-absorbing molecules without strong mid-infrared absorption. A continuous tuning range in the mid-infrared of  $3.6\text{ cm}^{-1}$  is achieved by synchronously scanning the frequency of both near-infrared lasers. Isotopic species detection and pressure dependence studies of methane lineshapes were performed in an absorption cell. A typical indoor air methane background level of 3 ppm was reported, which as expected is higher than the typical outdoor level of 1.7 ppm. The signal-to-noise ratio in the recorded methane spectra indicates that sub-ppm detection of methane at atmospheric pressure is feasible over a measurement path of 10 meters and that practical multispecies detection can be performed over longer outdoor absorption paths.

### Acknowledgements

The absorption wavelength relations for multispecies monitoring were pointed out by Dr. V.S. Avetisov. This work was supported by the Swedish Research Council for Engineering Sciences (TFR) and the Knut and Alice Wallenberg Foundation.

### References

1. A.A. Kostrov, R.F. Curl, F.K. Tittel, G. Gmachl, F. Capasso, D.L. Sivco, J.N. Baillargeon, A.L. Hutchinson, A.Y. Cho: *Opt. Lett.* **24**, 1762 (1999)
2. S.W. Sharpe, J.F. Kelly, J.S. Hartman, C. Gmachl, F. Capasso, D.L. Sivco, J.N. Baillargeon, A. Y. Cho: *Opt. Lett.* **23**, 1396 (1998)
3. K. Namjou, S. Cai, E.A. Whittaker, J. Faist, C. Gmachl, F. Capasso, D.L. Sivco, A.Y. Cho: *Opt. Lett.* **23**, 219 (1998)
4. U. Simon, C.E. Miller, C.C. Bradley, R.G. Hulet, R.F. Curl, F.K. Tittel: *Opt. Lett.* **18**, 1062 (1993)
5. K.P. Petrov, L. Goldberg, W.K. Burns, R.F. Curl, F.K. Tittel: *Opt. Lett.* **21**, 86 (1996)
6. W. Schade, T. Blanke, U. Willer, C. Rempel: *Appl. Phys. B* **63**, 99 (1996)
7. B. Sumpf, T. Kelz, M. Nägele, and H.-D. Kronfeldt: *Appl. Phys. B* **64**, 521 (1997)
8. K.P. Petrov, S. Waltman, E.J. Dlugokencky, M. Arbore, M.M. Fejer, F.K. Tittel, L.W. Hollberg: *Appl. Phys. B* **64**, 567 (1997)
9. K.P. Petrov, R.F. Curl, F.K. Tittel: *Appl. Phys. B* **66**, 531 (1998)

10. D.G. Lancaster, D. Richter, R.F. Curl, F.K. Tittel: Appl. Phys. B **67** 339 (1998)
11. M. Seiter, D. Keller, M.W. Sigrist: Appl. Phys. B **67**, 351 (1998)
12. T. Kelz, A. Schumacher, M. Nägele, B. Sumpf, H.-D. Kronfeldt: J. Quant. Spectrosc. Radiat. Transfer **61**, 591 (1999)
13. D.G. Lancaster, D. Richter, R.F. Curl, F.K. Tittel, L. Goldberg, J. Koplow: Opt. Lett. **24**, 1744 (1999)
14. U. Westblom, M. Aldén: Appl. Opt. **28**, 2592 (1989)
15. U. Westblom, M. Aldén: Appl Spectr. **44**, 881 (1990)
16. D.S. Baer, R.K. Hanson, M.E. Newfield, N.K.J.M. Gopal: Opt. Lett. **19**, 1900 (1994)
17. M. Aldén, H. Edner, S. Svanberg: Appl. Phys. B **29**, 93 (1982)
18. B.J. Jefferies, R.A. Copeland, G.P. Smith, D.R. Crosley: *Twentyfirst International Symposium on Combustion* (The Combustion Institute, Pittsburg 1986) p.1709
19. T.-B. Chu and M. Broyer: J. Physique **46**, 523 (1985)
20. L.S. Rothman, C.P. Rinsland, A. Goldman, S.T. Massie, D.P. Edwards, J.-M. Flaud, A. Perrin, C. Camy-Peyret, V. Dana, J.-Y. Mandin, J. Schroeder, A. McCann, R.R. Gamache, R.B. Wattson, K. Yoshino, K.V. Chance, K.W. Jucks, L.R. Brown, V. Nemtchinov, P. Varanasi: J. Quant. Spectrosc. Radiat. Transfer **60**, 665-710 (1998).

V



ELSEVIER

1 September 1999

OPTICS  
COMMUNICATIONS

Optics Communications 168 (1999) 17–24

www.elsevier.com/locate/optcom

## Single aerosol particle sizing and identification using a coupled-cavity diode laser

Jonas Sandsten <sup>\*</sup>, Ulf Gustafsson, Gabriel Somesfalean

*Department of Physics, Lund Institute of Technology, P.O. Box 118, S-221 00 Lund, Sweden*

Received 17 July 1998; received in revised form 14 May 1999; accepted 20 June 1999

### Abstract

A new instrument for aerosol particle size determination and identification by shape is presented. The instrument is based on a diode laser in a coupled cavity. An extinction loss determines the size of a single aerosol particle entering the coupled-cavity diode laser, and a Fourier transformed diffraction image of near-forward scattered light is used for shape and orientation analysis. We describe a model of the coupled-cavity diode laser using light scattering based on Mie theory. This model relates the extinction loss directly to the cross-sectional area of the aerosol particle and shows good agreement with experimental results on aerosol particles and fibers. It is demonstrated that the changes in extinction loss are essentially independent of refractive index of the aerosol particles. The measurable size range of the aerosol particles is 4–170  $\mu\text{m}$  with an accuracy of  $\pm 0.5 \mu\text{m}$ . The lower limit of the range is set by the extinction loss  $S/N$  ratio, the upper limit is given by the laser beam cross-section, and the accuracy is imposed by the oscillations in the extinction efficiency factor. © 1999 Elsevier Science B.V. All rights reserved.

PACS: 07.60. – j; 42.55.Px; 42.25.Fx

Keywords: Coupled cavity; Diode laser; Diffraction; Light scattering; Aerosol particle

### 1. Introduction

Allergy and asthma are known to increase because of poor indoor air quality and high levels of particulate contaminants and pollen in the outdoor environment [1]. Rapid changes in production technology and the introduction of new materials lead to new potential risks. It is desirable to be able to monitor and identify aerosol particles, such as fungal spores, microorganisms and fibers of hazardous materials, in a timely manner.

The new instrument presented in this paper allows size determination and identification by shape of aerosol particles in situ, using a commercially available diode laser in a coupled-cavity configuration with weak feedback. Detection and sizing are done by an extinction loss signal depending on light scattered out of the coupled cavity, and identification is performed using a diffraction image of near-forward scattered light.

Another technique based only on extinction loss uses an intra-cavity He–Ne laser with high mirror reflectivities [2]. A quality of our coupled-cavity configuration is the weak reflectivity of the external mirror which makes it possible to transmit near-for-

<sup>\*</sup> Corresponding author. Tel.: +46-46-222-4805; fax: +46-46-222-4250; E-mail: jonas.sandsten@fysik.lth.se

ward scattered light and distinguish aerosol particles with different shapes giving rise to the same extinction loss. Other optical techniques for aerosol particle sensing have been explored using lasers, for example time-of-flight monitoring and light scattering [3,4]. The instrument presented here distinguishes itself from existing techniques by combining an extinction loss with a diffraction image from a single particle measurement.

## 2. Description of the instrument

Our instrumental set-up, shown in Fig. 1, uses a diode laser in a coupled-cavity configuration, a digitizing oscilloscope, an infrared-sensitive CCD camera, and a high-resolution spectrometer. The coupled-cavity configuration consists of a single-mode AlGaAs diode laser (Sony SLD114VS) lasing at 780 nm with a free-running threshold current of 19.4 mA, an aspheric lens (Geltech 350230-B, N.A. = 0.55) which collimates the laser light to an approximately Gaussian elliptical beam with the 'top hat' full widths  $0.38 \text{ mm} \times 0.16 \text{ mm}$ , a 10 cm long coupled cavity and an external planar mirror with a reflectivity  $R_{\text{ext}} = 4\%$ . A specially designed piezo-controlled mirror mount with high angular resolution ( $< 1 \text{ arc sec}$ ) is used to align the coupled cavity. We also employ active control of the mirror mount with an autoalignment system (Melles Griot NanoTrak), which simplifies the alignment procedure before measurements. The reduction of the threshold current

with the coupled cavity is 6%. Coupling efficiency is mainly governed by the external mirror alignment, the numerical aperture of the collimator and the astigmatism of the diode laser. The coupling efficiency and the beam dimensions were investigated and simulated during the design of the instrument with an optics design software and a beam intensity profiler [5,6].

The working point, specified by the injection current, the temperature of the diode laser and the coupled-cavity length, was chosen so that the single-mode frequency of the free-running diode laser coincides with the coupled-cavity single-mode frequency. The injection current was set to 18.9 mA, which is above the threshold current of the coupled-cavity diode laser at 18.2 mA, but below the onset of the coherence collapse region at 20 mA [7]. During the design phase we have characterized the mode structure and optimized for single-mode operation of the coupled cavity with a spectrometer.

The sensing volume is comprised of the central part of the laser beam inside the coupled cavity together with the depth of field of the Fourier lens ( $L_1$ ). Introduction of an aerosol particle into the sensing volume along the major axis of the beam is accomplished with a nozzle designed to position the aerosol particle in a laminar air flow passing through the center of the beam. In this way we assure the alignment of different aerosol particles due to their specific aerodynamic properties. A fiber will, for example, traverse the laser beam aligned parallel to the laminar air flow.

The extinction loss, which determines the size of the aerosol particles, is measured with the photodiode integrated in the diode-laser housing. With a level discriminator it is possible to set the instrument to sample aerosol particles of the same size distribution. One feature of the measurement scheme is that there is no need for an external photodiode, which, in combination with folded rays of the diffraction image, makes the instrument fairly compact ( $0.3 \times 0.3 \times 0.2 \text{ m}^3$ ).

In addition to measuring the extinction loss, near-forward scattered light at angles between  $2$  and  $10^\circ$  is collected and transformed with the Fourier lens ( $L_1$ ). The resulting diffraction pattern is imaged with the lenses ( $L_2$  and  $L_3$ ) onto the CCD. The capture of the diffraction image is triggered by the

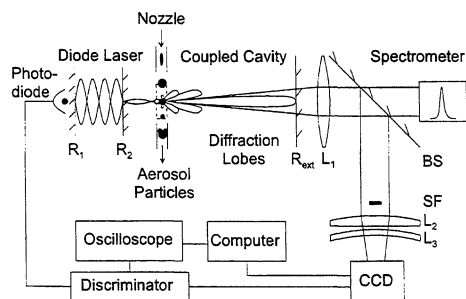


Fig. 1. Schematic of the instrumental set-up for aerosol particle measurements using extinction loss and near-forward scattered light. Laser diode facets,  $R_1$  and  $R_2$ ; planar external mirror,  $R_{\text{ext}}$ ; Fourier lens,  $L_1$ ; beamsplitter,  $BS$ ; spatial filter,  $SF$ ; Fourier-plane imaging lenses,  $L_2$  and  $L_3$ .

discriminator and a background image is subtracted from the image. The spatial frequencies in the diffraction image give information on the cross-section of the aerosol particles. The angular region is set by a spatial filter (SF) in the Fourier plane used for filtering out the direct light from the diode laser, and by the aperture of lens  $L_1$ .

### 3. Coupled-cavity model with Mie scattering

In the following we present a model describing the coupled-cavity diode laser using light scattering based on Mie theory for the detection and sizing of aerosol particles. The model characterizes the changes in the monitored output power as a function of the size of the particles by relating the extinction loss directly to the particle cross-sectional area. It is demonstrated that the changes in output power are essentially independent of refractive index of the aerosol particles.

Our model is an extension of the work presented in previous articles describing diode lasers subject to varying levels of external optical feedback [8–10]. The coupled cavity is considered equivalent to a solitary diode laser by replacing the inner facet reflectivity  $R_2$ , and the external plane mirror reflectivity  $R_3 = kR_{\text{ext}}$  ( $0 \leq k \leq 1$ ), with an effective reflectivity  $R_e$  (see Fig. 1). The coupling coefficient  $k$  accounts for optical losses in coupling the reflected light back into the diode laser. The single-reflection approximation is used due to weak feedback from the external plane mirror. This yields an effective reflectivity of the coupled facet with no particle perturbations

$$R_e = R_2 + (1 - R_2)^2 R_3. \quad (1)$$

Particles introduced in the radiation field inside the coupled cavity create losses due to scattering and absorption. The diffracted light becomes essentially divergent and is not coupled back into the diode cavity, while the central refracted light undergoes a phase shift and, being incoherently coupled, is also lost. Thus, the particle perturbation is completely described by light extinction in the direction of propagation. In Mie scattering theory, optical extinction is represented by the extinction cross-section  $C_{\text{ext}}$ , which is the product of the extinction efficiency

factor  $Q_{\text{ext}}$  and the aerosol particle cross-sectional area  $A_p$  [11]. The extinction efficiency factor is, especially for small particle sizes, an oscillating function of the ratio of particle radius to wavelength and of the index of refraction.  $Q_{\text{ext}}$  quickly converges to a value of 2 for particles larger than about  $4\lambda$ . In the presence of a particle inside the coupled cavity the effective reflectivity is

$$R_p = R_2 + (1 - R_2)^2 \left(1 - \frac{Q_{\text{ext}} A_p}{A_b}\right)^2 R_3, \quad (2)$$

where the additional factor  $(1 - Q_{\text{ext}} A_p / A_b)^2$  accounts for the particle-induced extinction loss, and  $A_b$  is the equivalent ‘top hat’ laser beam cross-sectional area inside the coupled cavity.

The output power of the equivalent solitary diode laser can be expressed as a linear function of the threshold current reduction  $I - I_{\text{th,e}}$  and of the total loss [12,13]. This relation is still valid for the perturbing particle case provided that the effective reflectivity,  $R_p$ , and the threshold current associated with the perturbation,  $I_{\text{th,p}}$ , replace  $R_e$  and  $I_{\text{th,e}}$  respectively. The output power emitted from the uncoupled facet of the laser is

$$P_p = \frac{\hbar \omega}{e} (I - I_{\text{th,p}}) \eta_i \frac{\ln(1/R_1)}{2\alpha_i L + \ln(1/R_1 R_p)}, \quad (3)$$

where  $\hbar$  is Planck’s constant,  $e$  is the electron charge,  $I$  is the operating current, and the cavity parameters are:  $\omega$  the radiation frequency of the diode,  $\eta_i$  the internal quantum efficiency to account for spontaneous emissions and leakage currents,  $\alpha_i$  the intrinsic loss per unit length due to material absorption and scattering inside the laser diode cavity, and  $L$  the diode cavity length.

We make a linear approximation for the threshold current change as a function of the variable effective reflectivity  $R_p$ ,

$$I - I_{\text{th,p}} = (I - I_{\text{th,e}}) \frac{R_p - R_2}{R_e - R_2}. \quad (4)$$

In the unperturbed case, i.e.  $R_p = R_e$ , it follows from this relation that  $I_{\text{th,p}} = I_{\text{th,e}}$ , while if the particle is totally obstructing the beam, i.e.  $R_p = R_2$ , the operating current equals the threshold current  $I = I_{\text{th,p}}$  and the system stops lasing.

The particle-induced extinction loss  $S$  is defined as the proportional reduction of the initial output

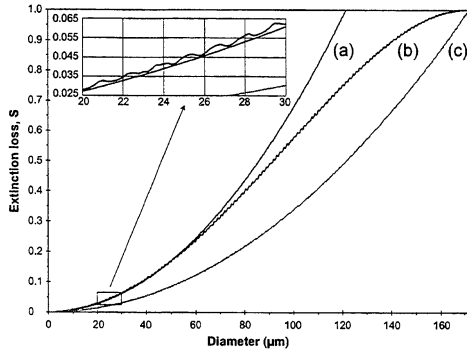


Fig. 2. The extinction loss vs. particle diameter. (a) Curve from the simple expression for the extinction loss (Eq. (6)). (b) Curve according to the complete coupled-cavity model (Eq. (5)). (c) Classical extinction curve. The insert is a magnification of the curves in the diameter range 20–30  $\mu\text{m}$ .

power  $P_e$ , according to  $S = (P_e - P_p)/P_e$ . Substituting Eq. (3) and Eq. (4) into this expression yields

$$S = 1 - \frac{P_p}{P_e} = 1 - \frac{(R_p - R_2) 2 \alpha_i L + \ln(1/R_1 R_e)}{(R_e - R_2) 2 \alpha_i L + \ln(1/R_1 R_p)}. \quad (5)$$

A plot of the extinction loss vs. particle diameter is shown in Fig. 2 (curve b) using the parameter values for the coupled cavity:  $R_1 = 0.32$ ,  $R_2 = 0.32$ ,  $R_3 = 0.04$ ,  $\alpha_i = 20 \text{ cm}^{-1}$ ,  $L = 300 \mu\text{m}$ ,  $A_b = 0.048 \text{ mm}^2$  and  $\lambda = 780 \text{ nm}$ .  $Q_{\text{ext}}$  is calculated according to the routine in Ref. [11] by simulation of the Mie scattering theory for a homogeneous sphere with refractive index  $n = 1.55$  and cross-sectional area  $A_p = \pi r^2$ . With these parameters the extinction loss reaches its maximum value for a particle diameter of about 170  $\mu\text{m}$ .

A simple expression for the extinction loss can be derived from a few assumptions as to the physical properties of the aerosol particles. We first make the assumption that the particle cross-sectional area is much smaller than that of the beam,  $A_p \ll A_b$ . We then set the lower limit for particle size to  $4\lambda$ , so that  $Q_{\text{ext}} \approx 2$ . The result is that

$$S \approx 2 \frac{Q_{\text{ext}} A_p}{A_b} \approx 4 \frac{A_p}{A_b}, \quad (6)$$

which is also plotted in Fig. 2 (curve a) using the same parameter values as above. This simple expression for the extinction loss agrees well with the actual extinction loss for particle diameters up to about 70  $\mu\text{m}$ , where the assumption  $A_p \ll A_b$  is valid. In classical extinction, i.e. illuminating the particles outside a laser cavity, the extinction loss can be expressed as  $S = Q_{\text{ext}} A_p/A_b \approx 2 A_p/A_b$ , see Fig. 2 (curve c). That is, comparing with Eq. (6), the coupled-cavity extinction loss is twice as large as in classical extinction for aerosol particles up to 70  $\mu\text{m}$ . For larger particles the coupled-cavity extinction loss approaches the classical extinction loss. When  $2 A_p = A_b$ , i.e. for a particle having a diameter of 170  $\mu\text{m}$ , the classical and the coupled-cavity extinction loss have the same value.

The insert in Fig. 2 emphasizes that the oscillatory behavior of the extinction efficiency factor is reflected in the extinction loss variation. Calculations of the extinction efficiency factor with different refractive indices (ranging from 1.3 to 3.0) indicates that this oscillation sets the accuracy of the size measurements to  $\pm 0.5 \mu\text{m}$ . Thus, the extinction process is essentially independent of refractive index and implies that correct size measurements can be performed on particles with unknown or varying refractive indices.

#### 4. Experiments on aerosol particles

The instrument was used to measure individual nonabsorbing silica gel particles with irregular shapes and varying sizes, ranging from 15–40  $\mu\text{m}$  (Merck Silica Gel 60, refractive index  $n = 1.55$ ). The particle concentration was diluted in purified air, and the particles were aligned in a laminar airflow and passed through the sensing volume individually. The oscilloscope traces for particle sizes from 14–34  $\mu\text{m}$ , triggered in real time, are shown together in Fig. 3 to demonstrate the effect of particle size on extinction losses. For validation, 14 diffraction images were used to estimate the size of the individual particles, and the results are plotted in Fig. 4 together with the theoretical curves given by Eq. (5) and Eq. (6). The error bars were defined as twice the standard deviation in the extinction loss. The deviations from the theoretical curves are explained by uncer-

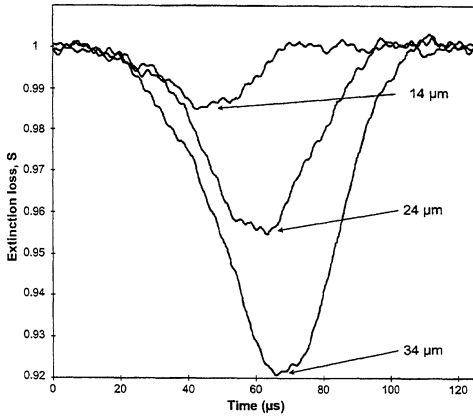


Fig. 3. Extinction losses from silica gel aerosol particles passing the sensing volume. The particle sizes are 14, 24 and 34  $\mu\text{m}$ .

tainties of the size determination using the diffraction images. We use the measured extinction loss to calculate the distribution of 100 silica gel particles applying Eq. (5) of the coupled-cavity model, see Fig. 5. This is feasible when the particles are approximated as being spherical. According to the specifications, 90% of the particle sizes should be between 15–40  $\mu\text{m}$ , which is in good agreement with our results. The current signal-to-noise ratio implies that the smallest detectable size is 4  $\mu\text{m}$ . The size sensi-

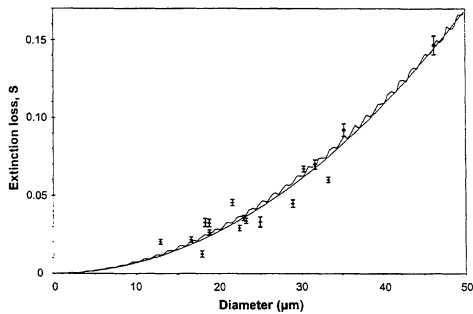


Fig. 4. Extinction loss from silica gel particles (—) and fibers ( $\blacklozenge$ ) together with theoretical curves (Eq. (5) and (6)). The error bars of the silica gel particles are set by the noise in the measured extinction loss, while the error bars for the fibers are equal to one standard deviation of five measurements.

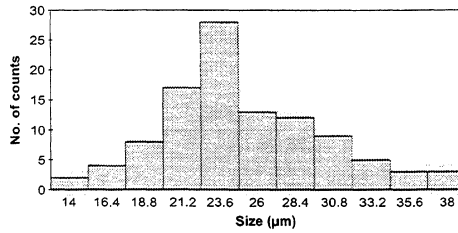


Fig. 5. Aerosol particle distribution obtained using the coupled-cavity model (Eq. (5)).

tivity of the instrument can be improved by reducing the laser beam diameter.

### 5. Experiments on fibers

We have also performed measurements on fibers with varying refractive indices, and evaluated the results with the model developed. Mie theory simulations applied on infinite cylindrical objects show that the cross-section of the fiber is governing the extinction loss. The fiber materials used were glass, carbon and kevlar<sup>®</sup>; the glass fibers were made by stretching melted sodium glass, while the kevlar and carbon fibers come from reinforcement materials used in surgery. The diameter of the fibers were measured with a calibrated microscope and detailed experiments were performed on three selected samples; a

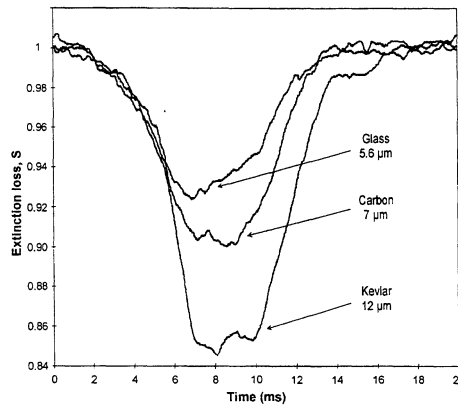


Fig. 6. Extinction loss measured for glass, carbon and kevlar fibers.

Table 1  
Experimental and calculated data for the fiber measurements

Material	Microscope measured diameter ( $\mu\text{m}$ )	Optical equivalent diameter ( $\mu\text{m}$ )	Measured extinction loss, $S$	Calculated diameter ( $\mu\text{m}$ )
Glass	$5.6 \pm 0.1$	$31.6 \pm 0.3$	$0.070 \pm 0.003$	$5.5 \pm 0.3$
Carbon	$7.0 \pm 0.1$	$35.3 \pm 0.3$	$0.092 \pm 0.004$	$7.4 \pm 0.4$
Kevlar	$12 \pm 0.1$	$46.2 \pm 0.2$	$0.147 \pm 0.006$	$12.1 \pm 0.5$

Fiber measurements.

glass fiber with a diameter of  $5.6 \mu\text{m}$ ; a carbon fiber with a diameter of  $7 \mu\text{m}$  and a kevlar fiber with a diameter of  $12 \mu\text{m}$ . The experiments were performed by manually translating the fibers, which were  $10 \text{ mm}$  long and mounted in holders, through the sensing volume of the coupled cavity.

In Fig. 6 we present the single recordings of the time-resolved extinction losses from the three fibers. Scaling is needed in order to compare the resulting extinction losses with those obtained from spherical particles passing through the Gaussian beam. The diameter and length of the fiber are consequently

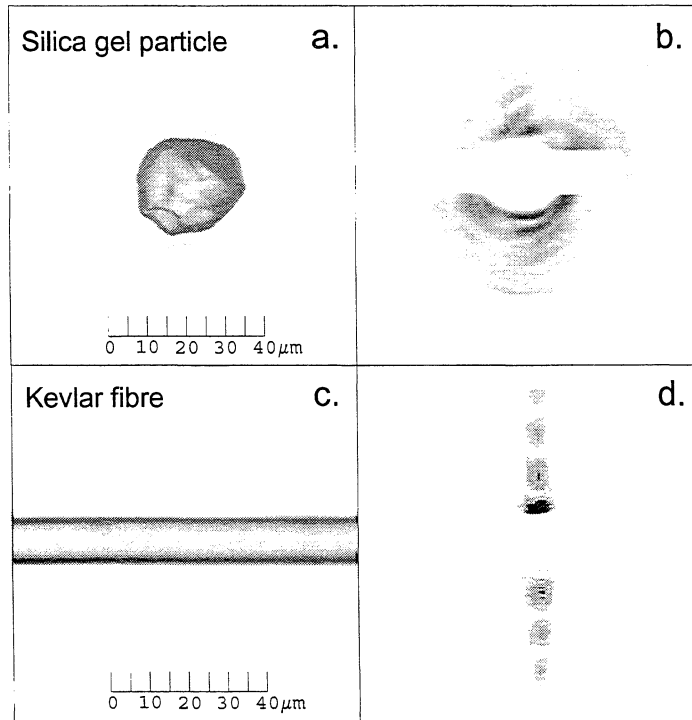


Fig. 7. (a) Microscope image of a silica gel particle with a diameter of  $25 \mu\text{m}$ , and (b) corresponding experimental diffraction image of near-forward scattered light. (c) Microscope image of a kevlar fiber with a diameter of  $12 \mu\text{m}$ , and (d) corresponding experimental diffraction image.

used to derive the diameter of an equivalent spherical particle which induces the same optical power extinction. Given an undisturbed optical power  $P_1 = I_0 A_b$  and an integrated power extinction  $P_s$  caused by a fiber, then an optical equivalent radius can be defined and calculated from the relation  $P_s = I_0 \pi r^2$ . The fiber extinction losses vs. the optical equivalent diameter are plotted together with the silica gel particles in Fig. 4. Experimental and calculated data from all the fiber measurements are summarized in Table 1. The optical equivalent diameter was calculated by scaling the microscope measured diameter, and the measured extinction loss was used to derive the calculated diameter.

The results show good agreement with this extension of the model to non-spherical particles. It is also verified that the extinction process is essentially independent of refractive index of the fiber material. Thus, correct size measurements can be performed on aerosol particles with unknown or varying refractive indices.

## 6. Identifying aerosol particles and fibers

Information on shape and orientation of the aerosol particle is obtained from the captured Fourier transformed diffraction image of near-forward scattered light. An aerosol particle inside the sensing volume forms a two-dimensional diffraction image determined by its shape. Irregularly shaped aerosol particles produce a more complex but specific image. These diffraction images can be used to identify the aerosol particle. Fig. 7 shows microscope images and corresponding Fourier transformed diffraction images of near-forward scattered light from a silica gel particle and a kevlar fiber inside the sensing volume. Image processing was done on the diffraction images to reduce the noise and enhance the contrast in the images. The central part of the diffraction images is obscured by the spatial filter (SF). The diffraction pattern of the silica gel particle has a concentric appearance thus indicating a spherical object. The kevlar fiber, which extends outside the sensing volume, produce mainly a one-dimensional diffraction image consisting of a series of light spots perpendicular to the fiber direction. Quantitative information about the relative proportions in the shape of a

particle can be inferred by analyzing the position of diffraction light intensity minima.

## 7. Conclusions

We have presented an instrument based on a commercially available diode laser in a coupled-cavity configuration, that utilizes extinction loss and near-forward scattered light to detect and identify aerosol particles. The compact instrument combines single-particle sizing with shape analysis of the aerosol particles. The experimental results clearly show that aerosol particles and fibers induce extinction losses that increase with increasing diameter, in good agreement with the developed coupled-cavity model. It is demonstrated that the extinction loss is essentially independent of refractive index. Information on shape and orientation of the aerosol particle is obtained from the diffraction image of near-forward scattered light. The measurable size range of the aerosol particles is 4–170  $\mu\text{m}$  with an accuracy of  $\pm 0.5 \mu\text{m}$ .

An optical trap [14] could be used for detailed investigation of the shape of a single aerosol particle by analyzing the diffraction images for different alignments in the sensing volume. The information obtained from these measurements can be used to compose a database of diffraction images for pattern recognition and automatic identification of various aerosol particles.

## Acknowledgements

We wish to thank S. Svanberg, M. Bohgard, E. Swietlicki, J. Smith and H. Edner for support and many helpful discussions. This research was financed by the Swedish Research Council for Engineering Sciences (TFR), the Environmental Fund of the Swedish Association of Graduate Engineers (CF) and the Knut and Alice Wallenberg Foundation.

## References

- [1] L. Morawska, N.D. Bofinger, M. Maroni (Eds.), *Indoor Air*, Elsevier Science, Oxford, 1995.
- [2] B.G. Schuster, R. Knollenberg, *Appl. Opt.* 11 (1972) 1515.

- [3] J. Gebhart, D.J. Rader, T.J. O'Hern, P.A. Baron, M.K. Mazumder, Y.S. Cheng, in: K. Willeke, P.A. Baron (Eds.), *Aerosol Measurement, Chapters 15–17*, Van Nostrand Reinhold, New York, 1993.
- [4] A. Macke, M.I. Mishchenko, K. Muinonen, B.E. Carlson, *Opt. Lett.* 20 (1995) 1934.
- [5] OSLO, *Optics Software for Layout and Optimization, Ver. 5.1*, Sinclair Optics, 1996.
- [6] M. Bottlinger, H. Umhauer, *Appl. Opt.* 30 (1991) 4732.
- [7] J. Kitching, R. Boyd, A. Yariv, *Opt. Lett.* 19 (1994) 1331.
- [8] R.P. Salathé, *Appl. Phys.* 20 (1979) 1.
- [9] R. Lang, K. Kobayashi, *IEEE J. Quantum Electron.* QE-16 (1980) 347.
- [10] J. Sigg, *IEEE J. Quantum Electron.* 29 (1993) 1262.
- [11] C.F. Bohren, D.R. Huffman, *Absorption and Scattering of Light by Small Particles*, John Wiley and Sons, New York, 1983.
- [12] K.J. Ebeling, *Integrated Optoelectronics: Waveguide Optics*, Springer-Verlag, 1993.
- [13] D.M. Kane, A.P. Willis, *Appl. Opt.* 34 (1995) 4316–4325.
- [14] A. Ashkin, J.M. Dziedzic, J.E. Bjorkholm, S. Chu, *Opt. Lett.* 11 (1986) 288.